Preclinical Evaluation of Glioma and Neuroblastoma Cells in the Chick Embryo Model

Inaugural-Dissertation

zur Erlangung des Doktorgrades
der Mathematisch-Naturwissenschaftlichen Fakultät

der Heinrich-Heine-Universität Düsseldorf

vorgelegt von

Sandra Krause

aus Aachen

Düsseldorf, Januar 2026

Gedruckt mit der Genehmigung der
Mathematisch-Naturwissenschaftlichen Fakultät der
Heinrich-Heine-Universität Düsseldorf

Berichterstatter:

1. PD Dr. Antje Willuweit

2. Prof. Dr. Dieter Willbold

Tag der mündlichen Prüfung: 09.04.2026

I Declaration

I declare under oath that I have produced my thesis independently and without any undue assistance by third parties under consideration of the ‘Principles for the Safeguarding of Good Scientific Practice at Heinrich Heine University Düsseldorf'.

Jülich, 08.01.2026

II Publications

Choi, C. H., Bruch, M., Hong, S. M., **Krause, S.**, Stegmayr, C., Schwan, S., Worthoff, W. A., Felder, J., & Shah, N. J. (2024). A Modified Quadrature Birdcage Coil Incorporated With a Curved Feature for In Ovo MR Imaging. IEEE open journal of engineering in medicine and biology, 5, 534–541. https://doi.org/10.1109/OJEMB.2024.3420231

Choi, C. H., Hong, S. M., Felder, J., Bruch, M., Worthoff, W. A., **Krause, S.**, & Shah, N. J. (2024). Design, construction, and use of a tapered-spiral, quadrature 1H/23Na double-tuned coil for in ovo MRI at 7 T. Medical physics, 51(12), 8761–8767. https://doi.org/10.1002/mp.17448

Galldiks, N., Lohmann, P., Friedrich, M., Werner, J. M., Stetter, I., Wollring, M. M., Ceccon, G., Stegmayr, C., **Krause, S.**, Fink, G. R., Law, I., Langen, K. J., & Tonn, J. C. (2024). PET imaging of gliomas: Status quo and quo vadis?. Neuro-oncology, 26, S185–S198. https://doi.org/10.1093/neuonc/noae078

Krause, S., Florea, A., Choi, C. H., Worthoff, W. A., Heinzel, A., Fischer, S., Burda, N., Neumaier, B., Shah, N. J., Lohmann, P., Mottaghy, F. M., Langen, K. J., & Stegmayr, C. (2025). Autoradiography of Intracerebral Tumours in the Chick Embryo Model: A Feasibility Study Using Different PET Tracers. Molecular imaging and biology, 27(2), 151–162. https://doi.org/10.1007/s11307-025-01983-9

Lohmann, P., Schäfer, L., **Krause, S.**, Altunay, B., Willuweit, A., Werner, J. M., Galldiks, N., Langen, K. J., Mottaghy, F. M., & Lütje, S. (2025). Advancements in noninvasive visualization of the immune environment in glioblastoma: A systematic review. Neuro-oncology advances, 7(1), vdaf176. https://doi.org/10.1093/noajnl/vdaf176

III Acknowledgements - Danksagung

Diese Dissertation wäre ohne die fachliche und persönliche Unterstützung vieler Menschen nicht denkbar gewesen. Ihnen allen gilt an dieser Stelle mein aufrichtiger Dank.

Zunächst möchte ich meiner Doktormutter PD Dr. Antje Willuweit für ihre Unterstützung danken. Sie hat mir die notwendigen Freiräume, Ressourcen und Rückendeckung gegeben, die diese Arbeit möglich gemacht haben.

Einen besonderen Dank gilt außerdem meinem Arbeitsgruppenleiter PD Dr. Philipp Lohmann durch seine Bereitschaft, trotz seiner zahlreichen Verpflichtungen meine Betreuung zu übernehmen. Seine offene Tür, seine kontinuierliche Unterstützung, seine Ideen und seine verlässliche Beratung haben mir in entscheidenden Phasen Orientierung und Sicherheit gegeben. Sein Engagement, auch inmitten eines vollen Terminkalenders immer Zeit für meine Fragen und Anliegen zu finden, hat diese Dissertation wesentlich geprägt und ermöglicht.

Auch möchte ich mich herzlichst bei Prof. Dr. Karl-Josef Langen bedanken, der mir in entscheidenden Momenten den Weg gewiesen hat, und bei Prof Dr. Dieter Willbold für seine Unterstützung im Rahmen der Co-Betreuung dieser Arbeit. Außerdem gilt mein Dank Prof. Dr. N. Jon Shah für die Bereitstellung der Rahmenbedingungen und für die Möglichkeit der Promotion in seinem Institut. Zudem möchte ich mich bei Prof. Dr. Dr. Susanne Lütje und dem Team der Nuklearmedizin der Uniklinik Aachen für die reibungslose wissenschaftliche Kooperation bedanken. Meiner ehemaligen Betreuerin Dr. Carina Stegmayr danke ich für ihre Vorarbeit, Einarbeitung und Unterstützung in der Durchführung von Hühnerembryo-Experimenten. Dem Graduiertenkolleg RTG 2610 InnoRetVision danke ich für die interdisziplinären Impulse und die Möglichkeit, über den eigenen fachlichen Tellerrand hinauszublicken.

Meinen Kolleginnen und Kollegen danke ich für ihre unverzichtbare Unterstützung im Alltag dieser Dissertation. Danke an Lara Kliebe, Nicole Burda, Mari Bonse und Michael Schöneck für eure Bereitschaft, mich im Labor und in schwierigen Situationen zu unterstützen. Ohne euch wäre dieser Weg deutlich steiniger gewesen.

Meiner Familie danke ich von Herzen für die bedingungslose Unterstützung und das Vertrauen während des Studiums und der Promotionszeit. Ihr Rückhalt hat mir in allen Phasen dieser Arbeit Sicherheit und Motivation gegeben. Ein besonderer Dank gilt meinem Partner Pieter für seine Geduld, stetige Ermutigung, ständiges Interesse und Unterstützung in allen Lebenslagen.

IV Abbreviations

AC	activity concentration
ALK	anaplastic lymphoma kinase
BBB	blood-brain barrier
CAM	chorioallantoic membrane
CE	contrast enhancement
CNS	central nervous system
DAPI	4’,6-Diamidin-2-phenylindol
DMSO	dimethyl sulfoxide
DOTA	(1,4,7,10-tetraazacyclododecane-1,4,7,10-tetrayl)tetraacetic acid
DPBS	Dulbecco’s phosphate buffered saline
EDD	embryonic development day
EDTA	ethylenediaminetetraacetic acid
FAPI	[^{68}Ga] small molecule fibroblast activation protein inhibitor
FDG	[^{18}F]fluorodesoxyglucose
FDOPA	3,4-dihydroxy-6-[^{18}F]-fluoro-L-phenylalanine
FET	O-(2-[^{18}F]-fluoroethyl)-L-tyrosine
FID	Fraction of injected dose
FLAIR	fluid-attenuated inversion recovery
GFAP	glial fibrillary acidic protein
GLUT1	glucose transporter 1
HH	Hamburger-Hamilton
HKII	hexokinase II
IDH	isocitrate dehydrogenase
INRG	international neuroblastoma risk group
LAT	large neutral amino acid transporter
MIBG	[^{123}I]metaiodobenzylguanidine
MR	magnetic resonance
MRI	magnetic resonance imaging

PBS	phosphate-buffered saline
PET	positron emission tomography
rH	relative humidity
ROI	region of interest
RPMI	Roswell park memorial institute
SNR	signal-to-noise ratio
SOX2	sex determining region Y box 2
SPECT	single photon emission computed tomography
SUV	standardised uptake value
TAC	time-activity-curves
TBR	tumour-to-background ratio
TBS	tris-buffered saline
TE	echo time
TR	repetition time
VOI	volume of interest
WHO	World Health Organisation

V List of figures

VI List of tables

VII Deutsche Zusammenfassung

Bis heute haben sich Tierversuche für aussagekräftige *in vivo* Forschung in verschiedenen präklinischen Bewertungen neuroonkologischer Erkrankungen als unverzichtbar erwiesen. Angesichts zunehmender ethischer Bedenken hinsichtlich der Verwendung von Tieren in der experimentellen Forschung müssen geeignete Alternativen gefunden werden. In den vergangenen Jahren hat das Hühnerembryo-Modell für diesen Zweck Aufmerksamkeit erlangt. In einigen Studien wurde mit der Verwendung des Xenotransplantat-Chorioallantoismembran (CAM) Modells sowie orthotopischer Hirntumormodelle in Hühnerembryonen begonnen. Allerdings müssen einige Herausforderungen, wie technisch anspruchsvolle Injektionsverfahren und Schwierigkeiten bei der Reproduzierbarkeit, zur Etablierung evaluiert werden.
In dieser Arbeit wurde das Hühnerembryo-Modell auf Grundlage eines intrazerebralen Gliom-Modells sowie eines Neuroblastom-CAM-Modells zur Etablierung von Alternativen im Bereich der medizinischen Bildgebung und zur Prüfung der translationalen Validität von Radiotracern eingesetzt.

Zwecks Analyse des intrazerebralen Gliom-Modells wurden zwei Gliomzelllinien in das Mesencephalon der Hühnerembryonen implantiert. Anschließend wurde die Blut-Hirnschrankenintegrität und Traceraufnahmen des tumortragenden Gehirns bewertet und mit berichteten Werten anderer Spezies verglichen. Die Tumorinokulationstechnik führte zu reproduzierbaren Hirntumoren innerhalb der Ventrikel des optischen Tectum. Die Analyse der Blut-Hirnschrankenintegrität an Tumorpositionen zeigte eine hohe Heterogenität. Die Radiotracer-Bildgebung war in den betrachteten Bildgebungsaspekten vergleichbar zum Nagetier Gliom-Modell und zu Hirntumorpatienten.

Das Hühnerembryo-CAM-Modell wurde mithilfe etablierter Radiotracer mit zwei Neuroblastomzelllinien evaluiert. Dafür wurden die Zelllinien auf die CAM implantiert und nach Tumorwachstum die Radiotraceraufnahme evaluiert. Es wurden keine signifikanten Unterschiede in der Tumortraceraufnahme festgestellt, wodurch eine hohe Übereinstimmung zweier klinisch etablierter Tracer mit dem neu getesteten O-(2-[^{18}F]-fluoroethyl)-L-tyrosine (FET) erkennbar wurde. Außerdem zeigte der Vergleich zu Patienten eine hohe Übereinstimmung. Allerdings müssen einige methodische Aspekte berücksichtigt werden, um die Reproduzierbarkeit und Validität der erzielten Ergebnisse in CAM-Radiotracer-Experimenten sicherzustellen.

Insgesamt bietet das Hühnerembryo-Modell eine hohe Vielseitigkeit und ein ethisch vertretbareres Modell als das Nagetiermodell für die präklinische neuroonkologische Forschung. Jedoch sind einige Einschränkungen zu berücksichtigen, die von hohen Ausfallraten im intrazerebralen Hühnerembryo-Gliom-Modell bis zu einem höheren methodischen Aufwand für reproduzierbare Forschung in Radiotracer-Experimenten reichen. Außerdem können inhärente Unterschiede in der Biologie von Vögeln und Säugetieren, sowie Unterschiede zwischen embryonalen und adulten präklinischen Modellen die Übertragung der Ergebnisse auf potenzielle Anwendungen in Säugetieren einschränken. Daher muss die translationale Relevanz der aus Hühnerembryonen gewonnenen Erkenntnisse für Forschungsfragen sorgfältig betrachtet und interpretiert werden.

VIII English Summary

To date, animal experiments have proven to be indispensable for meaningful *in vivo* research in various preclinical evaluations of neuro-oncological diseases. With raising ethical concern of animal use in experimental research, suitable alternatives have to be found. In recent years, the chick embryo model has gained attention for this purpose. Several studies have initiated the employment of the chick embryo xenograft chorioallantoic membrane (CAM) model as well as chick embryo orthotopic xenograft models for brain tumours. However, some challenges, as technically demanding injection procedures or difficulties with reproducibility, need to be evaluated for further validation of tumour models in the chick embryo.

Thus, in this thesis, the chick embryo model was evaluated based on an intracerebral glioma model as well as a neuroblastoma CAM model for the establishment of alternatives in the field of medical imaging and evaluation of radiotracers in respect to their translational validity.

For the analysis of intracerebral glioma, two glioma cell lines were implanted into the mesencephalon of chick embryos. Subsequently, the blood-brain-barrier integrity of the tumour-bearing brain and tracer uptakes were evaluated and compared to reported values from rodents and patients. The tumour inoculation technique yielded reproducible brain tumours inside the ventricles of the chick tectum. The analysis of blood-brain barrier integrity in tumour region revealed high variability. Radiotracer imaging indicated high comparability to xenograft rodent glioma models or brain tumour patients in the regarded imaging aspects.

The chick embryo CAM model was evaluated in two neuroblastoma cell lines using established radiotracers. For this purpose, the cell lines were implanted onto the CAM and radiotracer uptake was evaluated after tumour growth. No significant differences in tumour tracer uptake were observed, arguing for high congruency of the two clinically established radiotracers to the newly tested FET. Besides, the comparison of tracer uptakes to neuroblastoma patients revealed high agreement. However, some methodological assessments have to be carefully considered to ensure reproducibility and validity of achieved results in CAM radiotracer experiments.

All in all, the chick embryo model offers high versatility and a more ethical model for preclinical neuro-oncological research. However, several limitations have to be considered, from high dropout rates in the intracerebral chick embryo model to higher methodological burden for reproducible research in radiotracer experiments. Also, inherent differences between avian and mammalian biology, as well as differences between embryonic and adult preclinical models, may limit the extrapolation of findings to potential applications in mammalian systems. Thus, the translational value and relevance of chick embryo derived results on research questions have to be carefully considered and interpreted.

Table of Contents

1 Introduction

1.1 Tumours of the Nervous System

1.1.1 Cancer of the Central Nervous System: Glioma

Tumours of the central nervous system (CNS) compromise a heterogeneous group of neoplasms that have a wide variation in histopathological features, molecular profile, and prognosis. Among these, gliomas represent the most common malignant primary brain tumour in adults, with an annual incidence of approximately 6 cases per 100,000 individuals worldwide [1]. Gliomas arise from glial or glial precursor cells, including oligodendrocytes and astrocytes, and show a wide histopathological and molecular diversity. Historically, gliomas were classified based on histologic features [2] which failed to capture the biological heterogeneity of gliomas. In 2021, the World Health Organisation (WHO) established the fifth edition of the WHO classification of tumours of the CNS, in which the significance of molecular markers for classification, alongside the histopathological assessment, increased substantially [3]. With this, adult-type diffuse gliomas are divided into three molecular entities, as visualised in Figure 1. Key determinant includes the mutation status of the enzyme isocitrate dehydrogenase (IDH), for the distinction of IDH wild-type glioblastoma and other rare IDH wild-type tumour types, as diffuse hemispheric or diffuse midline glioma, from IDH mutant astrocytoma and oligodendroglioma [1]. In IDH-mutant gliomas, a heterogeneous missense mutation at codon R132 in IDH1 is by far the most common, accounting for approximately 70-90% of all IDH1/2 mutations [4, 5].

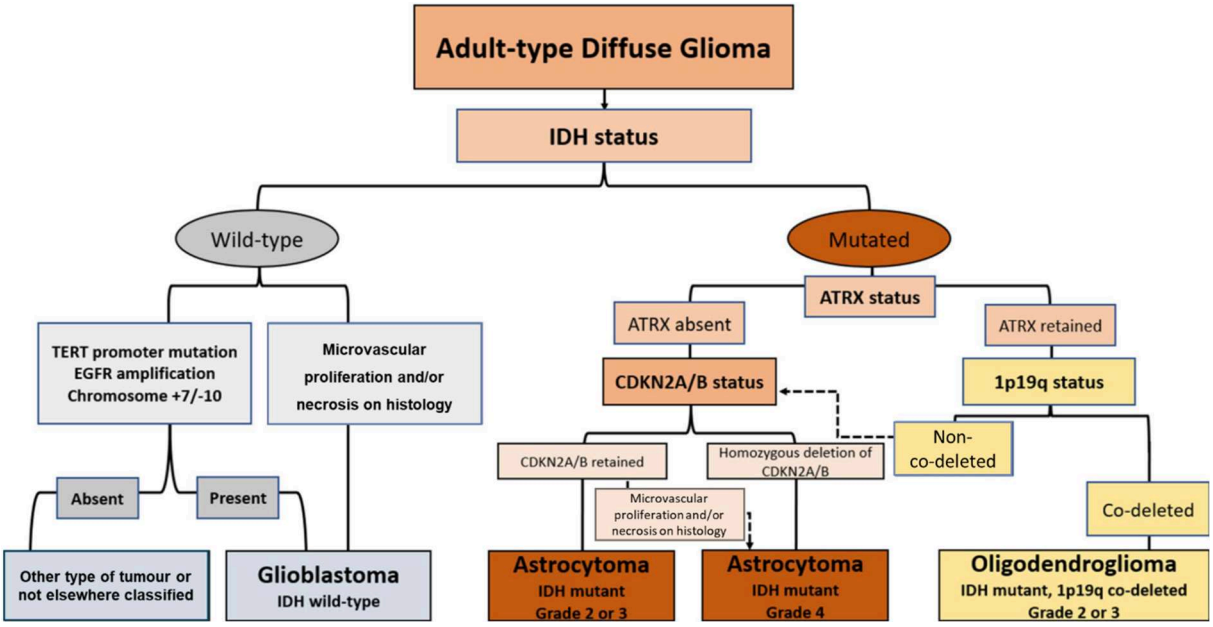

Figure 1: Schematic overview of the 2021 WHO classification of adult-type diffuse glioma (adapted from Nasany and La Fuente [6]). Abbreviations: IDH: Isocitrate Dehydrogenase; TERT: Telomerase Reverse Transcriptase; EGFR: Epidermal Growth Factor Receptor; ATRX: Alpha-Thalassemia/Mental Retardation Syndrome X; CDKN2A/B: Cyclin-Dependent Kinase Inhibitor 2A/B; 1p19q: Chromosome 1p and 19q.

Despite advances in molecular understanding and aggressive multimodal treatment strategies, including maximal safe surgical resection, radio- and chemotherapy, glioma remain largely incurable [1]. Particularly glioblastoma, with a 5-year overall relative survival of only 6.8% [7], continue to pose a major therapeutic challenge. Current research efforts focus on unravelling the molecular mechanisms driving therapy resistance, as its immunosuppressive microenvironment hindering immunotherapy efficacy [8], and offering insights into the tumour biology with the goal of developing more effective, targeted, and personalised treatment approaches [9].

One major hurdle for the treatment of all brain tumours is the blood-brain barrier (BBB) [10]: a complex and dynamic structure formed primarily by brain endothelial cells, supported by pericytes and astrocytic end-feet with tight junctions and molecular pumps that is selectively permeable, regulating the exchange of substances between the bloodstream and neural tissue while maintaining cerebral homeostasis and protecting the brain from toxins and pathogens [11, 12]. Various CNS pathologies show heterogeneous BBB dysfunction, including Alzheimer's disease, epilepsy, but also various tumours [13]. In context of glioma, BBB integrity is heterogenous: usually, BBB is intact in CNS WHO grade 2 gliomas, but disrupted in WHO grades 3 and 4 gliomas [14]. This heterogeneity significantly influences both medical imaging characteristics and treatment efficacy [15]. While conventional magnetic resonance imaging (MRI) has excellent soft tissue contrast with a high spatial resolution, contrast enhancement is achieved with gadolinium-based agents that accumulate in regions where the BBB is disrupted, leading to increased signal intensity on T1-weighted images. This enhancement thus only reflects BBB disruption and is non-specific for tumour tissue. Thus, it especially fails to delineate non-enhancing, IDH mutant gliomas with lower WHO grades reliably [16]. One main imaging modality offering insights into glioma metabolism and biology as well as treatment responses is positron emission tomography (PET), with utilisation of BBB-independent amino acid PET tracers that have gained interest since their first description in 1983 [17]. With today's advancements in clinical and technical PET guidelines for gliomas, integrations of artificial intelligence and radiomics, next-generation PET scanners, and the development of new and specialised PET tracers, PET imaging in gliomas has evolved considerably [18]. Taken together, the combination of structural MRI and PET remains of considerable diagnostic value in patients with brain tumours.

1.1.1.1 Modelling Glioma: Cell lines U-87 MG and U-87 IDH1^{R132H}

For the experimental modelling of glioma in human xenograft preclinical studies, established and widely characterised cell lines offer a practical platform. The cell line U-87 MG (HTB-14^{TM}, ATCC®) was generated from a malignant glioma of a male patient of unknown origin and age, likely with a glioblastoma, over 50 years ago [19]. Decoded in over 1,700 studies [20, 21], the cell line exhibits glioblastoma hallmarks as, for example, the molecular IDH wild-type marker or the ability to rapidly form tumours in xenograft models [22, 23]. Although the cell line differs from the original patient tumour [20], it still provides a well-described, established and practical platform for preclinical use.

The modelling of IDH mutated molecular subtypes of gliomas proves to be more challenging, as glioma cells with IDH1 mutation currently cannot be stably propagated *in vitro* [24, 25]. Thus, variants of various glioblastoma cell lines, as U-87 MG, have been engineered to carry an IDH mutation. A notable example is the IDH1 mutant cell line U-87 IDH1^{R132H} (HTB-14IG^{TM}, ATCC ®), which was derived from the parental U-87 MG cell line by introducing a c.395G>A (IDH1R132H) knock-in mutation using CRISPR/Cas9 gene editing. This specific mutation is most common in gliomas with IDH mutation [26, 5, 4]. While the introduction of IDH mutations into U-87 MG provides a controlled framework for studying the impact of IDH1 mutation in an otherwise stable genetic background, the metabolite profile which is still that of a glioblastoma with other unknown but inherited mutations [27, 28] has to be carefully considered.

1.1.2 Cancer of the Sympathetic Nervous System: Neuroblastoma

Neuroblastoma is the most common extracranial paediatric solid tumour, accounting for about 7% of all paediatric neoplasms [29] and is mainly observed in small children [30]. Primary neuroblastomas originate from primitive neural crest cells, that normally give rise to adrenal medulla or anywhere along the sympathetic nervous system chain [31, 32]. Neuroblastomas encompass a broad spectrum of biological and clinical characteristics, reflecting their striking heterogeneity [32], ranging from spontaneous regressing tumours [33] to highly aggressive metastatic diseases [31, 34]. To address this complexity and enable consistent global comparison of patient outcomes, the International Neuroblastoma Risk Group (INRG) provided the INRG Staging System as well as the INRG Risk Classification for a standardized and transparent framework for diagnosis, staging, and risk stratification, including age, histologic category, grade of differentiation, metastatic stage, and genomic features [35, 36]. The INRG stages are divided into the subgroups L1, L2, M, and MS. In short, localised tumours confined in one body compartment without image-defined risk factors are included in L1, whereas L2 are locoregional tumours without image-defined risk factors. In INRG stage M, distant metastatic diseases except for stage MS are grouped, whereas MS are metastatic diseases confined to liver, bone marrow and/or skin in children younger than 18 months [36]. A simplified version of the INRG consensus schema for the pre-treatment classification is shown in Table 1. However, this system has not yet been adopted by all cooperative groups [37].

Genomic factors that predict the outcome of neuroblastoma have been identified, starting with MYCN, an oncogene on chromosome 2 that is biologically involved in various processes as migration, metastasis, proliferation, pluripotency, cell survival, apoptosis, self-renewal, angiogenesis, differentiation, and immune surveillance [38, 37]. MYCN amplification, defined as more than 10 copies per diploid genome, has been correlated with higher stage tumours [39] and shorter progression free survival [40]. Other relevant genomic mutations that occur in a subset of neuroblastomas and represent the most common genetic alterations of this tumour type, are activating mutations or amplifications of the anaplastic lymphoma kinase (ALK) gene [38].

Table 1: Simplified schematic overview of the INRG consensus pretreatment classification. Table created based on Cohn et al. [36].

INRG Stage	Age (months)	Histologic Category	MYCN	Pretreatment Risk Group
L1/L2		ganglioneuroma maturing; ganglioneuroblastoma intermixed		very low
L1		any, except from ganglioneuroma maturing or ganglioneuroblastoma intermixed	not amplified	very low
			amplified	high
L2	< 18	any, except from ganglioneuroma maturing or ganglioneuroblastoma intermixed	not amplified	low to intermediate
	≥ 18	ganglioneuroblastoma nodular; neuroblastoma	not amplified	low to intermediate
			amplified	high
M	< 18		not amplified	low to intermediate
	< 18		amplified	high
	≥ 18			high
MS	< 18		not amplified	very low to high
			amplified	high

For high-risk neuroblastoma, an aggressive form of neuroblastoma with a high likelihood of relapse and poor prognosis, diagnosis relies on a combination of clinical evaluation, imaging studies, followed by histopathological examination, and molecular testing. To define the primary tumour extents, cross-sectional imaging via MRI or computed tomography (CT) are usually utilised. Gold standard for detecting primary and metastatic lesions remains to be a scintigraphy with [^{123}I]metaiodobenzylguanidine (MIBG) [41]. Due to its structural similarity to noradrenaline, MIBG selectively accumulates in tissues with rich adrenergic innervation, like most neuroblastomas due to their neuroectodermal and catecholaminergic origin. The uptake mechanism is based on the active transport via norepinephrine transporter, a monoamine transporter [42]. For tumours lacking an increased uptake of MIBG or whenever MIBG is not available, PET using the radiotracer [^{18}F]fluorodesoxyglucose (FDG) has proven to provide important diagnostic information while underperforming in stage 4 neuroblastoma [43, 41]. In a recent systematic review and meta-analysis, the higher maximum standardised uptake values SUV_{max} of FDG PET in neuroblastoma correlated with poor overall survival [44], thus providing additional value for the assessment of prognosis. In guidelines for nuclear medicine imaging in neuroblastoma, additional tracers as 3,4-dihydroxy-6-[^{18}F]-fluoro-L-phenylalanine (FDOPA) or (1,4,7,10-tetraazacyclododecane-1,4,7,10-tetrayl)tetraacetic acid

([^{68}Ga]DOTA) conjugated somatostatin receptor targeting peptides are named that are currently used in clinical practice [41].

Treatment is tailored to risk level and includes combinations of surgery, chemotherapy, radiotherapy, stem cell transplantation, immunotherapy, and differentiation therapy [32]. Despite the utilisation of these aggressive multimodal therapies, 5-year survival rate in high-risk neuroblastoma remains at approximately 50% [31, 45, 30]. Thus, current research efforts are focusing on the development of novel immunotherapeutic, and molecular targeted strategies. One promising target is the disialoganglioside GD2, which is abundantly expressed on neuroblastoma cell surfaces but largely absent in normal tissues [46, 45]. This tumour-associated antigen has become a key focus for monoclonal antibody-based immunotherapy with agents as Dinutuximab and Naxitamab that have shown to enhance adaptive immunity and partly restore tumour cell phagocytosis [47, 45]. Recently, efforts were made to radiolabel GD2 with [^{64}Cu] for a radioimmunotherapy as a dedicated theranostic approach showing the feasibility of the method as well as a first preclinical test in neuroblastoma-bearing mice [48]. Other targets include, but are not limited to, chimeric antigen receptor-expressing T cells, or targeted therapies, such as ALK inhibitors [32].

1.1.2.1 Modelling Neuroblastoma: Cell lines LAN-1 and SH-SY5Y

The LAN-1 cell line (ACC 655, DSMZ, Germany) is a human-derived neuroblastoma line established in 1977 from a bone marrow metastasis of a two-year-old boy with stage 4 disease [49]. Genetically, LAN-1 carries approximately 60-100-fold MYCN gene amplifications [50], while harbouring an activating ALK F1174L mutation, which drives ALK signalling [51], but without ALK gene amplification [50]. This cell line is extensively characterised [52] and utilised for neuroblastoma ALK targeting [53]. *In vivo*, LAN-1 cells showed tumorigenic potential in an immunodeficient mouse xenograft model with LAN-1 tumours developing rapidly and responding to treatment with growth suppression [54]. More recently, a bone metastasis model derived from LAN-1 xenografts has been established, enabling the analysis of phenotypic and biochemical changes in tumour cell populations during metastasis [55]. Besides, LAN-1 is a valuable preclinical model for studying alternative radiotracers due to its lack of MIBG accumulation [56, 57].

The cell line SH-SY5Y (ACC 209, DSMZ, Germany) is a human-derived neuroblastoma subclone of SK-N-SH, originally isolated from a bone marrow metastasis of a 4-year-old girl [58]. Established in 1970, this cell line is now widely used and extensively characterised for neuroscience and neuroblastoma research [59–63]. SH-SY5Y is MYCN nonamplified and a relevant ALK mutant neuroblastoma model for ALK-inhibitor research, harbouring the ALK F1174L mutation [64, 65]. Early studies indicated two morphologically distinct phenotypes derived from the parental differentiated SK-N-SH cells that can be divided into neuroblast-like cells and epithelial-like cells. The neuroblast-like cells were positive for the catecholaminergic neuron markers tyrosine hydroxylase and dopamine-β-hydroxylase, whereas the epithelial-like

morphologic cells lacked these enzymatic activities [66]. Undifferentiated SH-SY5Y generally exhibit characteristics of immature catecholaminergic neurons [67–69].

1.2 Medical Imaging Techniques

In the following, medical imaging modalities that are frequently utilised in the diagnosis, therapy monitoring and detection of recurrence or metastasis for the cancer types discussed in chapter 1.1 will be introduced.

1.2.1 Magnetic Resonance Imaging

MRI is a non-invasive imaging modality that offers high-resolution visualisation of soft tissues and usually enables a precise tumour localisation, evaluation of extent, and biological characteristics, as cellular density or perfusion, in the body using its magnetic properties. Conventional MRI works by detecting signals from hydrogen nuclei (protons) that are abundantly distributed in tissues, fat, grey and white matter of the brain, blood, as well as several other fluids, primarily due to the high concentration of water, but also from protons of other molecules. The protons align along the strong external magnetic field, resulting in a net magnetisation of the tissue. This net magnetisation can be manipulated by an external radiofrequency pulse which tilts the protons away from their orientation along the magnetic field. Once the radiofrequency pulse is switched off, the protons return to equilibrium, which is described by the relaxation times T1 and T2 that are characteristic for different types of tissue: The T1 relaxation time is longitudinal, emphasizing differences in how quickly protons realign with the magnetic field, making a T1-weighted image show fat in bright and fluids in dark. T2 relaxation time represents how quickly protons dephase in the transversal plane and how spins decay of transversal magnetisation due to the recovery of longitudinal magnetisation. Thus, in T2-weighted images, fluids appear bright and fat dark [70].

In brain imaging, contrast enhancement typically involves the intravenous injection of gadolinium-based contrast agents, which shorten local T1 relaxation times. As these agents cannot cross the intact BBB, enhancement only occurs in regions of the brain where the BBB is disrupted, such as in some brain tumour types. Typically, MRI in brain tumour patients combines T1-weighted sequences with contrast agents, fluid-attenuated inversion recovery (FLAIR), and/or T2-weighted sequences to visualise BBB disruption, oedema, and other pathological changes.

1.2.2 Positron Emission Tomography

PET is a functional imaging modality that reveals metabolic or physiological activities. For this, a molecule that normally participates in biological processes is radioactively labelled with a positron (β^+) emitting isotope, to form a so-called radiotracer. After application into the subject, the location of radioactive decay and therefore the radiotracer distribution can be tracked and quantified inside the body.

The principle of PET, visualised in Figure 2, is based on a physical effect called annihilation. The radiotracer, accumulated in specific tissue, undergoes β^+ decay, whereby a proton is converted into a neutron under the emission of a positron. This positron travels a small distance through the tissue, until it collides with an electron of some atom present in the tissue, leading to the conversion of their mass into energy. This process of annihilation results in the simultaneous emission of two gamma photons with an energy of 511 keV into opposite directions at an angle of about 180°. The PET scanner consists of a ring of scintillation detectors which detects these gamma photons in coincidence, converts their energy into visible light and finally into an electrical signal. Using several correction methods and mathematical image reconstruction techniques such as filtered backprojection or ordered subset expectation maximisation, a quantitative, tomographic representation of the distribution of the radiotracer can be computed [70].

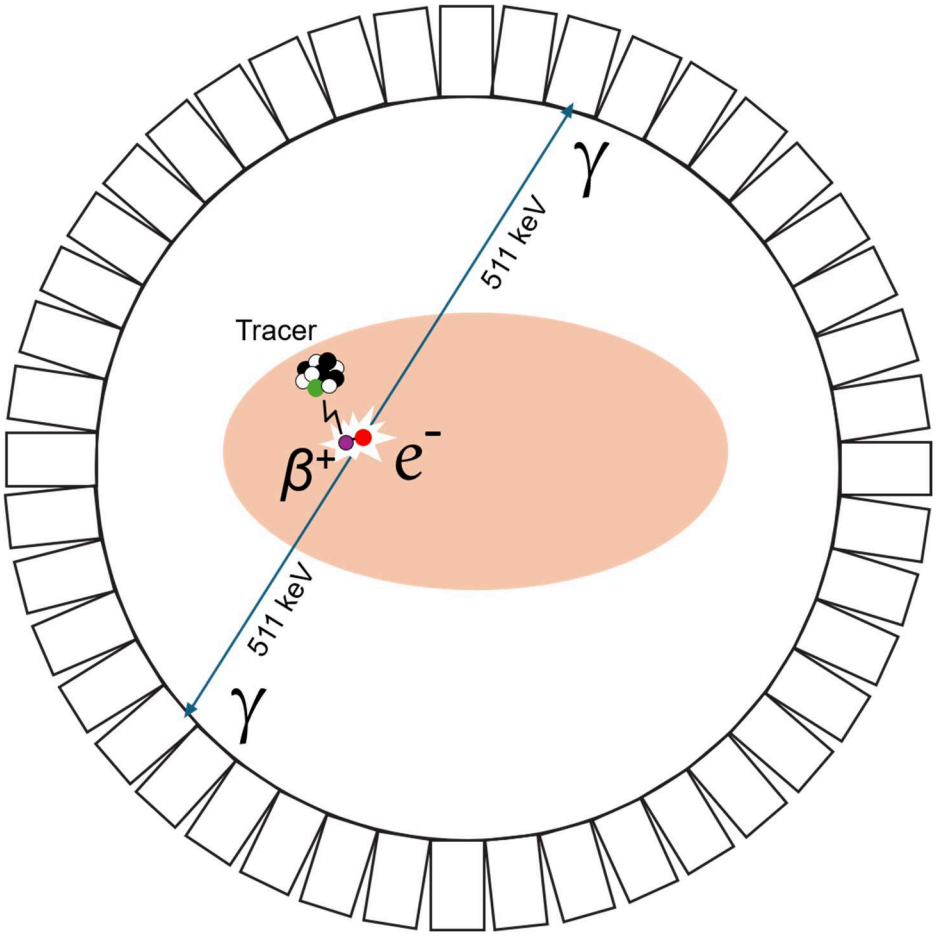

Figure 2: Schematic representation of PET principle. The tracer, accumulated in specific tissue, undergoes β^+ decay, whereby a proton is converted into a neutron under the emission of a positron. This positron travels a small distance through the tissue, until it collides with an electron of some atom present in the tissue, leading to the conversion of their mass into energy. This annihilation process results in the simultaneous emission of two gamma photons with an energy of 511keV into opposite directions at an angle of about 180°, that can be detected by the PET scanner scintillation detectors.

Usually, radioactive atoms with a short half-life are chosen for PET tracers, as [^{18}F], an unstable isotope of the element Fluorine with a half-life of about 110 minutes, or [^{68}Ga], a Gallium isotope with a half-life of 68 minutes. Also, only a small quantity of these radioactive atoms is needed for a PET measurement, making it a safe imaging method. Depending on the molecule attached, various targets can be analysed, as described in detail in Chapter 1.2.2.1. In general, a radiotracer is picked to show specific biological processes or molecular targets *in vivo*; for example, for cancerous tissues a radiotracer should ideally have a high specificity for tumour tissue, while showing a low uptake in healthy tissue. Due to the relatively low spatial resolution of PET, the combination with structural imaging such as computed tomography or MRI is particularly valuable for a precise anatomical localisation of regions with an increased radiotracer uptake.

1.2.2.1 Selection of Radiotracers for Tumour Diagnostics

Several radiotracers are employed in tumour diagnostics, each with distinct advantages and limitations. This chapter provides an overview of utilised PET or single photon emission computed tomography (SPECT) tracers and their value for glioma or neuroblastoma diagnostics.

For neuroblastoma, the most commonly used radiotracer is [^{123}I]MIBG in a scintigraphy or SPECT measurement. With a sensitivity in the range of 88-92% and a specificity of 83-92% [71], this radiotracer offers a high accuracy for detecting metastatic lesions, differentiating residual primary tumour from post-therapy changes, assessing response of bone marrow metastasis to treatment, and surveillance of relapse [71, 41]. As there are limitations in the availability of [^{123}I]MIBG SPECT among clinics, several other radiotracers for PET measurements have been evaluated and accepted for neuroblastoma evaluation [41].

The most commonly used PET radiotracer, reflecting mainly glucose metabolism and thus providing high uptake for many cancers, is [^{18}F]fluorodeoxyglucose (FDG) [70]. For stage 1 and 2 neuroblastoma, FDG provides important information for detecting malignant tissue, as well as therapy management. It delineates proficiently tumours in the chest, abdomen, and pelvis. FDG is used whenever MIBG is not available or whenever patients show low MIBG uptake [43, 44]. For glioma, this radiotracer shows severe limitations due to the high physiological glucose uptake in the grey matter, reducing the contrast and thus the tumour-to-background ratio (TBR) [72]. In contrast, white matter and most extracerebral tissues exhibit lower FDG uptake, allowing higher contrast in non-CNS regions. Moreover, FDG uptake is often increased in inflammatory regions or areas affected by radiotherapy, which further complicates image interpretation in the brain [72]. In Figure 3, a non-enhancing anaplastic astrocytoma with hypometabolic FDG is visualised in comparison to amino acid PET.

The amino acid tracer O-(2-[^{18}F]fluoroethyl)-L-tyrosine (FET) has proven to be a powerful radiotracer for brain tumour diagnostics, providing information on tumour metabolism, extent, therapy monitoring, and recurrence [73–76]. The uptake of FET is independent of the BBB integrity and several uptake pathways have been described.

Among them, the large neutral amino acid transporter (LAT) 1 and LAT2 function sodium independently [77] while there are also sodium dependent uptakes via system B^{0+} [78]. Most brain tumours show upregulated LAT1 expression to provide the tumour cells with essential amino acids to support the higher metabolic demands of these cells, whereas the normal brain tissue shows low tracer uptake, providing a high TBR [79]. Thus, LAT1 transport was long regarded as the main uptake route for FET; however, FET-negative glioma tissue did not show reduced LAT1 expression [80]. Thus, the mechanism of FET uptake remains to be further investigated [81]. Overall, FET demonstrated a sensitivity of 79-98% and specificity of 37-99% [82]. With regard to tracer sensitivity, about 30% of WHO grade 2 gliomas exhibit no amino acid uptake [83, 84]. Besides, also photopenic defects might occur, where the FET uptake of the tumour is even lower than in healthy brain tissue. This finding mainly occurred in non-enhancing gliomas harbouring higher CNS WHO grades [85].

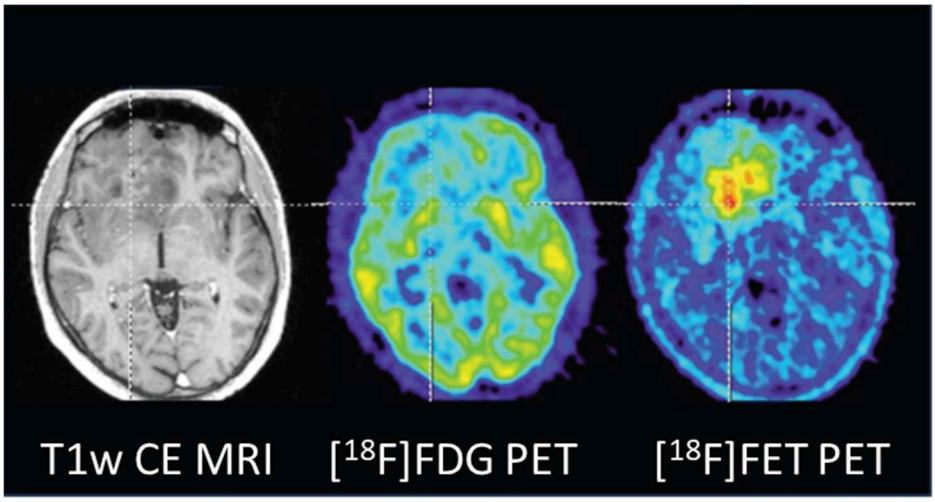

Figure 3: Comparison of MRI, FDG, and FET PET in a patient with a non-enhancing anaplastic astrocytoma. While the tumour does not show contrast enhancement (CE) on the T1-weighted MRI (left) or an increased uptake of FDG (centre), a metabolically active tumour was revealed by FET PET (right). Image adapted from Galldiks et al. [72].

Another amino acid analogue with high relevance for metabolically active brain tumour tissue identification is 3,4-dihydroxy-6-[^{18}F]-fluoro-L-phenylalanine (FDOPA). FDOPA is approved in many European countries for the detection of suspicious recurrence or residual disease in primary brain tumours [72]. Similar to FET, FDOPA exhibits generally low uptake in healthy brain tissue, but demonstrates additional uptake in brain regions with high concentration of tyrosine hydroxylase, as in the basal ganglia [75, 86, 87]. This additional uptake appears because FDOPA serves as a substrate of catechol O-methyl transferase and aromatic amino acid decarboxylase, converting FDOPA to 3-O-methyl-6-fluoro-L-DOPA and [^{18}F]fluoro-dopamine, respectively. Similar to FET, the uptake of FDOPA is independent of the BBB and it is mainly transported by the LAT1 transporter [86]. FDOPA seems not to be metabolised in glioma cells [88]. The phenomenon of photopenic defects described for FET in some gliomas has also been observed for FDOPA [89, 84]. With regard to neuroblastoma, FDOPA has proven to be a valuable diagnostic tool for identifying tumours with elevated catecholamine metabolism with high accuracy [90–92, 41].

Lastly, the [^{68}Ga] labelled quinoline-based small molecule fibroblast activation protein inhibitor (FAPI-46) is a radiolabelled inhibitor for FAP, a type II transmembrane glycoprotein that plays an important role for the remodelling of extracellular matrix. Thus, the radiotracer is relevant in processes where FAP (over)expression is targeted, as in inflammatory diseases [93, 94]. Also, cancer-associated fibroblasts could be found in various cancer entities, including glioma [95, 96]. Although the radiotracer is not able to cross the intact BBB, this target is of special interest in the research of embryonal models, as FAP is implicated in tissue remodelling during embryogenesis and in reactive stromal cells [97]. Thus, its evaluation for accessing potential limitations of embryonal models that do not replicate a mature biological system is of special interest in this thesis.

1.2 Preclinical Research with Animal Models

The utilisation of animal models in biomedical research has been, and still is, an essential tool for advancing our understanding of human biology and disease. To date, animal experiments have proven to be indispensable for meaningful *in vivo* research in preclinical tumour modelling and imaging [98, 11]. Rodent models have been widely utilised for *in vivo* oncology research, offering the often-needed complex metabolic routes and organ-specific challenges as the BBB to address all questions of new approaches [98, 99]. For accessing the BBB integrity status in rodents, two main experimental approaches can be used. First, comparable to patients, contrast-enhanced T1-weighted MRI can be utilised [100]. Also, the azo dye Evans Blue can be used in a terminal setting, where the brain has to be extracted for assessing the BBB status. Evans Blue has a high affinity to serum albumin, fluoresces with excitation peaks at 470 and 540 nm and has an emission peak at 680 nm [101]. The azo dye is not able to pass the intact BBB once bound to serum albumin; thus, fluorescence in the brain after injection shows Evans Blue dye extravasation due to a disrupted BBB [102]. In several studies, this dye has been utilised for assessing BBB disturbance in terminal rodent experiments [74, 103].

With raising ethical concern of animal use in experimental research, suitable alternatives must be found following the 3R principles [104] – “Replace, Reduce, and Refine”. The commitment to the 3R principles is firmly embedded in European legislation, with legal obligations to adhere to these principles outlined in Directive 2010/63/EU. Recently, a fourth R, “Responsibility”, has been introduced as well, emphasising the ongoing efforts of more ethical animal experiments [106].

1.2.1 Chick Embryos as Preclinical Model

In recent years, with advancing preclinical imaging methods and raising ethical concerns regarding animal experimentation, the chick embryo model has generated increasing interest in the field of neuroimaging and nuclear medicine.

The chick embryo model is ethically preferential compared to the use of rodent models, as avian embryos are traditionally regarded as being at a lower phylogenetic level. Legally, the avian embryos are not protected under European law on the protection of animals used for scientific purposes, as introduced in detail in Chapter 1.2.1.3. Thus, experiments with chick embryos are less restricted and can be performed quicker than rodent experiments that need study approvals by authorities. Besides, economic advantages can be considered, with lower costs and minimal animal husbandry requirements, provided that experiments are conducted before hatching. Another positive aspect with high importance in xenograft cancer research is the embryo's natural immunodeficiency that allows for tumour transplantation without immune responses in the beginning, as the chick immune system only begins to function about two weeks into the development. By embryonic development day (EDD) 18, chick embryos are considered immunocompetent [107–109]. However, limitations arise from the avian background, as mammals are generally considered to be more closely related to humans in terms of physiology and disease biology; thus, the translational relevance must be carefully assessed. Also, many reagents including antibodies or primers are not compatible with avian species [110]. Another limitation arises from the experimental timeframe. As chick embryos would hatch after around 21 days, experiments need to be terminated beforehand, limiting the usability of slow-growing tumour types or long-term treatment evaluations.

In the following subchapters, the main stages of chick development will be introduced, together with the formation of the chick chorioallantoic membrane (CAM). Afterwards, a short overview of the state of the art in cancer research and imaging will be given, followed by the ethical and legal perspective for chick embryo experiments in Europe and Germany.

1.2.1.1 Chick Embryo Development

Ever since Aristotle recognized the chick embryo as an ideal model for embryological experiments, the chick embryos have been classified by the length of incubation, except for the first three incubation days, where more detailed characteristics have been in place. However, there is no linear correlation between chronological and structural age in embryos even when placed in an incubator at the same time. Reasons for this are several external factors, such as the time lapse between the hen laying the egg and the start of incubation, or the individual size of eggs. Thus, in 1951, Hamburger and Hamilton described the chick embryo development based on morphological stages, previously described by several other researchers such as Duval in 1889 or Keibel and Abraham in 1900 [111]. This combination work of illustration and description of chick embryos on the various Hamburger-Hamilton (HH) stages has developed to be the main descriptive atlas for staging chick embryos worldwide. For experiments on the embryo itself, these stages are considered; in studies on the CAM, the chronological age remains to be the main descriptive variable. Also, it has to be considered that the HH staging defines start of incubation time with day 0, whereas commonly for CAM, the day of incubation start is normally defined EDD 1.

The Hamburger-Hamilton stages range from starting the incubation on day 0 with HH stage 1 to a newly-hatched chick at HH stage 46. In this thesis, the focus of chick embryo studies is laid onto the brain; thus, the main HH stages of brain development and relevant days for intracerebral tumour inoculations are regarded in the following.

Starting about 24 hours after incubation, the anterior end of the neural tube enlarges to form the brain. By stage 9, the formation of optic vesicles starts, leading to stage 10, where the brain has three distinct primary regions: the prosencephalon (forebrain), mesencephalon (midbrain) and rhombencephalon (hindbrain). In the following stage 11, the rhombencephalon divides into the metencephalon (cerebellum and pons) and myelencephalon (medulla oblongata). By stages 12-13, the forebrain divides into telencephalon and diencephalon. The mesencephalon increases in size by about stage 18, which is approximately EDD 4, growing clearly marked off posteriorly from the rhombencephalon by the meso-metencephalic fold [112]. At stage 18, cerebral hemispheres are formed from the telencephalic vesicle. Regarding the whole embryo, a bend from the tail-region begins to extend into the lumbo-sacral region at stage 20. Limb-buds are distinctly larger than the wing-buds. The allantois is on average of the size of the midbrain and a faint greyish hue of eye pigment can be seen. In stage 21, the allantois grows in size and the eye pigmentation becomes more prominent. At stage 22, which is approximately 3.5-4 days after incubation start and thus, about EDD 4.5-5, the allantois extends to the head and may overlap the forebrain [111]. The mesencephalon starts projecting over the metencephalon. At stage 27, the differentiation of the optic lobes from the mesencephalon starts. During further development, the walls of the rhombencephalon as well as of the metencephalon become thicker as the two halves of the cerebellum form. By EDD 10-11, the two halves enlarge and fuse together in the midline. The brain shape changes until stage 44, or at EDD 19, where the cerebral hemispheres enlarge, while the size of the optic lobes decreases [112].

For the growth and development of a chick embryo, several extra-embryonic membranes are necessary (Figure 4): First, the yolk sac encloses the yolk and is constructed to pass partially digested yolk into the embryonic blood stream. Also, the amnion is needed for the embryonal development. This sac surrounds the embryo and secretes fluids to cushion the embryo and to prevent dehydration. Lastly, the chorioallantoic membrane is an extra-embryonic membrane with three functions for the embryo. It is needed as respiratory exchange, stores nitrogenous waste products of the embryo, and is important for calcium transport to the embryo. This membrane is a widely-accepted research tool for tumour engraftments and thus relevant for this thesis, so its formation and development is described in the following in more detail [112].

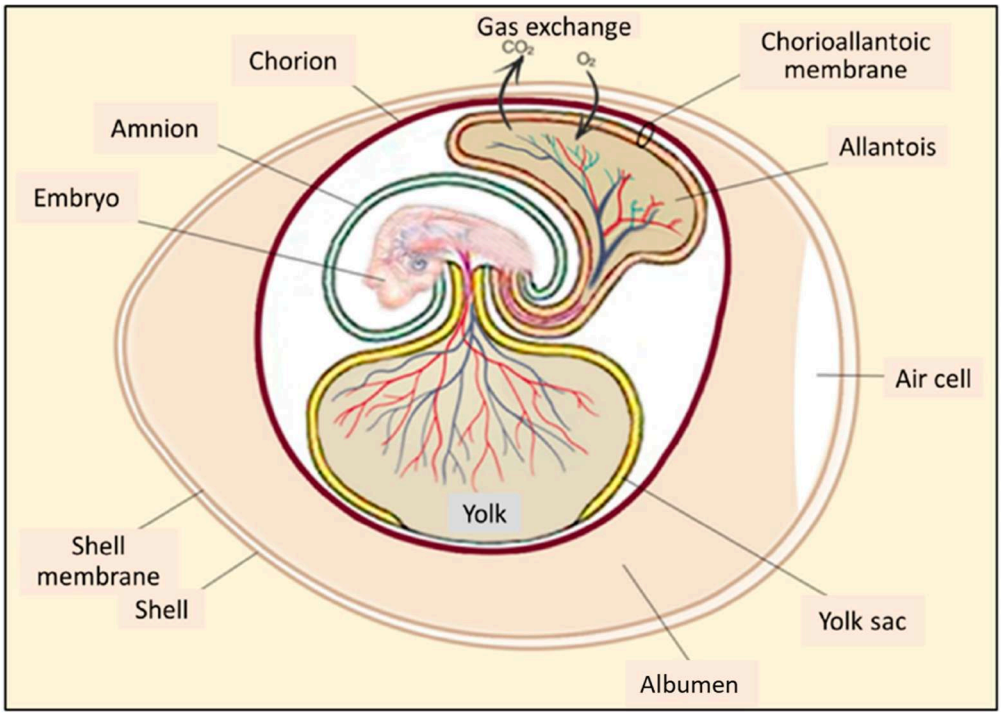

Figure 4: Illustration of membranes and blood circulation system of a chick embryo on EDD 7. Image adapted from Chen et al. [113].

At stage 12, the tissues amnion and chorion are formed and start to overlap the forebrain. The outer part will become the chorion, while the inner part will become the amnion. When the chorion and the allantois come into contact, they fuse and form the chorioallantoic membrane (CAM). At about EDD 7-8, the allantois has grown to a balloon-like structure outside the body, which then fuses with the inner layer of the chorion. The CAM consists of three layers: the ectoderm from the chorion, the mesoderm, where the fusion of mesoderm from chorion and allantois happens, and the endoderm from the allantois. The growing CAM then rapidly spreads over the surface until it is pressed against the shell membrane, allowing for gas exchange through the egg pores via its rich vascular system. Also, calcium from the shell is transported to the embryo for ossification. At hatching, the CAM stays within the discarded shell [112].

1.2.1.2 State of the Art for Preclinical Chick Embryo Cancer Research

In recent years, the chick embryo model has gained attention as alternative for rodent models in preclinical cancer research [114, 115].

The CAM is a widely accepted research tool for tumour engraftments, with various studies on tumorigenic aspects as angiogenic and metastatic potentials [116–119]. Also, several anticancer drugs have been evaluated in this model [120–123]. Besides, *in vivo* imaging techniques, like MRI and PET, have been tested in chick embryos, allowing for real-time monitoring of tumour growth and effects of treatments [124–128].

In the field of neuroblastoma, Ribatti and colleagues pioneered chick embryo CAM studies with neuroblastoma cell lines in 1998, demonstrating the functionality on the CAM and showing the cell lines' angiogenic capacity [129]. Four years later, the group

demonstrated the growth of further neuroblastoma cell lines as well as the growth of patient derived xenografts, and correlated the angiogenesis on the CAM with the MYCN amplification status [65]. Since then, several studies were performed for the utilisation of the chick embryo CAM in neuroblastoma research, not only for studying the tumour biology, but also for the evaluation of new therapeutic approaches: antitumor drug evaluation was comparable to results from tumour-bearing mice [130, 131]. In another study, neuroblastoma cells were embedded in Matrigel and pipetted onto the CAM, revealing the expression of angiogenic and angiostatic genes which are characteristic for human disease, thus, indicating for a good experimental model of high translational relevance in the field of anti-angiogenic research [132]. Thus, the chick embryo CAM model has shown its value as preliminary screening tool using neuroblastoma cell lines as well as patient-derived xenografts for the research of tumorigenicity, drug sensitivity and resistance, metastasis, and angiogenesis [133].

While the CAM tumour model provides a convenient and rapid way to study the early tumour stages like growth, angiogenesis, and metastatic potential, intracerebral tumour implantation into developing chick embryo brains provide a more realistic model of the interactions between brain tumours, e.g. gliomas, and the surrounding brain tissue *in vivo*. In the latter approach, cells are implanted into the neural tube of developmentally early chick embryos, allowing the growth and interaction of implanted tumour cells in a more sophisticated *in vivo* model [134]. With another methodology, brain tumour cells were pressure-injected into the midbrain on EDD 6 which also led to the growth of intraventricular tumours [135]. In a method article, Pastorino and colleagues also utilised EDD 6 old chick embryos for the injection of glioblastoma cells as well as glioma stem cells, with intracerebral tumour validation via immunofluorescence after finalisation of experiments on EDD 15 [136].

1.2.1.3 Ethical and Legal Considerations for Chick Embryo Experiments in Germany and Europe

Russel and Burch already described the utilisation of chick embryo experiments as replacement strategy comparable to the use of tissue culturing in 1959 [104]. Based on today's knowledge on nociception in chick embryos, it can no longer be regarded as a mere tissue culture.

Still, today, chick embryos are not protected by animal welfare laws for scientific research, under neither European nor German law: Both the Directive of the European Parliament and of the Council on the Protection of Animals used for Scientific Purposes (Directive 2010/63/EU), as well as the German Ordinance on the Protection of Animals Used for Scientific Purposes (German: "Tierschutzversuchstierverordnung" TierSchVersV, § 14) explicitly protect living non-human vertebrate animals, including larval forms that feed independently and foetal forms of mammals in the last third of their development [105, 137]. Also, live cephalopods are protected in the European

Law [105]. Thus, foetal forms of avian species are currently not covered by these regulations.

To address animal welfare concerns, the German law has changed in 2022 to prohibit the culling day-old male chicks in food production. Thus, an exploratory study was conducted in three subparts to narrow down when chick embryos acquire nociception [138–140]. In the first part of the study, cardiovascular responses to mechanical noxious stimuli were tested [138]. For this, changes in blood pressure and heart rates in response to mechanical stimuli at the base of the beak versus a light touch on the beak were examined in chick embryos of EDD 7 to 18. Weiss and colleagues found cardiovascular changes after the noxious mechanical stimulus in chick embryos of EDD 16 onwards, indicating a nociceptive response [138]. In the second part, the development of the chick embryo brain was examined by EEG recordings. Noxious stimuli were applied while hyperpallial brain EEGs were recorded. Although no nociceptive responses were documented, an onset of physiological neuronal signals could be found at EDD 13. Thus, EDD 13 was considered the earliest embryonal stage for being able to process pain [140]. The last part of the study examined the movements of chick embryos of various developmental stages before and after the application of noxious stimuli. The earliest stage for a detectable response after an applied stimulus was found on developmental day 15. Most noticeable were movements from the beak in response to noxious stimuli [139]. Based on those results of nociception, there was an extension to the German animal protection law for chick embryos in 2024: § 4c (3) of German Animal Welfare law (German: “Tierschutzgesetz”, TierSchG). This addition states the prohibition of killing of chick embryos from EDD 13 onwards when or after a method of sex determination was applied [141].

2 Aim of this Study

Despite the increasing use of the chick embryo model for neuro-oncological evaluations, several methodological and translational aspects remain to be adequately addressed and standardised for reproducible and valuable research as more ethical alternative to rodent models.

In the field of brain tumour research, orthotopic implantations are oftentimes needed to reflect the complex metabolic pathways and organ-specific challenges, such as the blood-brain barrier [99, 98]. Only few studies have been published in this field utilising chick embryos [135, 134, 142, 143, 136], indicating technical challenges with only limited knowledge on mortality rates or feasibility of brain tumour imaging in respect to the translational relevance.

For research questions unaffected by blood-brain barriers or exact tumour microenvironment modelling, tumour engraftments on the extra-embryonic chorioallantoic membrane are already widely accepted as research tool for various purposes [118, 114, 119, 144, 145]. However, higher technical difficulties in regard to radiotracer experiments occur, with the risk of failed injections [128] or heavy bleedings during cannula removal [144] limiting the meaningfulness, robustness, and reproducibility of radiotracer experiments.

Aim of this study is to establish, characterise and analyse glioma and neuroblastoma tumour models in the chick embryo using radiotracer-based imaging for the feasibility and translational relevance in comparison to established rodent models or patients.

With this, the following questions shall be addressed:

1. Can intracerebral gliomas in the chick embryo model be successfully modelled and visualised using autoradiography with different PET radiotracers?
2. How do radiotracer uptake and kinetics in the chick embryo model compare to those observed in rodent models and patients?
3. Is the neuroblastoma CAM model suitable for reproducible radiotracer evaluations? Are there possible refinements to increase the robustness of CAM radiotracer studies?
4. How do the radiotracer uptakes derived from CAM neuroblastoma perform compared to the achieved values in neuroblastoma patients?
5. How does the radiotracer FET compare in respect to its neuroblastoma uptake to the clinically established radiotracers FDG and FDOPA in the chick embryo model?
6. In which aspects might the chick embryo model be considered an alternative to rodent models and what are its limitations?

3 Materials and Methods

3.1 Study Designs

3.1.1 Intracerebral Tumour Study for Glioma

An overview of the study design for intracerebral tumours is given in Figure 5. The cultivated glioma cells were implanted into the forming mesencephalon of the chick embryo on EDD 5, and placed back into the egg incubator until one day before PET in the third incubation week. MR imaging was then utilised to screen for adequately-sized brain tumours in T1-and T2-weighted images, and/or to evaluate BBB integrity after injection of a paramagnetic contrast agent. On the following day, PET imaging was performed in the most promising tumour-bearing chick embryos. The diluted tracer for each chick embryo was mixed with Evans Blue dye for additional *ex ovo* BBB evaluation. One hour after injection, the chick embryo was finalised, the brain extracted, and tissue prepared for *ex ovo* autoradiography. Histology and immunofluorescence staining were performed afterwards with sections in brain tumour region.

3.1.2 CAM Tumour Study for Neuroblastoma

The study design for the CAM tumour neuroblastoma study is summarised in Figure 6. After cultivation of neuroblastoma lines and inoculation on the CAM between EDD 8 and 11, PET measurements were performed in the third week after visual inspection of tumour growth on the CAM surface. Only when no tumour was observed macroscopically from the outside, T1- and T2-weighted MR imaging was performed to screen for suitable candidates for next-day PET measurements. In each subgroup of neuroblastoma cell lines, three chick embryos were injected with the corresponding radiotracer. In one of the three subjects, PET imaging was performed directly after injection for thirty minutes. For the other two subjects per group, the chick embryos were placed back into the incubator post injection. As control group, three naïve chick embryos per radiotracer were measured with PET. All subjects were finalised one hour after radiotracer injection. The tumour tissues were extracted from the CAM, weighed, and prepared for autoradiography. The beheaded chick embryo was weighted, as well, and the amount of radiotracer inside the embryo was measured with a gamma counter for a proof of correct intravenous injection. After *ex ovo* autoradiography, histological and immunofluorescence stainings were performed.

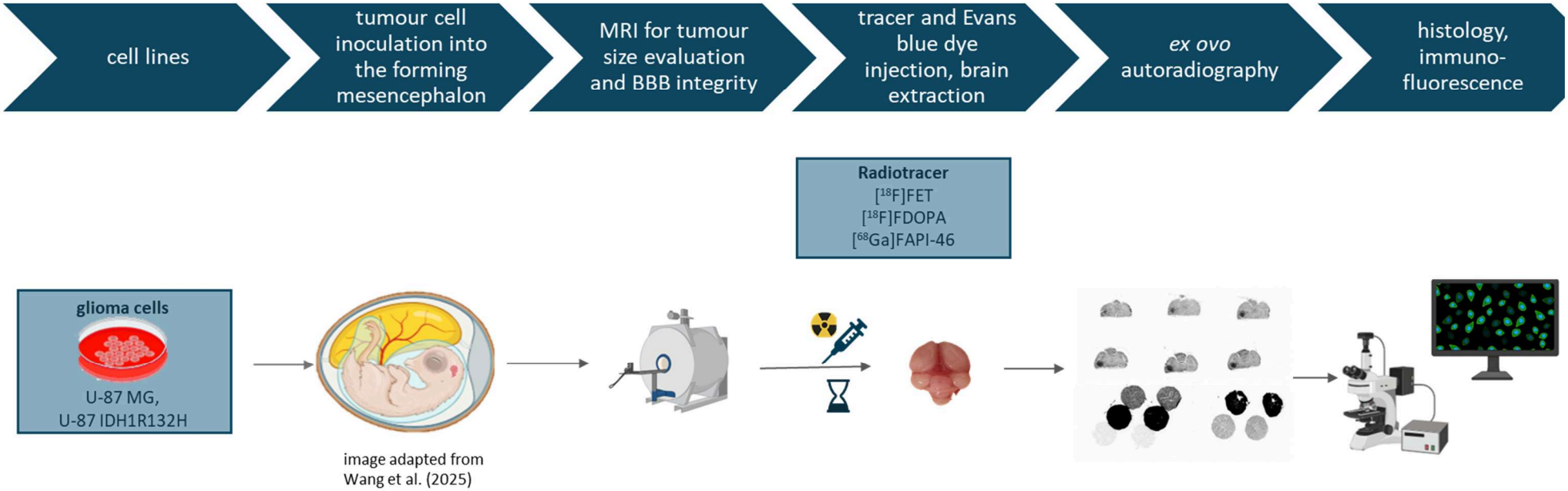

Figure 5: Overview of the intracerebral glioma study design. Chick embryos were inoculated with the respective glioma cells on EDD5. In the third week of incubation, MRI was performed for the evaluation of tumour sizes, as well as the evaluation of the BBB integrity after paramagnetic contrast agent injection. On the following day, the respective tracer was mixed with Evans Blue dye for an additional ex ovo BBB evaluation, and injected into the embryo. One-hour post injection, the chick embryo was finalised, the brain extracted, and ex ovo autoradiography was performed. Histological and immunofluorescence stainings were performed afterwards in tumour regions of the brain. Image created with BioRender.com.

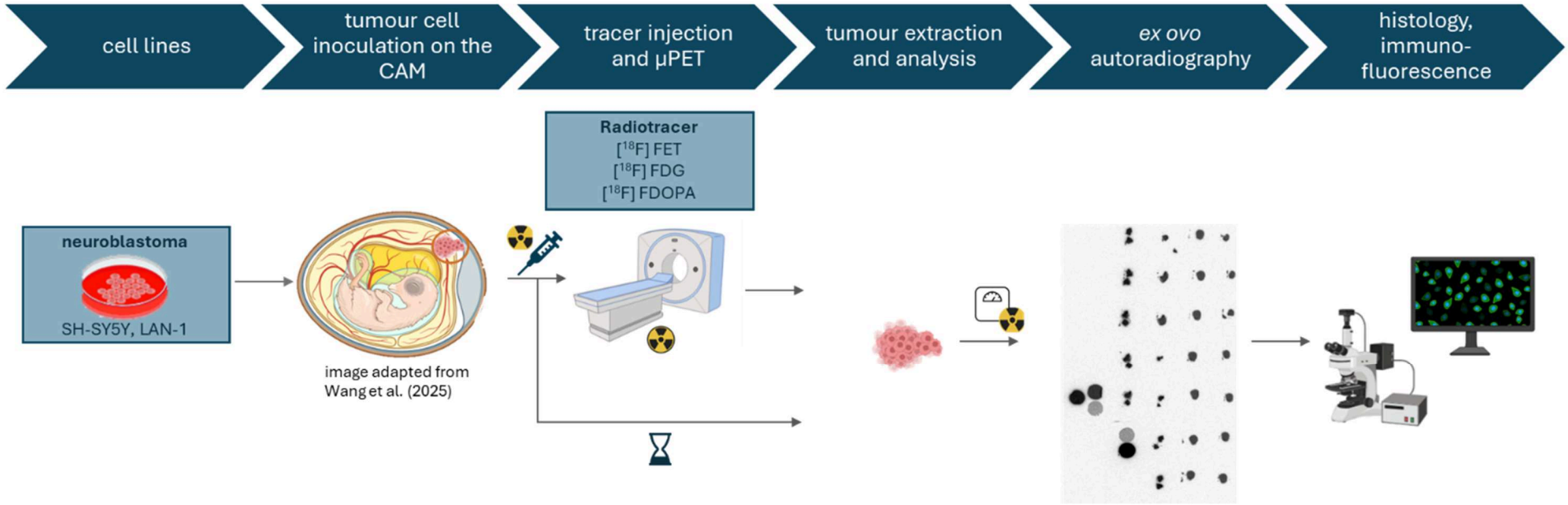

Figure 6: Overview of the CAM neuroblastoma study design. After tumour cell inoculation on EDD 8-11, tumour growth was visually inspected in the third incubation week on the day of PET. Three chick embryos per cell line were injected with the respective radiotracer. One of those three embryos was placed into the PET scanner, whereas the other two subjects were placed back into the incubator. One hour after injection, all chick embryos were finalised, the respective tumour was extracted and weighed. Tumour tissue was prepared for autoradiography. The chick embryos were weighted, and the amount of radioactivity inside the subject was measured with a gamma counter for proof of correct injection. Afterwards, histological and immunofluorescence staining were performed for the validation of human tumour tissue. Image created with BioRender.com.

3.2 Cell Culture

A list of the utilised cell culture materials with their respective suppliers can be found in Table 2.

Table 2: List of cell culture materials with suppliers.

Material	Supplier
Minimum Essential Medium Eagle	Sigma-Aldrich, Germany
Roswell Park Memorial Institute (RPMI) 1640	Sigma-Aldrich, Germany
MEM non-Essential Amino Acids	Biowest, France
Dulbecco's Phosphate Buffered Saline	Sigma-Aldrich, Germany
Trypsin – EDTA Solution (10x)	Sigma-Aldrich, Germany
L-Glutamine (200 mM)	Sigma-Aldrich, Germany
Foetal Bovine Serum (FBS), South America origin	PAN-Biotech, Germany
Penicillin-Streptomycin (10.000 U penicillin + 10 mg Streptomycin per mL)	Sigma-Aldrich, Germany
Matrigel® Matrix, Basement Membrane, Growth Factor Reduced	Corning, USA

All cells were cultivated at 37°C and 5% CO_2. An overview of utilised cancer cell lines with their corresponding tumour origin, growth types as well as their respective culturing media can be seen in Table 3Table 3. The cell culture solutions were prewarmed to 37°C before use.

All cells were stored in liquid nitrogen at -196°C in their respective culture medium with additional 10% dimethyl sulfoxide (DMSO). For thawing, the respective vial was rapidly warmed to 37°C, diluted in fresh medium and centrifuged for 3 minutes at 600 g to remove the DMSO. The cell pellet was then resuspended in fresh medium, and culturing was performed in T-25 and T-175 cell culture flasks. When confluent, the old medium was removed, adherent cells were washed in Dulbecco's Phosphate Buffered Saline (DPBS), and trypsinated with 1-fold trypsin/ethylenediaminetetraacetic acid (EDTA) for up to 8 minutes until the adherent cells have detached from their adherent growth in the flask. For cell cultures with additional suspension cell growth properties, the medium and the washing steps were centrifuged, and the subsequent pellet was added in the following passages, as well. To inactivate the trypsin/EDTA, fresh culture medium was added, cells collected and centrifuged for 3 minutes at 600 g. The cell pellet was then resuspended and cultured in a ratio of up to 1:8. The subsequent cell passages were marked. All experiments were performed in cell passages below 20.

Table 3: Overview of utilised cancer cell lines with subsequent cancer- and growth types and culturing media.

Cell line	Cancer type	Growth type	Culture medium
U-87 MG (HTB-14™, ATCC ®)	Likely Glioblastoma	adherent	Minimum Essential Medium Eagle, containing 10% foetal calf serum, 1% L-glutamine, 1% MEM non-essential amino acids, 1% penicillin/streptomycin
U-87 IDH1^{R132H} (HTB-14IG™, ATCC ®)	Glioma	adherent	Minimum Essential Medium Eagle, containing 10% foetal calf serum, 1% L-glutamine, 1% MEM non-essential amino acids, 1% penicillin/streptomycin
LAN-1 (ACC 655, DSMZ, Germany)	Neuroblastoma	slightly adherent and in clumps in suspension	Roswell Park Memorial Institute (RPMI) 1640, containing 10% foetal calf serum, 1% penicillin/streptomycin
SH-SY5Y (ACC 209, DSMZ, Germany)	Neuroblastoma	adherent and suspension	Roswell Park Memorial Institute (RPMI) 1640, containing 10% foetal calf serum, 1% L-glutamine, 1% penicillin/streptomycin

3.2.1 Glioma cell lines

The cell lines U-87 MG (HTB-14™, ATCC) and U-87 IDH1^{R132H} (HTB-14IG™, ATCC) were cultured in Minimum Essential Medium Eagle with 10% foetal calf serum, 1% L-glutamine, 1% MEM non-essential amino acids, and 1% penicillin/streptomycin at 5% CO_2 and at a temperature of 37°C.

Four days prior to the intracerebral implantation in chick embryos, the cells were counted using a Neubauer chamber and set to a concentration of 5,000 cells per 40 µl. Drops of 40 µl were then placed in the lid of a petri dish to allow hanging drop culturing. To ensure that the small droplets did not dry out, the petri dish was filled with medium. Four days after the incubation, cell spheres of approximately 50,000 cells have formed which are suitable for one injection. For this, the cell pellet was drawn in a volume below 1 µl under a binocular microscope (Leica M320 F12, Leica Microsystems CMS GmbH, Germany) into a neuro-syringe (Neuros™ 700/1700 Series, Hamilton, USA) that was connected to a stereotactic frame (Föhr Medical Instruments GmbH, Germany).

3.2.2 Neuroblastoma cell lines

The neuroblastoma cell line LAN-1 (ACC 655, DSMZ, Germany) was cultured in Roswell Park Memorial Institute (RPMI) 1640 medium with 10% foetal calf serum, 1% penicillin/streptomycin at 5% CO_2 and 37°C. Due to the only slightly adherent growth with suspension cells in clumps, the depleted medium as well as all washing steps were centrifuged and the corresponding cell pellets utilised together with the adherent cells. LAN-1 cells were utilised for CAM implantation on EDD 8. For this, the cells were collected and counted as described in Chapter 3.1 and set to a concentration of 2,500,000 cells per 25 µl. The cell vial was placed on ice, and 25 µl cell suspension was freshly mixed with 25 µl growth factor reduced Matrigel ® Matrix (Corning, USA) directly before implantation of 50µl per egg.

The metastatic neuroblastoma cell line SH-SY5Y (ACC 209, DSMZ, Germany) was cultured in RPMI-1640, containing 10% foetal calf serum, 1% L-glutamine and 1% penicillin/streptomycin in standard culturing conditions. Due to the adherent growth with additional suspension cells, the depleted media as well as all washing steps were centrifuged for 3 minutes at 600 g, and the cell pellet was added to the adherent protocol. For the utilisation of SH-SY5Y cells for CAM experiments, the cell inoculation took place on EDD10-11. Cells were collected, counted, set to a concentration of 2,000,000 cells per 20 µl, and cooled to 4 °C. Mixed 1:1 in growth factor reduced Matrigel ® Matrix, 40 µl of cell-Matrigel-suspension was utilised per egg.

3.3 Treatment of Fertilised Chicken Eggs

All procedures and interventions on chick embryos were performed in strict alignment to regulatory policy for German national and EU guidelines.

Specific pathogen-free fertilised chicken eggs for medical purposes (Valo BioMedia GmbH, Germany) were utilised for this study. Upon arrival, the eggs were stored at 17±2°C for at least 24 hours. Before incubation start, the eggs were warmed to room temperature (22±1°C) for 12 hours. The embryonic development was started on their sides at 37.8°C without turning with a relative humidity of 50-57% on embryonic development day (EDD) 1 (Favorit-Olymp 192, Heka, Germany). Generally, fertilised eggs were utilised within a week after delivery to decrease the risk of viability loss due to long storage. Besides, to decrease the risk of contaminations, windowing was performed under a clean bench. The water for humidity control was depleted and refreshed shortly before a new cohort of eggs was started. The incubator and all utilised instruments were rigorously cleaned with suitable disinfectants after each use and in-between cohorts. During handling of eggs and all openings of the incubator, disinfected gloves, clean lab coats, and FFP2 masks were worn to protect the eggs from ubiquitous germs that might decrease viability. Any symptoms of illness were exclusion criteria of entering the incubator room. A monitoring of temperature and relative humidity (rH) inside the incubator was carried out every 30 minutes for the whole incubation time using a data logger (testo 174H, testo, Germany). On EDD 5, the eggs were fenestrated to gain access to the embryo and sealed with adhesive tape,

as described in detail in the following chapter 3.2.1. Tumours were either inducted intracerebrally on EDD 5, or on the chorioallantoic membrane (CAM) on EDD 8-11, as explained in chapter 3.2.2. During experimental days, where the incubator was opened and thus disturbed repeatedly, humidity spikes of up to 85%rH were exhibited. To minimise these disturbances, a portable egg incubator was used on experimentation days, allowing the simultaneous incubation of ten eggs that need intervention and thereby reducing the number of openings of the main incubator while keeping the environment of the eggs in experiment more stable. With this, humidity spikes were reduced to a maximum of 61.4%rH. After the tumour induction, imaging was performed on EDD 17-20 (chapter 3.2.3), and experiments were finalised on EDD 18-20 (chapter 3.2.4).

3.3.1 Egg Fenestration

On EDD 5, a window was cut into the eggshell to access the embryo as shown in Figure 7. In short, the embryos have attached to the upper side of the sideways laying eggs within the first days of incubation. Thus, the air bubble that is naturally occurring on the blunt end of the egg must be relocated carefully to detach the embryo and act as a buffer to not cut into the embryo while cutting into the eggshell. For a clean environment, this process was performed in a clean bench whenever possible.

In more detail, batches of ten eggs were placed laying sideways for the procedure (A). With a candling lamp, the position of the embryo could be visualized as a darker orange structure (B) and was marked on the eggshell with an alcohol-proof marker. Also, the candling lamp was utilized to mark the position of the air bubble on the blunt end of the egg. The position of the air bubble on the blunt end of the egg was disinfected before drilling a small hole with a 0.8 mm engraving ball tip of a micro drill (Dremel Micro, Dremel Company, USA) (C). The eggshell dust was then wiped off the hole. A long 20G cannula (0.9 x 70 mm) was attached to a 5 ml syringe and inserted in a 45-90° angle into the hole (D). The cannula was utilised to scratch the inner eggshell membrane on the bottom of the sideways laying egg to allow the following relocation of the air bubble. In addition, 2 ml of albumen was aspirated to lower the fill level (E), before extracting the cannula. The egg was then rotated carefully so that the scratched inner eggshell was on the top which led to the relocation of the air bubble towards the middle of the egg. The egg was slowly turned back, and the air bubble was utilised to gently detach the embryo from the inner eggshell. This procedure was monitored with the candling lamp in the dark (F). The position of the window was disinfected, and a new hole was drilled into the eggshell at the new position above air bubble (G). Potentially, parts of the air bubble might be remaining at the blunt end of the egg. This occurrence can be checked with the candling lamp, which would show a bright circle at the blunt end. In this case, a Peleus ball was placed on the first drilled hole, and the remaining air was suctioned off. Afterwards, the hole on the side was closed with adhesive tape (H). With a 38 mm diamond cutting disc attached to the micro drill, a window of approximately 2.5 x 1 cm was cut into the eggshell, without disrupting the inner eggshell membrane (I) to prohibit the calcium eggshell particles from falling onto the embryo. The particles were wiped off with disinfectant wipes. With tweezers, the

inner eggshell membrane was pierced at one side, and the cut eggshell fragment was removed (J). To avoid drying out in the incubator, the window was sealed with adhesive tape (K). Lastly, the egg was marked with a number for clear identification (L) and placed back into the incubator until the next experiment.

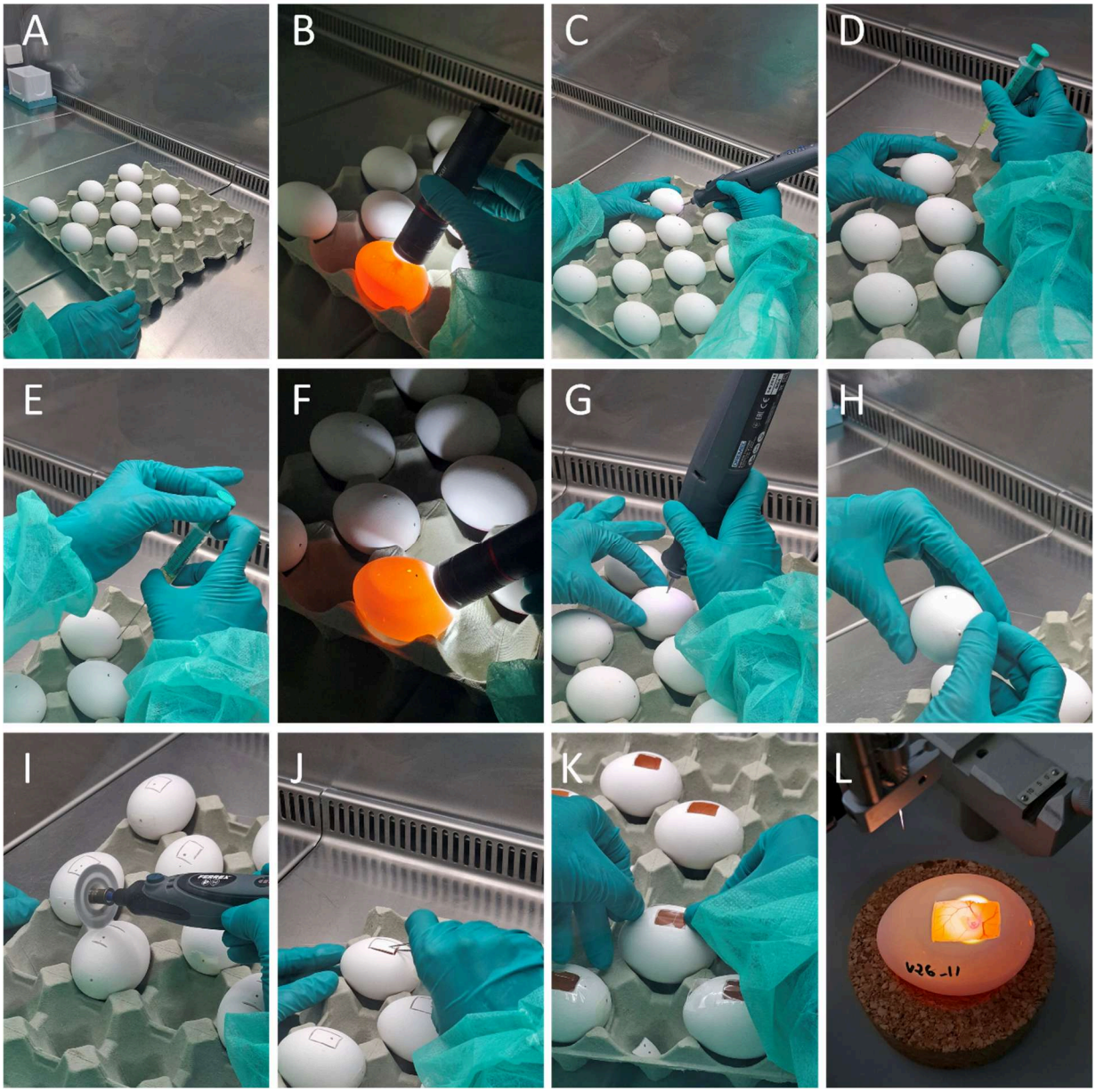

Figure 7: Overview of the fenestration process of chick eggs on embryonal developmental day 5. A: Batches of ten eggs were placed sideways, with the blunt ends facing to one side. B: With a candling lamp, the position of the embryo was marked on the outside of the eggshell. C: A small hole was drilled in the blunt end of the egg. D: A 20G cannula with syringe was inserted into the hole, scratching the inner eggshell membrane. E: 2 ml of albumen was aspirated to lower the fill level of the egg. F: After rotating the egg, the relocation of the air bubble was checked with the candling lamp. G: A small hole was drilled into the new position of the air bubble. H: The small hole on the side was closed with adhesive tape. I: With a diamond cutting disc, a window of approximately 2.5 x 1 cm was cut into the eggshell without disrupting the inner eggshell membrane. J: After cleaning off the eggshell fragments from cutting, tweezers were utilized to open the window. K: With adhesive tape, the new window was closed to avoid drying out. L: The eggs were marked with a clear identification number and were placed back into the incubator.

3.3.2 Tumour Induction

For the glioma studies, intracerebral tumours were generated for the possibility of higher translational relevance. For experiments of neuroblastoma, tumour cell inoculation on the CAM was chosen.

3.3.2.1 Intracerebral Tumour Induction

Intracerebral tumour induction was performed on EDD 5 under the binocular microscope. Embryos with delayed development, as optically visible through missing cervical flexure, non-observable allantois and missing eye pigments, were excluded from implantation; thus, implantation was performed on HH Stage 20 and older. The embryo was placed under the stereotactic frame with the connected neuro-syringe. The cells were drawn into the neuro-syringe directly before injection. The adhesive tape was opened, and the chorion was punctured and sliced with a sharp glass capillary at a position next to the embryo's head to avoid large opening of the chorion. In the next step, the spoon of a micro spatula was carefully introduced into the opening of the chorion and placed below the head of the embryo. With the sharp glass capillary, the amnion was ruptured at mesencephalon position by pressing and pulling the amnion against the spoon upwards towards the spatula. The ruptured ends of the amnion were then placed towards the end of the brain to expose the mesencephalon. With the head still resting on the spoon, a small hole was punctured into the mesencephalon with the glass capillary. The neuro-syringe was then lowered into the hole while the head was still resting on the spoon so that the amnion does not cover the hole. Otherwise, the flexible tip of the syringe cannot enter the brain. A correct placement of the syringe in the brain was checked via slightly adjusting the stereotactic frame left to right as well as slightly down. If the syringe was correctly inserted into the brain, the head would move left and right together with this repositioning. Slight downward movement into the brain would not change the orientation of the chick embryo head, if inserted correctly. The injection of the cells was performed slowly to avoid too high pressure in the brain. For hanging drop cultures, the syringe was shortly left inside the brain to avoid pulling out the cell pellet together with the syringe. For suspension cells, this waiting time after injection was prolonged to approximately 5 minutes for the cells to settle downwards. The procedure of injection as well as the extraction were carefully observed through the binocular for visual confirmation of cells not spilling. Then, the amnion was carefully placed over the brain again and the ruptured ends of the chorion were merged again, if possible. The window of the egg was then covered again with adhesive tape, and the egg was re-entered in the incubator. The ruptured membranes usually healed within the next 2 days. A representative image of a chick embryo with a depiction of the implantation technique is visualised in Figure 8.

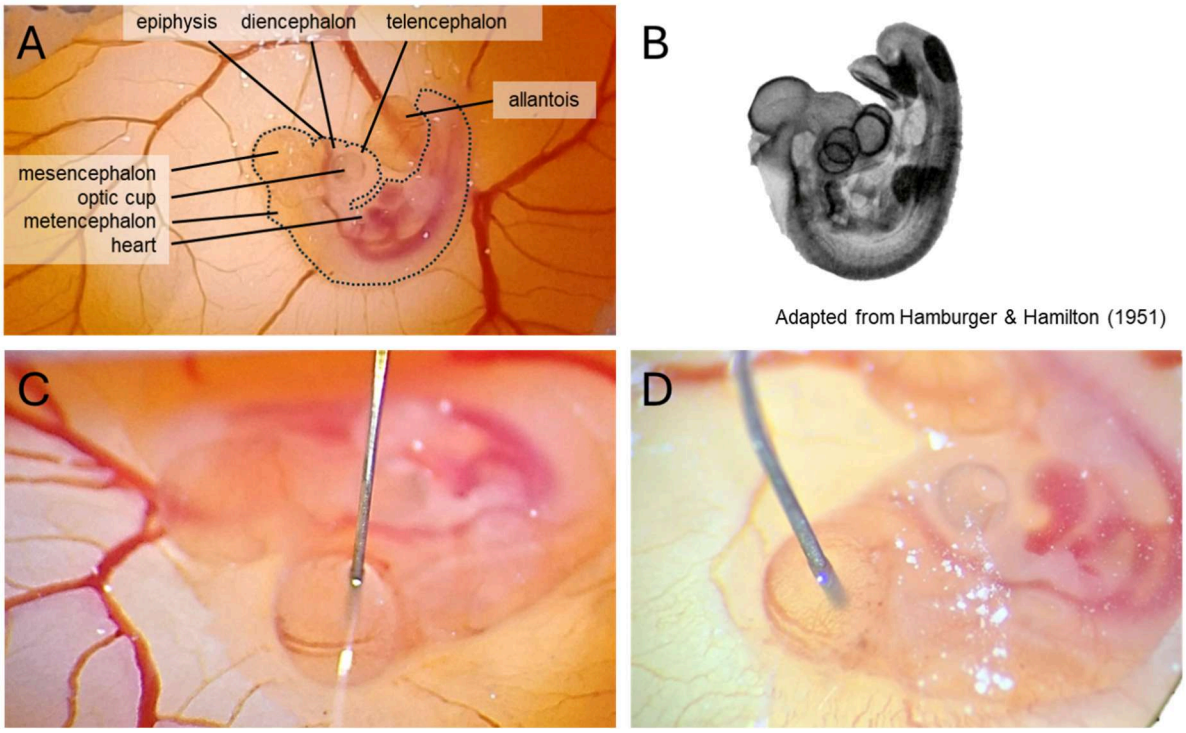

Figure 8: Overview of intracerebral tumour inoculation for chick embryos on EDD 5. Embryos of Hamburger Hamilton Stage 20 and older were utilised for the implantation, visible through the bending of the whole body, the pigmentation of the optic cup, and visible allantois (A). For better visualisation, an adapted comparative image to Hamburger Hamilton Stage 21 can be seen in B. In C and D, different orientations show the micro-syringes inserted into the forming mesencephalon.

3.3.2.2 Tumour Induction on the Chorioallantoic Membrane

Tumour induction on the chorioallantoic membrane was performed on EDD 8-11, depending on the tumour type. For better visualisation, the binocular was utilised for the procedure. Before start, flat silicone rings with an inner diameter of 9 mm were sterilised in 99% ethanol and subsequently allowed to dry until all residual ethanol has evaporated before use. With curved forceps, the silicone ring was gently placed on a region with small- to middle-sized veins and arteries merging. The silicone ring was then gently pressed onto the CAM to ensure close contact. The curved forceps were utilised to gently lacerate both small-sized veins and arteries inside the ring so that some micro bleeding could be observed through the binocular. Then, the cell-Matrigel suspension was added to the silicone ring. The egg was not moved for a few minutes to allow the Matrigel to harden so that the suspension is not spilled outside the ring. Then, the egg was closed with adhesive tape and placed back into the incubator. A photographic representation of CAM tumour inoculation can be seen in Figure 9.

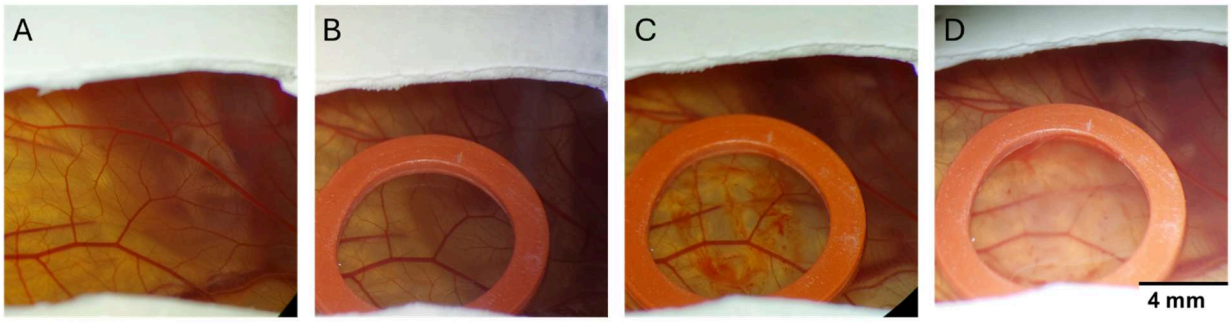

Figure 9: Overview of tumour cell inoculation technique on the CAM, exemplary on an EDD 10 CAM. A position of the CAM where middle-sized veins and arteries merge (A) was chosen for the placement of the silicone ring (B). Small-sized vessels inside the ring were gently lacerated to create micro-bleedings of the CAM (C). The cell-Matrigel solution was pipetted inside the ring, which turned opaque through hardening of Matrigel as well as highly concentrated cells (D).

3.3.3 Imaging

The imaging modalities MRI and PET were performed after tumour growth in the third week of embryonic development.

3.3.3.1 Preparations: Anaesthesia and Intravenous Injections

For all imaging modalities, movements of the embryo were mitigated by isoflurane (IsoFlo, Abbott, USA) anaesthesia. Anaesthesia was initialised for 5 minutes in 5% isoflurane in air in a small-animal gas chamber. During measurements, anaesthesia was either performed under constant flow of 2% isoflurane in oxygen, whenever the small-animal isoflurane vaporiser system (Isoflurane Vapor 19.1, Dräger, Germany) was available, or via pipetting liquid isoflurane on a tissue paper to reach approximately 2% isoflurane in the sealed chamber. Whenever possible, the temperature was maintained with an infrared lamp.

For intravenous injections, the eggshell was opened as wide as possible without damaging the CAM to facilitate the access. All substances were injected intravenously in middle-sized veins of the CAM, which are the light red vessels, in a flow direction from smaller to bigger vessels. Injections were performed with a 33G cannula connected to a 1 ml syringe. In case of radiotracer injections, the 1 ml syringe was inserted into a tungsten coating for radiation protection. For the injection, the CAM was held with curved forceps and slightly pulled towards the injector for cannula insertion into the vein. Volumes of 100 to 150 µl were injected over a time period of at least 20 seconds. For visual feedback on correct insertion into a vessel, 1 µl of 2% Evans blue dye, diluted in 0.9% NaCl, was added to the injection solution. Before pulling out the cannula, the vein was pinched with the curved forceps to minimise bleeding.

3.3.3.2 Magnetic Resonance Imaging

MRI was conducted using a 7 T clinical whole-body MRI scanner (Terra, Siemens Healthineers, Germany) on EDD 17-19.

The glioma study was conducted with a standard birdcage coil (Siemens Healthineers, Germany) with an inner diameter and length of 45 mm and 60 mm, respectively. The

coil and egg were fitted inside a tailor-made cylindrical plastic case with an inner diameter of 74 mm and a length of 160 mm.

For the neuroblastoma study, new in-house designed coils for chick embryo measurements were utilised and improved, as described in short in chapter 4.1 and in more detail elsewhere [146, 147].

For T1-weighted images, the standard MR sequence MP2RAGE was performed before and after injection of 30 µl of 0.5 mmol/ml gadopentetic acid (DOTAREM, Guerbet, France) as contrast agent into a vein of the CAM. The sequence had a repetition time (TR) of 4310 ms, echo time (TE) of 3 ms, with two averages and a resolution of 0.2 mm³ isotropic. The acquisition time was approximately 23 minutes. For T2-weighted imaging, a 2D turbo spin echo sequence was employed, with a TR of 6340 ms, TE of 52 ms with four averages, a slice thickness of 0.7 mm and an in-plane resolution of 0.1 x 0.1 mm². The acquisition time was approximately 14 minutes.

3.3.3.3 Positron Emission Tomography

For the glioma studies, dynamic PET scans were acquired with a Siemens InVeon scanner (Siemens, Erlangen, Germany) [148] or a Triumph II CT scanner (Northridge Tri-Modality Imaging, USA). Radiotracers labelled with [18F] were synthesised at the Institute of Neuroscience and Medicine Nuclear Chemistry (INM-5) of Research Centre Jülich, Germany, while [68Ga]-labelled radiotracers were synthesised at the Department of Nuclear Medicine, RWTH Aachen University Hospital, Aachen, Germany, all in accordance with Good Manufacturing Practice for clinical use. 15 ± 5 MBq were injected in a volume of up to 150 µl into each chick embryo for all radiotracers. For [^{18}F]-labelled radiotracers, image acquisition was performed for 65 minutes, whereas scans with [^{68}Ga]-FAPI-46 a duration of 30 minutes. FAPI scans were conducted by Dr. Carina Stegmayr. After injection of all radiotracers using the binocular microscope, emission scans were started with a time delay of 3-6 minutes. After the emission, 10-minute transmission scan (InVeon) or a low dose CT (Triumph II) was utilised for attenuation correction. For the dynamic acquisition of FET (n = 5), injections were performed via a venous catheter. There, the transmission scan was performed first, followed by a synchronised tracer injection with emission scan start.

For the neuroblastoma CAM studies, dynamic PET scans were performed using the Siemens InVeon scanner with 30 minutes emission scans, followed by 10 minutes transmission scans. All radiotracers were injected using the stereomicroscope, thus, emission scans were started with a time delay of up to 10 minutes.

For image reconstruction, OSEM3D/MAP was applied resulting in an image voxel size of 0.7764 x 0.7764 x 0.7796 mm³ and a matrix size of 128 x 128 x 159 for InVeon measurements, and a voxel size of 0.25 x 0.25 x 0.597 mm³ and a matrix size of 240 x 240 x 192 for Triumph II scans. All images were corrected for scatter, decay, attenuation, and dead time.

After the scan, the chick embryos were checked for vital signs, for example by visual assessment of pulse with a high magnification stereomicroscope before tissue processing.

Image analysis was performed using summed images from 18 to 50 minutes post injection using the software PMOD (Version 4.205, PMOD Technologies Ltd.). Volumes of interest (VOIs) were manually outlined to respective tissues of interest, as heart, liver, kidney, brain, or CAM tumour.

3.3.4 Finalisation

For finalisation of chick embryo experiments, ethical standards consistent with the national and European animal welfare guidelines were strictly followed. Isoflurane vapour exposure was utilised as anaesthesia to minimise suffering before finalisation, as described in detail in chapter 3.3.3.1. The embryo was then promptly decapitated with sharp, sterilised scissors at the base of the skull.

3.3.5 Tissue Preparations and Sectioning

Following the decapitation after anaesthesia, the tissue of interest was extracted.

For intracerebral tumour studies, feathers and skin were removed on the upper side of the head. Beginning from the brain stem, the skull was cut upwards gently along the sagittal suture to not damage the brain. The two halves of the skull were peeled away to the sides, the brain was gently scooped out, weighted, and frozen in -50°C cold isopentane for thirty seconds. The brain was stored at -80°C if not utilised directly.

For CAM tumour studies, the derived tumours were found either protruding inside the silicone ring, or below the CAM surface in the silicone ring position. Depending on the implanted cell line, solid tumours of approximately 1 cm^3 or multiple smaller spheroids could be found. The tumour tissue was weighted and frozen in -50°C cold isopentane for thirty seconds. If directly utilised for *ex ovo* autoradiography, the tissue was directly sectioned, otherwise, it was stored at -80°C until further use.

The respective tissue was cut into 20 µm thick sections with a cryostat CM3050 S Leica (Leica Microsystems CMS GmbH, Germany). For intracerebral tumour studies, coronal sections of the brains were chosen. For CAM tumour experiments, the orientation of the solid tumours was not specified.

For sectioning, the respective tissue was fixed on an object holder with Tissue-Tek® O.C.T (Sakura Finetek, the Netherlands), and a single-use microtome blade (Leica DB80 LS, Leica Microsystems CMS GmbH, Germany) was utilised for cutting. With the help of an anti-roll plate, the cut section was pressed on -20°C cold silane coated objective slides. After slowly thawing on the edge of a heating plate, the dry slices were stores at -80 °C until further processing. For autoradiographic examination, every tenth dry section was utilised as described in the following chapter.

3.3.6 *Ex ovo* Autoradiography

For high resolution radiotracer evaluation, *ex ovo* autoradiography was utilised after finalisation of the chick embryo one hour after radiotracer injection and the tissue was prepared as described in the previous chapters. Every tenth slice was exposed to a [^{18}F] and [^{68}Ga] sensitive phosphor imaging plate (BAS TR2025 Fuji Imaging Plate, Raytest Isotopenmessgeräte GmbH), together with freshly prepared tracer standards of known activity. The standards were prepared with five chicken liver homogenates of 1g each, that were mixed with 1.5MBq, 0.8MBq, 0.4MBq, 0.2MBq, and 0.04MBq of radiotracer, respectively. After centrifugation for 20 minutes at 5000 g at 4°C, the standards were frozen in -50°C cold isopentane and cut in 20 µm thick sections. All sections were exposed to the imaging plate overnight, scanned (Fuji BAS Reader 5000, Raytest Isotopenmessgeräte GmbH), and read out in 25µm resolution. The quantitative evaluation of the derived digital autoradiogram was performed with the software AIDA Image Analyzer (AIDA Version 5.1 SP 2, Raytest Isotopenmessgeräte GmbH).

For quantification of tracer uptakes, the standards of known concentration were calculated to fit the respective injection time of the respective tissue. For a clear depiction of signal, the background signal was subtracted. The regions of interest (ROIs) were defined based on histological or immunohistofluorescence staining on adjacent slices, as described in detail in chapter 3.3. For the intracerebral glioma study, the adjacent slice was stained with DAPI for a depiction of tumour tissue in the brain. The mean tumour-to-brain ratio (TBR) was calculated by division of tracer uptake in tumour tissue by the uptake in the normal brain tissue in the contralateral hemisphere. For neuroblastoma CAM tissue, the adjacent slice was stained with a human nuclei marker to determine the location of human-derived tumour tissue within the CAM. The mean standardised uptake value (SUV_{mean}) was calculated by dividing the radioactivity in the respective tissue by the injected radioactivity per gram body weight. The whole egg (47-52 g) was chosen as the reference body weight.

3.3.7 Evans Blue Dye Evaluation

For the assessment of BBB integrity in intracerebral tumours, 20 µl of 2% Evans Blue in 0.9% NaCl were injected into a middle-sized CAM vein one hour before finalisation. After tissue preparation, a cryoslice containing the region of interest was warmed up to room temperature, left to dry, and examined with a TXR filter (610 nm) using a microscope (Leica LMD 6000, Leica Microsystems CMS GmbH, Germany) at 5x magnification. For better visualisation, the derived image was colour-inverted to blue scale and qualitatively examined.

3.4 Histology and Immunofluorescence

For all stainings, Tris-buffered saline (TBS) or Phosphate-buffered saline (PBS) were utilised as wash buffer. 1xTBS was prepared with final concentrations of 38.5 mM Tris-HCl, 11.5 mM Tris-Base, and 500 mM NaCl, pH 7.45. 1xPBS was prepared with final

concentrations of 137 mM NaCl, 2.7 mM KCl, 10 mM Na_2HPO_4, and 1.8 mM KH_2PO_4, pH 7.45.

3.4.1 Nuclei Staining

In order to visualise all nuclei for localisation of specific regions on the slice, the nuclei dye 4',6-Diamidin-2-phenylindol (DAPI) was utilised. For intracerebral brain tumours, every tenth slice was stained to localise the tumour cells in the brain. For this, the -80°C cold sections were thawed to room temperature for ten minutes. Then, the mounting medium Fluoromount-G™ containing DAPI (Invitrogen, USA) was utilised and slices were covered with coverslips. Overall slice images were acquired with a UV filter using a microscope (Lumar.V12, Zeiss, Germany).

3.4.2 Antibody Staining with Human Nuclei Antibody

For a proof of tumour tissue, the human origin of all cell lines in this xenograft model was proven using an immunostaining with a mouse monoclonal human nuclei antibody (MAB1281, Merck Millipore, Germany).

The sections from -80°C storage were thawed to room temperature for ten minutes. Then, fixation was performed with -20°C cold methanol for 10 minutes under a fume hood. After three washing steps for 5 minutes each in TBS with 1% Triton X-100 (TBS-T), the primary antibody was added in a 1:250 dilution to the washing solution over night at 4°C. On the next day, the unbound antibody was washed off two times for 5 minutes each in TBS-T, before adding secondary antibody goat anti mouse Alexa 488 (A11001, Invitrogen, USA) or 568 (A11004, Invitrogen, USA) in a dilution of 1:500 in TBS-T. The secondary antibody incubation was performed for 2.5 hours at room temperature in a humid dark chamber. Afterwards, the unbound secondary antibody was washed off two times for 5 minutes in TBS. All nuclei were then stained with DAPI, in a concentration of 0.5 µg/ml in TBS, for 5 minutes. Another washing step for 5 minutes in TBS was used to get rid of unbound DAPI solution, before the mounting medium Fluoromount™ Aqueous Mounting Medium (Sigma-Aldrich, USA) and a coverslip were utilised.

3.4.3 Antibody Staining with Proliferation Marker Ki-67

For an indication of proliferative cells, the antibody rabbit anti Ki-67 (ab16667, Abcam, UK) was utilised, mainly in a double staining with anti human nuclei, as described in chapter 3.4.2. For this, the same protocol as before was used, with added primary antibody in a 1:250 dilution in TBS-T, as well as added secondary antibody donkey anti rabbit 488 (A21206, life technologies, USA) in a dilution of 1:500 to the secondary antibody solution. Two different coloured secondary antibodies were utilised for a clear identification of signals.

3.4.4 Antibody Staining for Glial Fibrillary Acidic Proteins

The antibody staining for glial fibrillary acidic proteins (GFAP) was performed with a rabbit polyclonal antibody (Z0334, DAKO, USA). For this, slices were thawed for ten minutes at room temperature, followed by the fixation step for 10 minutes in 4%

paraformaldehyde in TBS. After three washing steps in 1% TBS-T for 5 minutes each, the primary antibody was diluted 1:500 in 1% TBS-T over night in a dark, wet chamber in the fridge. On the following day, the antibody was washed off with three washing steps in TBS for 5 minutes each. Donkey anti rabbit secondary antibody (A21206, life technologies, USA) was used 1:500 in 1% TBS-T for 2.5 hours at room temperature. The secondary antibody was washed off with three washing steps for 5 minutes in TBS, incubated with 1:10000 DAPI in TBS for 5 minutes, and subsequently washed off again for 5 minutes in TBS. The finished staining was mounted with Fluoromount™ Aqueous Mounting Medium and covered with a coverslip.

3.4.5 Antibody Staining for SOX2

The antibody staining for sex determining region Y box2 (SOX2) as functional neural stemness marker was performed with a goat polyclonal antibody (ab239218, Abcam, UK). Slices were thawed to room temperature for ten minutes, followed by a 10-minute fixation step in 4% paraformaldehyde in PBS. After two washing steps with 1%PBS-T, the primary antibody was diluted 1:100 in 1% PBS-T and incubated overnight in a dark humid chamber at 4°C. On the following day, the antibody was washed off three times with 1%PBS-T for 5 minutes each. Donkey anti goat antibody 488 (A11055, Invitrogen, USA) was diluted 1:1000 in 1% PBS-T and incubated for 2.5 hours at room temperature. After washing it off two times for 5 minutes in PBS, the slices were incubated with 1:10000 DAPI in PBS for 5 minutes, and subsequently washed off again two times for 5 minutes in PBS. The finished staining was covered with Fluoromount™ Aqueous Mounting medium and a coverslip.

3.4.6 Antibody Staining for Nestin

An antibody staining for Nestin was utilised as marker of neural stem cells with the mouse monoclonal anti Nestin antibody (ab18102, abcam, UK). After thawing the slices to room temperature, a fixation step with 4% paraformaldehyde in PBS was performed for 10 minutes. After washing off three times for 5 minutes in 0.3% PBS-T, the primary antibody was diluted 1:300 in 0.3% PBS-T and incubated overnight in a dark humid chamber at 4°C. On the next day, three washing steps for 5 minutes each were performed with 0.3% PBS-T. For the secondary antibody incubation, the secondary antibody goat anti mouse Alexa 488 (A11001, Invitrogen, USA) was utilised in a dilution of 1:1000 for 2.5 hours at room temperature. After two washing steps with PBS for 5 minutes each, the slices were incubated with 1:10000 DAPI in PBS for 5 minutes, and subsequently washed off again two times for 5 minutes in PBS. The finished staining was covered with Fluoromount™ Aqueous Mounting medium and a coverslip.

3.5 Data Evaluation and Statistics

Quantification of proliferative cells was performed on overview images of brain slices stained with Ki-67 using the software ImageJ (National Institute of Health, Bethesda, MD, United States).

All statistical calculations were performed with GraphPad Prism 10.0.2 (GraphPad Software, Inc., La Jolla, CA, United States). Descriptive statistics are provided as mean and standard deviation. For methodology comparison, a paired t-test and Pearson correlation (r) were chosen. Survival Analysis was performed with a Gehan-Breslow-Wilcoxon test. The Gaussian distribution of all data was validated using the normality plot in GraphPad Prism. Normally distributed data were analysed in one-way analysis of variance (ANOVA). Šídák's pairwise multiple comparisons were utilised for more detailed analysis. A p-value of less than 0.05 was considered to indicate statistically significant differences in all tests.

4 Results

4.1 Methodological Adaptations for Chick Embryo Experiments

All procedures and interventions on chick embryos were conducted in full compliance with German national and EU regulatory guidelines. Recent advances in the understanding of chick embryo nociception have emphasised the ethical responsibility in chick embryo experiments for animal welfare considerations. As a result, experimental settings have been refined to minimise potential pain, harm, and distress, as described in detail in Chapter 4.1.1. Besides, experiments utilising chick embryos often face challenges due to their high sensitivity interfering with the chick embryonic development. Therefore, efforts have been directed towards improving experimental conditions to enhance chick embryo viability as described in Chapter 4.1.2.

4.1.1 Adaptations for Ethical Considerations for Chick Embryo Studies

Intracerebral tumour growth in the chick embryo might pose a risk of increased physiological burden on the animal if the tumour grows too excessively. For intracerebral rat studies in-house, humane endpoints were previously considered when the tumour reached 4-7% of the brain volume, depending on the occurrence of additional behavioural abnormalities or the specific location of the growing tumour [103]. Thus, objective monitoring was implemented via non-invasive MR observation of tumour volume in the brain whenever research on a new brain tumour cell line was initiated. With this, chick embryos with intracerebrally implanted new cell lines were longitudinally measured and checked for too large tumours based on our experience of tumour burden in rodents. Once established, the cell number implanted was adjusted in a way to not exceed humane endpoint sizes known from rodent experimentation of comparable-sized brains for the whole duration of the chick embryo experiment. Embryos with implanted brain tumours that stopped their development naturally were sorted out daily, and their brains were extracted and checked for excessive tumour growth for further validation and refinement of the methodology.

For a functional MR monitoring of tumour growth, a standard birdcage coil was modified and constructed by Dr. Chang-Hoon Choi [146] to improve Signal-to-Noise Ratio (SNR), as visualised in Figure 10. With multiple measuring steps, starting with unfertilised supermarket eggs and then embryonal chicks at various developmental stages, a modified birdcage coil with increased sensitivity and coverage in relevant regions of the curved egg was established. A good SNR is of special interest in regions of the egg where the head normally turns to, which is physiologically the pointed or blunt end with increasing growth of the chick inside the egg (Figure 10 regions a and d). As the risk of too excessive tumour growth increases with longer duration, regions near the end of the egg are more relevant for chick embryo brain tumour research in this aspect. With the modified birdcage coil, more uniform B_1^+ fields in those regions could be achieved with an improvement of SNR of 36% in the pointed end and 29% improvement in the blunt end, enhancing the quality of MR measurements significantly. However, in regions near the centre, the SNR decreased by approximately 6% in the

modified coil compared to the standard birdcage coil (Figure 10, regions b and c) [146]. Thus, the monitoring of tumour growth was performed with the modified coil.

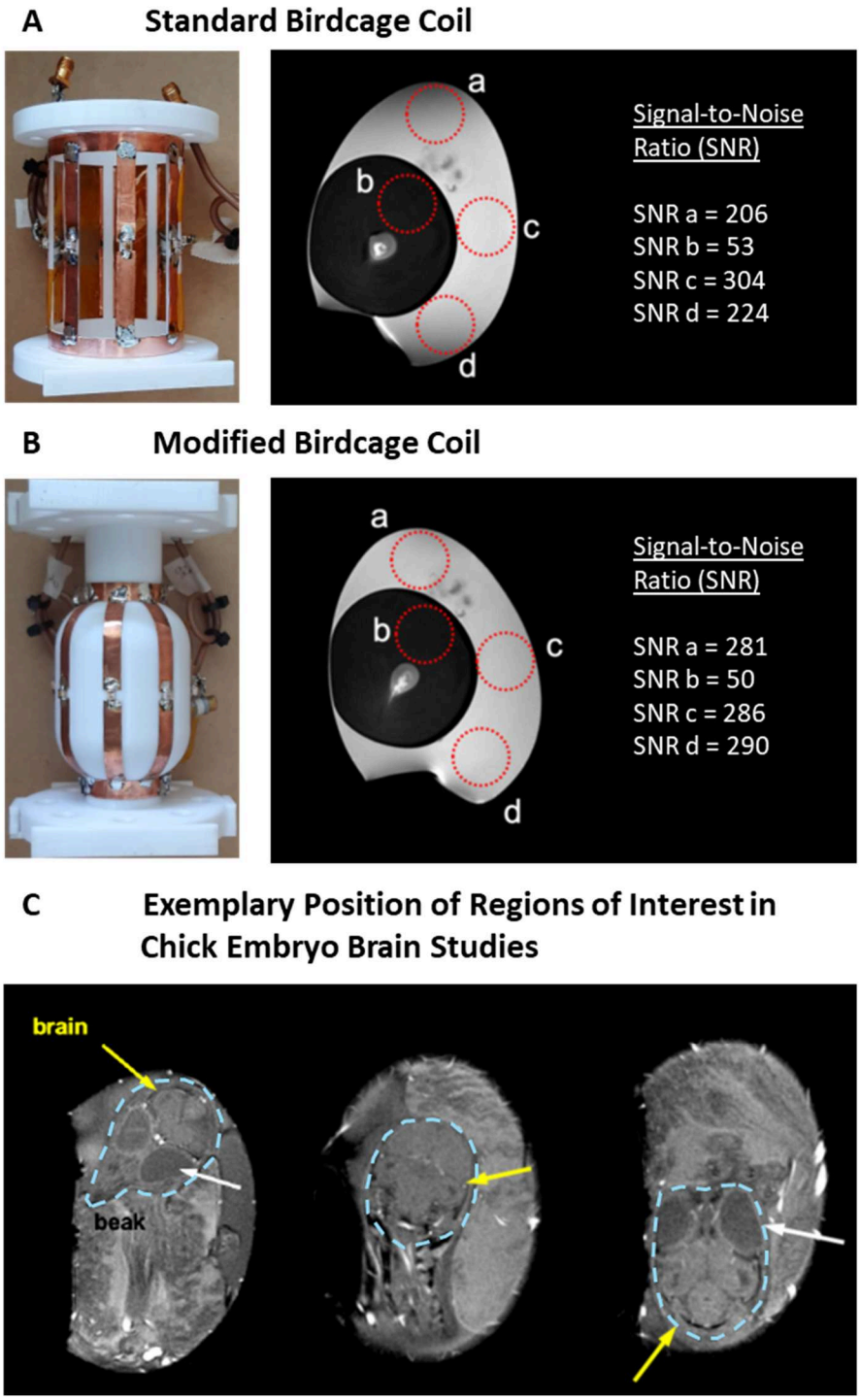

Figure 10: Performance comparison of standard birdcage coil and modified birdcage coil based on signal-to-noise ratios (SNR) in various regions of interest (ROIs) in supermarket eggs, with validation in embryonal chicks. A: Standard birdcage coil with circular ROIs at the pointed and blunt end of the unfertilised egg, as well as two regions in the centre. B: Modified birdcage coil designed and constructed by Choi et al. [146] with curved feature for egg measurements showed improved SNR at the two ends of the unfertilised egg with lower SNR in the centre. C: Validation with three exemplary chick embryos showing the position of the brain (yellow arrows), eyes (white arrows) and the head position (dotted blue line) inside the egg. As development progresses, the head appears to orient itself physiologically towards one end of the egg. This is why the modified birdcage coil offers improved MR image quality in this configuration. Image modified from [146].

If excessive tumour growth in the chick embryo brain can be ruled out, the highest burden in brain tumour research arises from the tumour inoculation itself. This intervention is timed at EDD 5, where the chick embryo is not yet capable of nociception [138–140].

As the CAM is not innervated, effects of CAM tumour growth only needed to be considered for too aggressive growth with blood depletion on the embryo. For this, the rate of developmental failures in the later EDDs was considered as an indicator of tumour burden: Control embryos that were fenestrated on EDD 5 but did not receive any intervention showed a viability of 61% (n = 49) on EDD 14-20. For neuroblastoma CAM tumours, the viability in the same developmental stages was 66% for the LAN-1 (n = 38), and 92% for the SH-SY5Y (n = 36) cell line.

4.1.2 Adaptations of Experimental Conditions for increased Chick Embryo Viability

High and variable developmental failure rates represented a major challenge. Adjustments to the experimental conditions were tested to improve chick embryo viability, as explained in chapter 3.3, resulting in a reduction of developmental failure rates by 12%; however, other unknown factors for this developmental failure decrease cannot be excluded.

During the windowing procedure, the air bubble at the blunt end was deliberately used as a lever to separate the embryo from the inner eggshell membrane. Depending on the operator, and unknown factors as the batch storage duration before arrival, this procedure varied in difficulty between cohorts, with some relocations causing the embryo to twist into an s-shaped orientation, in below 5% of cases. S-shaped embryos resulted in developmental failures in 100% of observed cases (n = 11) within 10 developmental days. Thus, a method for repositioning of s-shaped embryos was tested, as visualised in Figure 11. S-shaped embryos were observed directly after windowing on EDD 5 through the s-shape of the spine, where the allantois (Figure 11 B, asterisk) and the head are oriented into different directions. For the repositioning, a hole was punctured into the chorion next to the spine with a sharp glass capillary and opened along the side of the embryo without damaging the amnion (Figure 11 B, blue line). Then, a micro-spatula was inserted, and the embryo’s head and upper body were carefully rotated back into the orientation of the allantois. The chorion healed within 48 hours. Higher developmental failures were observed directly after the intervention on EDD 5. Only one s-shaped embryo showed normal development after repositioning until final experimentation on EDD 19 (1/7 successful, n = 7). Kaplan-Meier survival analysis showed no significant difference between s-shaped as well as repositioned embryos (Gehan-Breslow Wilcoxon test, p = 0.6414) and a median of 8 survival days for both.

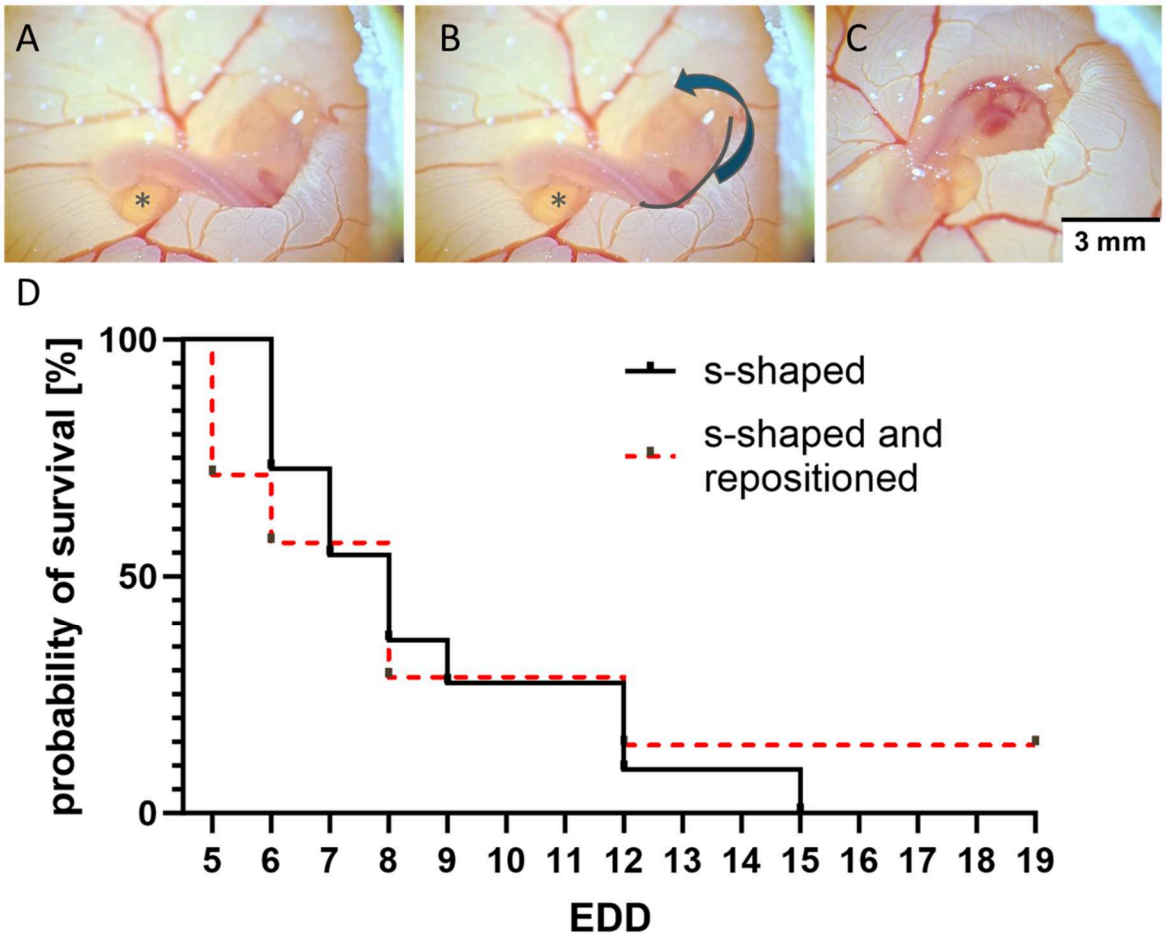

Figure 11: Technique of repositioning of an s-shaped embryo on EDD5 and its influence on survival. A: An s-shaped embryo on EDD 5, with a prominent curvature in the spine. The head and the allantois (asterisk) are oriented into opposite directions. B: With a glass capillary, a hole is punctured into the chorion next to the spine without damaging the amnion, and the chorion is opened along the upper side of the embryo (blue line). The allantois (asterisk) guides the direction of repositioning. A micro-spatula is inserted into the opening of the chorion, and the head and upper body of the embryo are rotated back into the direction of the allantois. C: Visualisation of a repositioned embryo. D: Kaplan-Meier Survival Analysis of s-shaped embryos without intervention (n = 11) in black and with intervention (n = 7) in dotted red. No statistically significant difference could be observed (Gehan-Breslow-Wilcoxon test, p = 0.6414).

4.2 Evaluation of the Intracerebral Glioma Chick Embryo Tumour Model

Parts of this chapter have previously been published in Krause *et al*. 2025 [149].

In the following chapter, the validation of tumorigenicity, histopathology, as well as key aspects of the tumour microenvironment will be described. Also, the BBB of chick embryos will be analysed. Afterwards, the feasibility of radiotracer evaluation together with the translational relevance will be evaluated.

4.2.1 Tumorigenic Proliferation and Astrocyte Activation of U-87 MG and U-87 IDH1^{R132H} cells in the Intracerebral Chick Embryo Model

Intracerebral tumours were successfully generated in all viable chick embryos. However, 52% of chick embryos did not survive the implantation procedure until final experiments on EDD 18-20 (n_{total} = 85), with most developmental failures occurring within 48 hours post-surgery. In the control group, that were only fenestrated without an intervention until EDD 10, the mortality rate was 13% ($n_{control}$ = 226). The implanted tumour cells could be reliably found within the ventricles of one or both optic tecti, forming solid tumours with infiltrative growth into the brain tissue, as representatively shown in Figure 12 for U-87 IDH1^{R132H}, and in Figure 13 for U-87 MG. It should be noted that while the presence of the injected cells of human origin could be verified via an immunofluorescence staining with a human nuclei antibody (Figure 12 D and Figure 13 F), tracing each individual cell's fate was beyond the scope of analysis. In both implanted cell lines, strong GFAP-positive cells could be found in the vicinity of the tumour, revealing astrocyte activation (Figure 12 E and Figure 13 F).

An interesting example of U-87 IDH1^{R132H} is shown in Figure 12 D and F-I, where a strong infiltrative growth pattern into stratum griseum was observed in the left ventricle, whereas a solid and clear delineated tumour border was formed in the right ventricle. Both tumours showed high proliferative indices based on the proliferation marker Ki-67, with significant differences in the proliferation densities in the infiltration zones. The left tumour had 37% proliferative cells in this region, whereas the right tumour exhibited 62% Ki-67 positive cells. Additionally, in the centre of the right tumour, a region without Ki-67 positive cells could be observed (Figure 12 G).

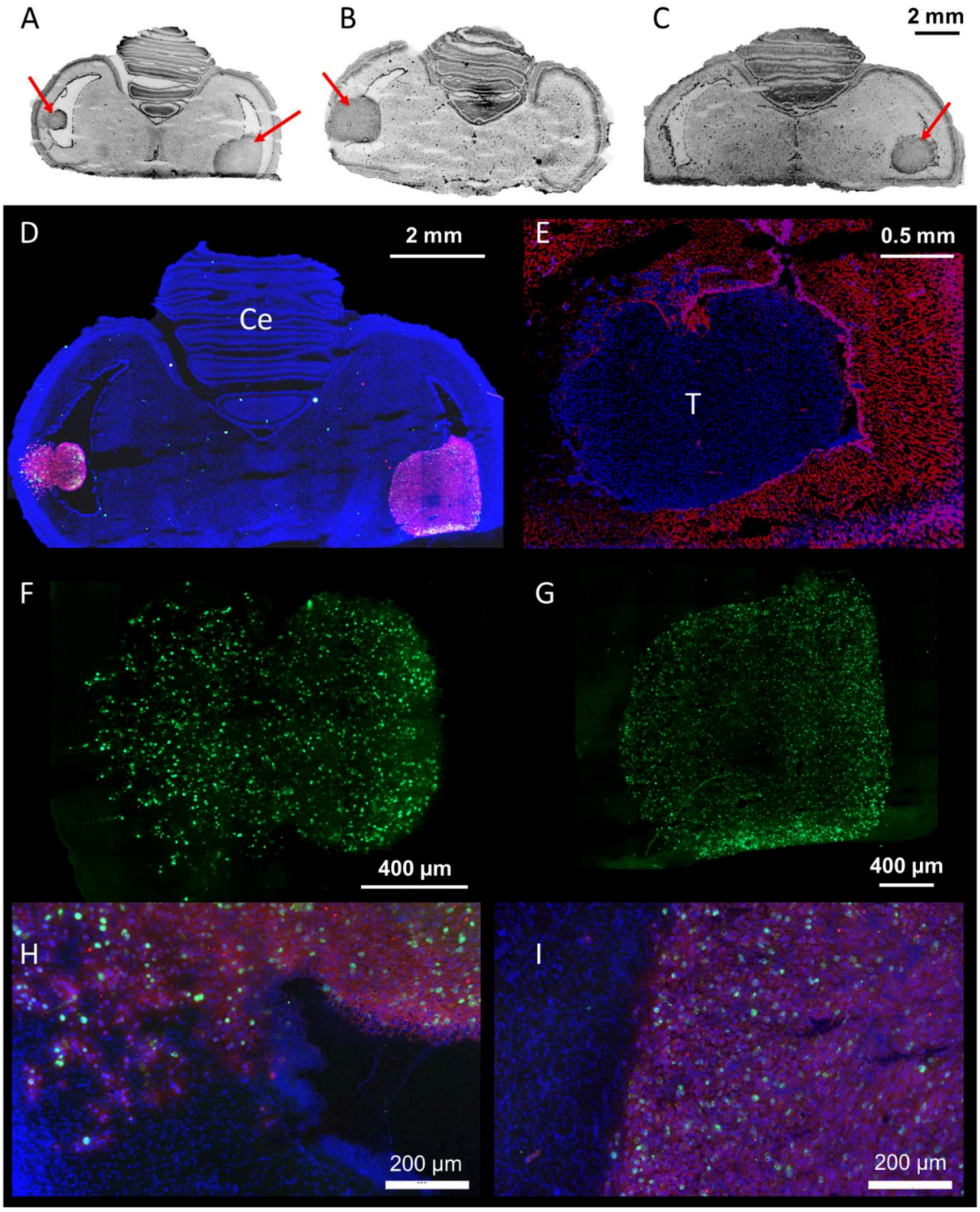

Figure 12: Representative 20 µm slices of intracerebral U-87 IDH1^{R132H} tumours in the chick embryo model with representative tumour proliferations and activated astrocytes. A-C: DAPI stainings in three chick embryos shows densely packed tumour cells (red arrows), reliably found in the ventricles of the chick tectum opticum with growth into the surrounding brain tissue. D: Exemplary staining with a human nuclei antibody as proof for cells of human origin (red), where proliferating cells are shown with proliferation marker Ki-67 (green). In blue, all cell nuclei are marked. This staining was performed on a consecutive slide of A. The abbreviation 'ce' indicates the position of the chick cerebellum. E: Representative astrocyte staining using an anti-GFAP antibody (red) reveals astrocyte activation in the tumour (marked with T) vicinity of a consecutive slide of C. F-G: Extract of Ki-67 positive cells of slice D for the left tumour (F) and the right tumour (G) in green. H-I: Detailed images of the border regions of both tumours of image D in higher magnification, revealing the infiltrative growth pattern into stratum griseum (H) and the solid and clear delineation of the right tumour (I). Image partly adapted from [149].

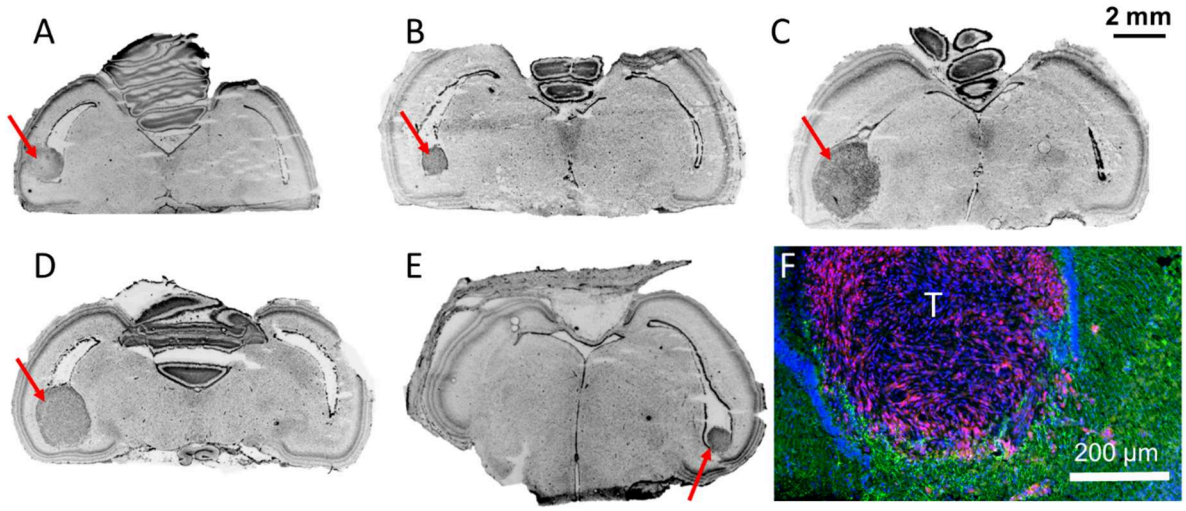

Figure 13: Representative 20 µm slices of intracerebral U-87 MG tumours in the chick embryo model. A-E: Densely packed tumour cells (red arrows) could be reliably found in the ventricles of the chick tectum opticum with DAPI staining. Mostly, solid tumours with clear borders were formed (B, D, E), with some infiltrative growth into the surrounding brain (A, C). F: Representative astrocyte staining shows astrocyte activation with an anti-GFAP antibody (green) in the vicinity of a human-origin tumour (red, tumor marked with T). For this image, a consecutive slice of the tumour in E was chosen.

4.2.2 Evaluation of Blood-Brain Barrier Integrity in the Intracerebral Glioma Chick Embryo Model

BBB integrity was assessed either *in ovo* by MRI following administration of a paramagnetic contrast agent (Figure 14), or *ex ovo* using Evans blue dye extravasation (Figure 15).

MR experiments were also utilised the day before PET for the identification of suitable-sized brain tumours using T1- and T2-weighted images (Figure 14 A, B). The injection of contrast agent (n = 1) significantly improved the delineation of tumour rim region in the respective chick embryo with disrupted BBB (Figure 14 C). Magnified images focused on the brain are shown in Figure 14 E-G.

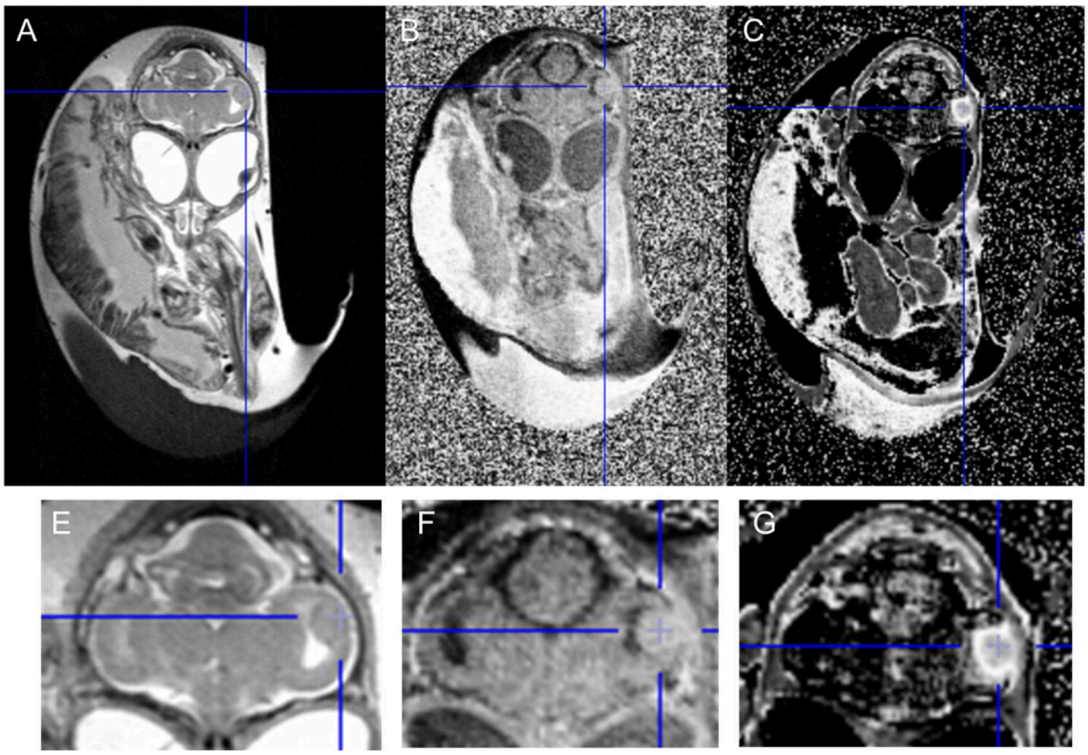

Figure 14: MR images of a chick embryo with intracerebral U-87 MG tumour on EDD 19. T2- (A) and T1-weighted MRI (B) as well as T1-weighted MRI after contrast agent injection (C). The tumour is depicted with the crosshair in the ventricle of the optic tectum. The contrast-enhanced, T1-weighted MRI (C) shows a BBB disruption at the rim of the tumour. In E-G, magnified images of A-C focused on the brain are shown. Image modified from [149].

The *ex ovo* BBB evaluation was performed in five intracerebral U-87 MG chick embryos with Evans blue dye (n = 5), as visualised in Figure 15. A stronger extravasation of Evans blue dye and thus BBB impairment could be seen especially at the rim region of three chick embryos (Figure 15 B, D, and H). In one chick embryo, the BBB was only disrupted slightly at tumour rim region (Figure 15 J), whereas in another chick embryo, no Evans blue extravasation could be seen, indicating an intact BBB (20%, 1 out of 5) (Figure 15 F).

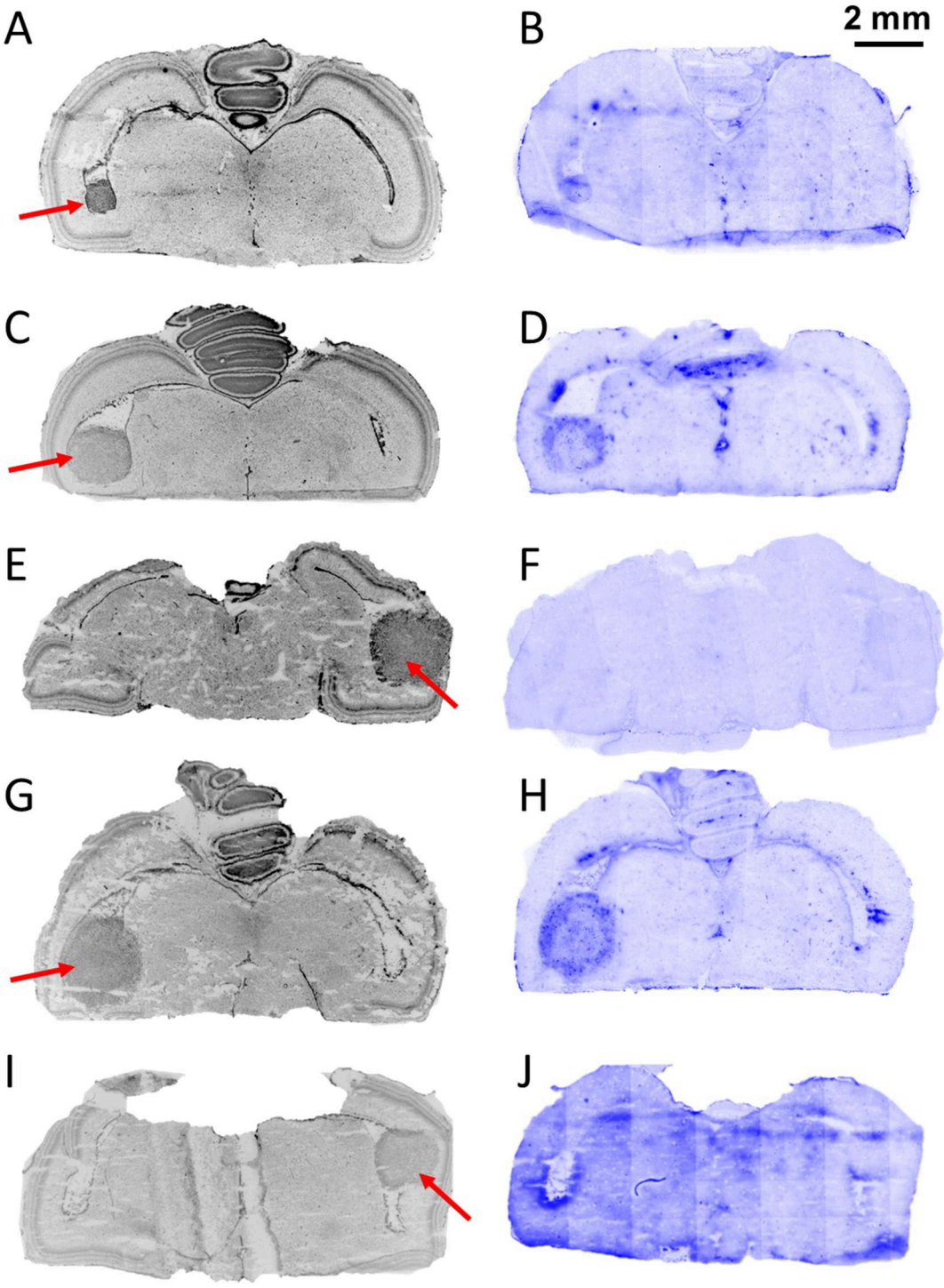

Figure 15: Evaluation of BBB integrity on chick embryos with intracerebral U-87 MG tumours (n = 5). Each row represents one chick embryo with nuclei staining revealing the tumour regions through densely packed nuclei (left column, tumours marked with red arrows) and the consecutive slice showing the Evans blue dye extravasation (right column). Evans blue dye extravasation can be depicted in the tumour rim region in B, D and H. In J, only a slight extravasation at tumour rim region can be seen, whereas in F, no Evans blue extravasation could be observed in the tumour region, indicating an intact BBB. In all cases, Evans blue dye was injected correctly in a CAM vessel. Image adapted from [149].

4.2.3 Feasibility of Radiotracer Evaluation in the Chick Embryo Model

Due to differences in terminology and conceptual usage across research fields, a clear definition of the term ‘tracer uptake’ is required prior to data analysis. In the context of radiotracer evaluation in oncology, the term ‘tracer uptake’ does not imply continuous

tracer influx but denotes the measurable tracer concentration within a tissue at a given time point. This concentration results from dynamic processes including initial accumulation and subsequent wash-out, and the term is used here in accordance with its widespread application in oncological imaging and SUV-based analyses.

In a first step, the feasibility of radiotracer evaluation in the chick embryo model was tested using the radiolabelled amino acid FET. The feasibility of µPET evaluation in naïve chick embryos is representatively shown in Figure 16 A, where high uptakes in liver, heart, and kidneys with low brain uptake could be qualitatively observed. Also, dynamic FET imaging was performed in naïve chick embryos (n = 5) for the assessment of time-activity curves of FET accumulation in the organs heart, liver, kidney, and brain (Figure 16 B). Within the first minutes after injection, high mean uptake values could be found in heart, liver, and kidney. The plateau of nearly constant organ uptakes was reached in about 20 minutes after intravenous injection for all investigated organs. Mean SUV were calculated with the weight of the whole egg as reference body weight. In average, from the chick tissues of interest, FET showed the highest accumulation within the heart (SUV_{heart} = 3.70 ± 0.35), closely followed by high uptake in the liver (SUV_{liver} = 3.51 ± 0.41 and kidneys (SUV_{kidney} = 3.26 ± 0.43), indicating FET clearance through hepatic/pancreatic and urinary pathways. The brain SUV was moderate with an average of 1.09 ± 0.09. In the time frame of 10 minutes to the end of measurements, the SUV rates declined, with -0.4433 SUV/h for the heart, -0.436 SUV/h for the liver, and -0.3032 SUV/h for the kidney. The SUV rate of the brain was slightly increasing with a rate of 0.0376 SUV/h.

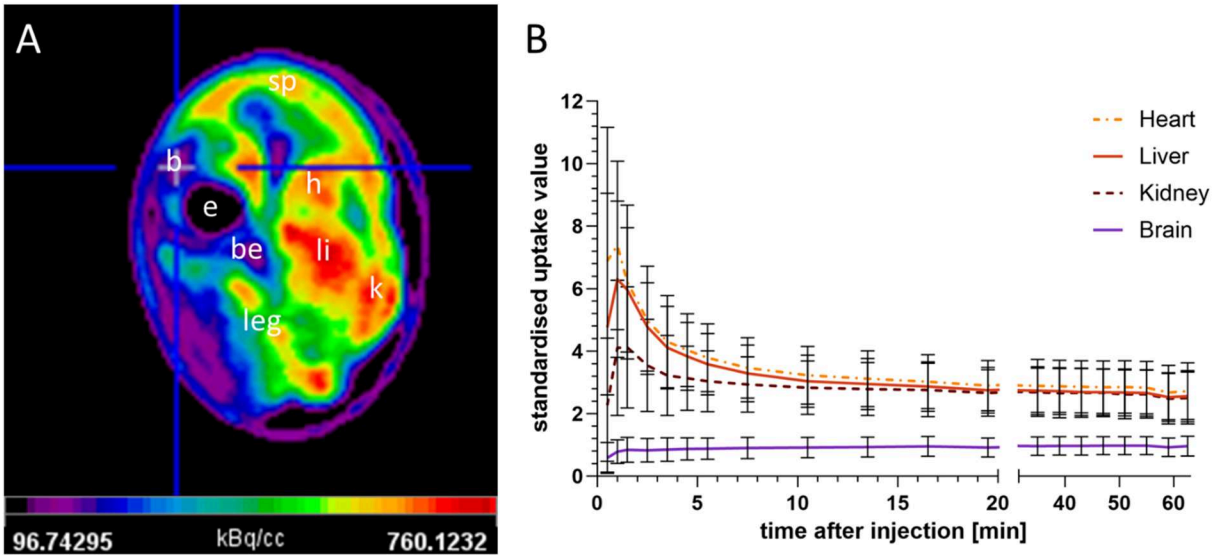

Figure 16: Representative image of a naïve chick embryo FET µPET and the time-activity curves of FET uptake in relevant chick organs. A: Representative summed image of a FET µPET of a chick embryo on EDD 19, averaged from 18 to 50 minutes post injection. The crosshair points at the brain. B: Averaged time-activity curves of FET uptake in chick embryos (n = 5) in the heart, liver, kidney, and brain. High mean uptake values in the heart, liver and kidney could be found in the first minutes of injection. All organ uptakes reached equilibrium after 20 minutes. Abbreviations: b, brain; sp, spine; e, eye; be, beak; h, heart; li, liver, k, kidney. Image adapted from [149].

For radiotracer analysis within the tumour bearing brain, in addition to FET PET scans, *ex ovo* autoradiography analysis of FET was performed as an established preclinical diagnostic tool for brain tumours, as the relatively small size of the brain resulted in significant partial volume effects in the tumour VOIs. Thus, the SUV of the whole brain was used to compare both methods of acquisition. A pairing of derived brain SUV of dynamic *in ovo* PET measurement and of *ex ovo* autoradiography was analysed for individual subjects (n = 4), showing only minimal deviation with significant correlation of pairs (paired t-test: p = 0.8840; effectiveness of pairing: correlation coefficient: r = 0.9811 with p = 0.0094), resulting in a high degree of congruency between the two chosen methods (Figure 17).

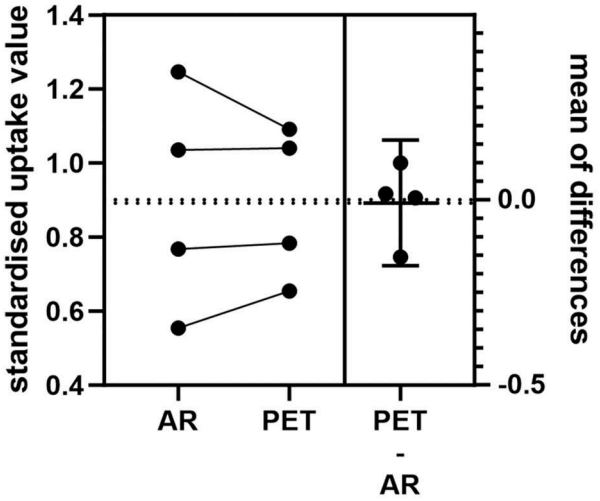

Figure 17: Correlation efficiency of PET and ex ovo autoradiography (AR) derived standardised uptake values of naïve chick embryo brains (n = 4), showing significantly effective pairing (paired two-tailed t-test, p = 0.8840; correlation coefficient r = 0.9811 with p = 0.0094). Image adapted from [149].

In the following, the intracerebral glioma chick embryo model was evaluated based on the radiotracer uptake in the brain and the intracerebral tumour through the parameter TBR_{mean} of the radiotracers FET (n = 5), FDOPA (n = 3), and FAPI (n = 4). Due to the small size of the tumour inside the brain, *ex ovo* autoradiography was performed. The delineation of the tumour was based on a nucleus staining of the consecutive slide of the brain (Figure 18, left column). The tracer uptake on the corresponding slide is visualised representatively for each tracer in Figure 18 (right column). With all three radiotracers, the tumour could be easily identified by high tracer uptake whereas the surrounding brain showed lower uptake.

For FET, with the weight of the whole egg as body weight reference, the average SUV of the chick embryo optic tecti, as main brain region of interest was 0.80 ± 0.31 in *ex ovo* autoradiography, whereas the SUV of the tumour was 1.25 ± 0.35. The TBR of U-87 MG tumours in the developing chick brain was 1.69 ± 0.54 as TBR_{mean}, and 1.92 ± 0.5 as TBR_{max}.

In the example of FDOPA, a special case can be observed, where two tumours with visibly different FDOPA uptakes have formed: the left tumour shows isometabolism

(TBR_{mean} = 1.1), while the right-sided tumour showed high tracer uptake (TBR_{mean} = 3.8). A chick-genetic origin of the tumours could be excluded, as both tumours were of human origin (Figure 12 D).

For FAPI, the TBR_{mean} was proficient with 19.13 ± 0.64.

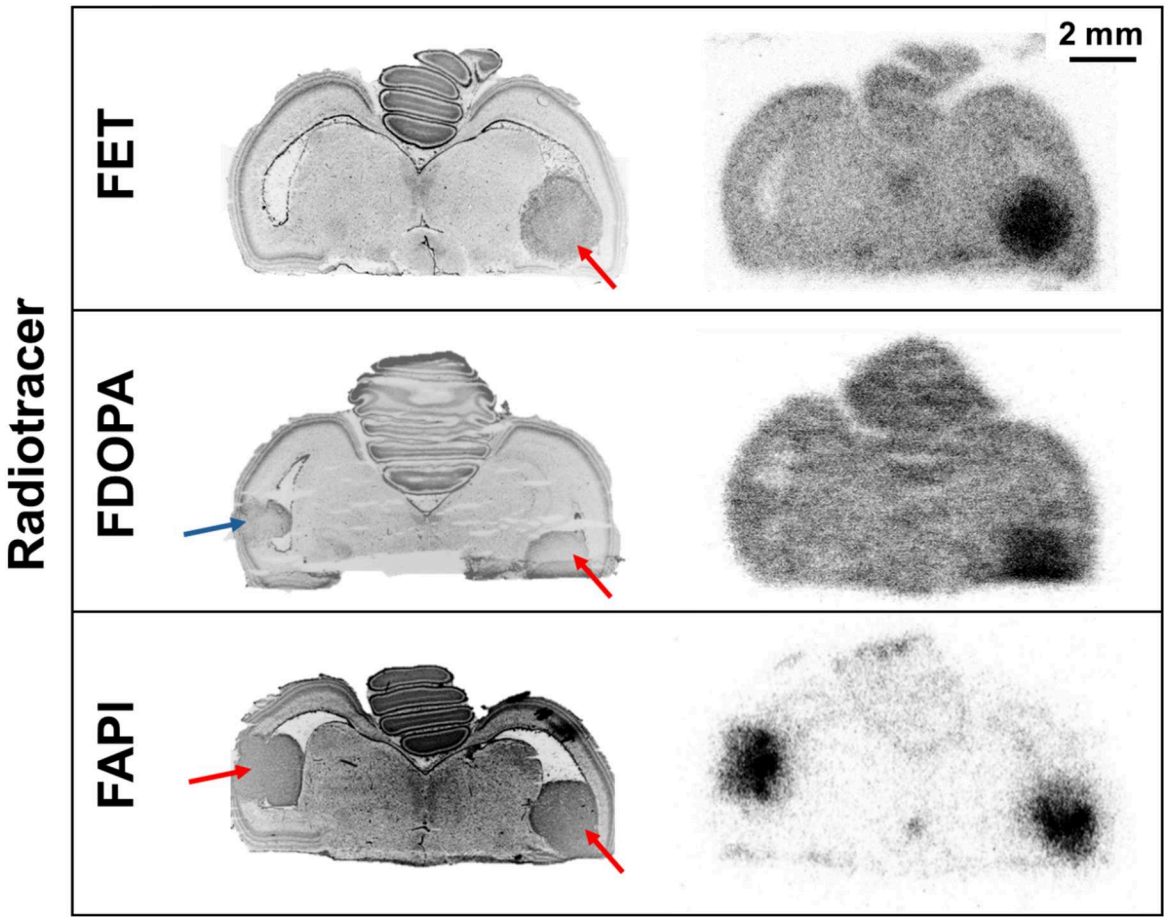

Figure 18: Histological stainings of intracerebral tumours (left, tumours marked with arrows) and the representative ex ovo autoradiographies (right) for the radiotracers FET, FDOPA, and FAPI in the intracerebral glioma chick embryo model. High tumour uptakes of the respective radiotracer can be seen, whereas the brain shows lower uptake. In the example of FDOPA, an increased uptake tracer can be seen in the right tumour, whereas the left tumour (blue arrow) appears isometabolic. Image adapted from [149].

4.3 Neuroblastoma Tumours on the Chorioallantoic Membrane

In the following chapter, the neuroblastoma CAM chick embryo model will be characterised. Then, radiotracer uptakes are evaluated based on µPET in naïve chick embryos as well as in the neuroblastoma CAM model. As a next step, a potential correlation of PET and AR derived uptake values for CAM tumours is assessed. Lastly, *ex ovo* autoradiographic tracer uptakes are inspected, together with a comparison to known patient tracer uptakes for an evaluation of translational relevance.

4.3.1 Characterisation of Neuroblastoma CAM Tumours

Inoculation of the neuroblastoma cell lines SH-SY5Y and LAN-1 on the CAM resulted in mean tumour weights of 125.7 mg for SH-SY5Y (n = 25), and 50.2 mg for LAN-1 (n = 15) for the test cohort on EDD 19 (Figure 19 A). Visible differences were observed during tumour growth on the CAM, with regular ruptures of CAM vessels observed in SH-SY5Y tumours, leading to extra-vasal blood deposits (Figure 19 B). However, these haemorrhages had no effect on the viability of the chick embryos or on the injection of radiotracers. The extracted SH-SY5Y CAM tumours appeared as dark red with volumes of up to 500 mm^3, indicating high blood content in those tumours with tumour induced angiogenesis. In contrast to this, LAN-1 CAM tumours appeared smaller in size, with volumes of approximately 315 mm^3 in the establishment cohort. The formed LAN-1 CAM tumours showed flat expansion rather than three-dimensional growth (Figure 19 C). For both cell lines, immunostainings with a human nuclei marker were used to differentiate between chick embryo CAM tissue and the inoculated cell lines of human origin, showing infiltrative tumour growth on the CAM with multiple small tumour cell clusters invading CAM tissue, rather than a single well-circumscribed and solid mass (Figure 19 D and E). Preliminary results showed some preservation of stemness in both cell lines, based on immunofluorescence analysis against the stem cell markers SOX2 and Nestin (data not shown).

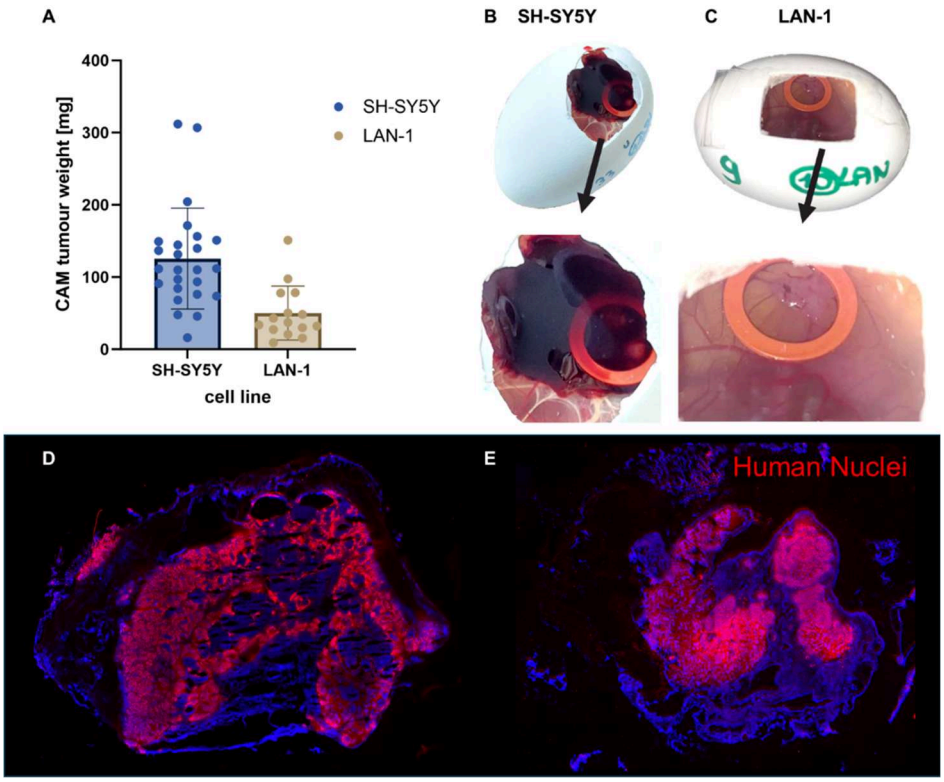

Figure 19: Characterisation of SH-SY5Y and LAN-1 neuroblastoma cells on the CAM of chick embryos. A: Mean tumour weights of 125.7 mg for SH-SY5Y (n = 25), and 50.2 mg for LAN-1 (n = 15) could be achieved after growth until EDD 19. B: Macroscopically visible CAM vessel ruptures with extra-vasal blood deposits in the surrounding of the growing SH-SY5Y CAM tumour were observed regularly. C: LAN-1 CAM tumours showed a rather flat tumour growth on the CAM. D-E: Representative overview immunostainings with human nuclei marker in red and all nuclei in blue (DAPI) revealing the infiltrative growth pattern with multiple cell clusters of SH-SY5Y cells (D) and LAN-1 cells (E) into the chick embryo CAM tissue.

4.3.2 Refinements of CAM Radiotracer Experiments in Chick Embryos

Generally, the chick embryo methodology of radiotracer studies needs the introduction of more rigorous controls to ensure comparable and robust experiments. Firstly, refinement strategies for both µPET experiments as well as *ex ovo* AR are given. Afterwards, PET-specific pitfalls are refined in the following sub-chapter. Lastly, the refined methodology for CAM radiotracer experiments in chick embryos is described.

4.3.2.1 General refinements for both µPET and *ex ovo* autoradiographies

For both µPET measurements and *ex ovo* AR, the utilisation of chick embryos enforced a higher need of rigorous functional control of tracer injection quality to assess whether radiotracer uptakes of CAM tumours could be considered reliable. In contrast to animal models, where the tracer is injected directly into a vessel of the organism and occlusion of the tail vein can be applied to prevent reflux after injection, injections into the extra-embryonic CAM are prone to bolus pooling on the membrane surface. Tracer injections into CAM vessels are technically more challenging than tail vein injections in rodents, as the vessel cannot be stabilised and occlusion or pinching are more challenging. Consequently, the injection process was prone to errors as tracer backflow, bleedings

after cannula extraction, and paravenous injections. For a robust and comparable CAM radiotracer evaluation, a rigorous measure of what is considered ‘still reliable experiment’ or ‘excluded due to failed injection’ is currently missing and needs to be found. Consequently, in this thesis, efforts were made to establish rigorous functional controls of radiotracer injections.

In the following scheme (Figure 20), possible complications in radiotracer injections and their impact on CAM tumour tracer uptakes are shown. In a fully functional correct injection procedure, the injected radiotracer entered the bloodstream, distributed through the chick embryo and the vascularised CAM and therefore represented CAM tumour uptakes in a realistic intravenous application. If a tracer was injected in a high volume and the injection into a vessel failed, the tracer activity would be accumulating on or below the surface of the CAM, possibly coming into close contact to the CAM tumour. As the resorption of tracer from the CAM region took longer than the one-hour experimentation utilised in this study, the CAM tumour might take up the radiotracer through other processes as diffusion rather than mimicking the intravenous application route. On the other hand, if the injection failed while utilising a small-volume tracer in a vessel distinct from the CAM tumour, the CAM tumour might not get into contact to the tracer at all. Both those cases needed to be excluded from radiotracer uptake evaluation. In most cases, a partial correct injection could be found, where a part of the tracer had been correctly injected into the vessel, but a residue of tracer stayed paravenous in the injection region.

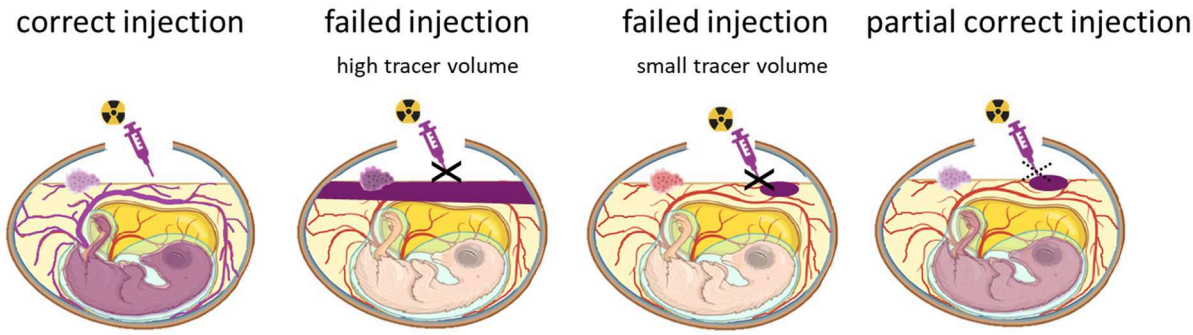

Figure 20: Schematic overview of possible radiotracer injections and their impact on CAM tumour radiotracer uptakes. Due to the higher difficulty of radiotracer injections into the CAM with sufficient pinching of the injection vessel to avoid paravenous radiotracer bolus pooling, different scenarios and their impact on radiotracer uptake of CAM tumours were considered. First, a correct intravenous CAM injection is shown, where the injected tracer entered the bloodstream, got distributed through the chick embryo and the vascularised CAM and therefore presented CAM tumour uptakes in a realistic intravenous application. Failed tracer injections can be subdivided into two groups, where the paravenous radiotracer came into contact with the CAM tumour, for example in the case of high tracer volume, or where no contact to the CAM tumour was possible. In the first scenario, the CAM tumour might take up the radiotracer through other processes as diffusion rather than mimicking the intravenous application route. In small volume failed tracer injections, where a locally distinct injection vessel was picked, the CAM tumour might not come into contact to the radiotracer at all. Both scenarios were considered failed injections and excluded from analysis. However, in the field of CAM radiotracer studies, studies oftentimes stated ‘partially missed’ injections, or heavy bleedings after injections, which led to the scenario of partially correct injections. In this case, some radiotracer entered the bloodstream and was distributed, but a residue was left on the injection side, either through partly paravenous injection or through leakage after injection due to the more difficult vessel pinching. This scenario needed to be examined more closely to ensure validity of achieved results, which has not been rigorously performed in literature.

For the determination of a new parameter as injection control, the kinetics of the utilised radiotracers in the chick embryo model had to be considered to track the physiological tracer accumulation after injection. Thus, the naïve chick embryo model was evaluated based on µPET using the radiotracers FET, FDOPA, and FDG. For a description of the results for FET in naïve chick embryos, please refer to Chapter 4.2.3 and Figure 16. Three naïve chick embryo measurements were performed each as control of physiological tracer uptake using FDOPA and FDG. The time-activity-curves (TACs) of FDOPA and FDG are shown in Figure 21, with the weight of the whole egg as reference body weight. For the FDOPA TAC (n = 3), a plateau of nearly constant uptake was reached after approximately 10 minutes for heart, liver and brain, with mean uptake values of 2.69 ± 0.36 for the heart, 3.02 ± 0.33 for the liver, and 1.12 ± 0.18 for the brain. The TAC of the kidneys showed a transient decrease within the first minutes after injection, with a visible increase afterwards. The kidneys showed the highest uptake of FDOPA with mean uptake values of 5.91 ± 1.13. The results of the liver and kidneys indicate FDOPA clearance over the urinary and hepatic/pancreatic pathways. The change of SUVs in the time from 10 minutes post-injection to the end of measurement at 35 minutes showed wash-out for the heart (-0.2719 SUV/h) and brain (-0.422 SUV/h), whereas the clearance organs liver (0.6181 SUV/h) and kidneys (6.9607 SUV/h) showed increasing SUV rates. The tracer accumulation outside of the chick embryo was negligible.

For FDG, averages of two naïve chick embryos were utilised, as the third naïve embryo had to be excluded due to pronounced underdevelopment. Consequently, the SUV calculated with the total egg weight as corresponding body weight did not accurately reflect the actual physiological condition. The two naïve chick embryos showed nearly constant uptake in the kidneys over the analysed time window of 35 minutes, with a mean SUV of 2.51 ± 0.38. The uptake kinetics of heart and liver were nearly identical, with a slight decrease of FDG uptake over time with comparable mean SUV for the heart (SUV_{heart} = 2.12 ± 0.29) and the liver (SUV_{liver} = 2.20 ± 0.43). The brain uptake showed a constant uptake increase of tracer uptake, with a mean SUV of 1.49 ± 0.23. The change of SUV in the time from 10 minutes post-injection to the end of measurement at 35 minutes showed increasing brain uptake with a rate of 1.0116 SUV/h. The other regarded organs showed declining rates, with the highest decline in the liver (-0.4942 SUV/h), followed by the heart (-0.4342 SUV/h), and the lowest decline in the kidneys (-0.144 SUV/h). The extra-embryonal tracer accumulation in the chick embryo’s allantois was negligible.

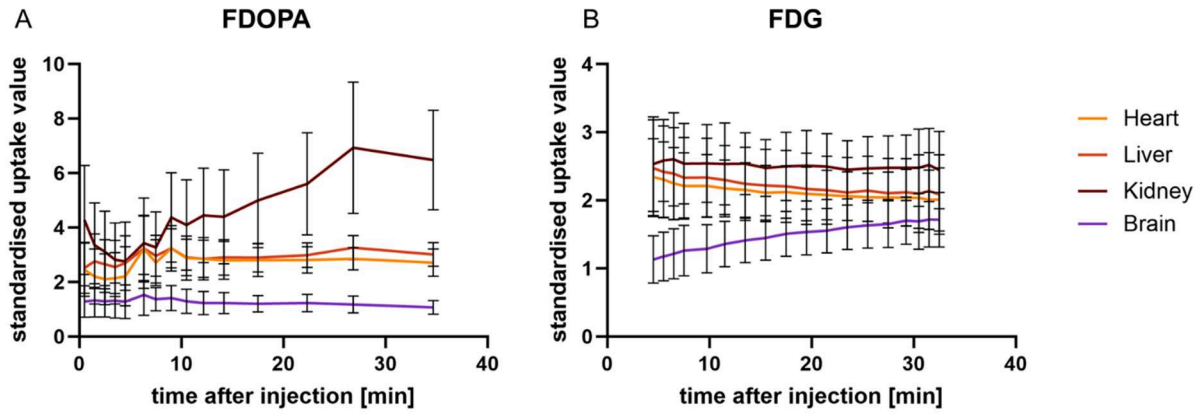

Figure 21: Time-activity curves of FDOPA and FDG in relevant chick embryo organs. A: Averaged time-activity curves of FDOPA uptake of three naïve chick embryos in heart, liver, kidney, and brain. High mean uptake values can be found in the kidney, indicating urinary excretion. A plateau of constant radiotracer in heart, liver, and brain can be found ten minutes after injection. B: Averaged time-activity curves of FDG uptake of two naïve chick embryos in the respective organs. Nearly constant FDG levels can be found in heart, liver, and kidneys, whereas the brain shows a constant increase of FDG uptake over time.

Thus, all three radiotracers show radiotracer accumulation inside the embryo after the injection.

As possible injection control, the utilisation of a new parameter is introduced in this thesis: The fraction of injected dose (FID) could be used as injection control parameter in radiotracer evaluations where the injected radiotracer is accumulated in the embryo itself. For this, chick embryos were extracted from the egg after finalisation, and were measured in a gamma counter. The radiotracer uptake of each embryo could be calculated back to the amount of tracer that went into the embryo at the time of injection, as control for functional injections. The FID was thus calculated by dividing the recalculated dose measured in the chick embryo by the overall injected dose. Thus, values between 0 and 1 could be achieved, with higher values showing more ideal injection processes in radiotracers known to accumulate in the embryo. This value could be utilised to control injections in µPET for a quantification of correct injected dose for partial correct injections, as well as in *ex ovo* AR, where no functional injection would be otherwise validated due to the missing of an overall image of the egg after injection. Exemplarily, the FID for the neuroblastoma CAM study is shown in Table 4, where chick embryos utilised for *ex ovo* AR, as well as chick embryos with additional µPET measurement (highlighted in light blue) were tested for their FID parameter.

Table 4: Overview of injection control in the neuroblastoma chick embryo CAM model with recalculated dose inside the embryo based on ex ovo extraction and gamma counter measurement for all ex ovo autoradiography subjects. In light blue, the chick embryos that have been additionally measured with µPET are highlighted.

Radiotracer	Cell line	Injected dose [MBq]	Dose inside embryo, recalculated for injection time [MBq]	Fraction of injected dose [-]
FET	LAN-1	10.67	8.59	0.81
		7.03	5.00	0.71
		10.88	7.86	0.72
	SH-SY5Y	7.60	5.89	0.78
		9.34	6.37	0.68
		6.12	3.99	0.65
FDG	LAN-1	7.58	5.63	0.74
		5.37	2.93	0.55
		7.88	6.69	0.85
	SH-SY5Y	6.42	5.46	0.85
		7.65	5.07	0.66
		9.19	6.68	0.73
FDOPA	LAN-1	10.47	8.34	0.80
		12.92	8.11	0.63
		12.93	9.29	0.72
	SH-SY5Y	9.90	8.85	0.89
		12.02	8.65	0.72
		11.62	7.49	0.64

In the following, the influence of the FID parameter to the respective CAM tumour tracer uptake was considered (n = 19). A significant correlation of FID towards CAM tumour uptake based on *ex ovo* AR could be found, as shown in Figure 22 (one-tailed Pearson correlation, r = 0.4567, p = 0.0247). Across the observed range, the relationship was consistent, with the exception of a single data point at FID = 0.55, which deviated markedly from the otherwise positive trend.

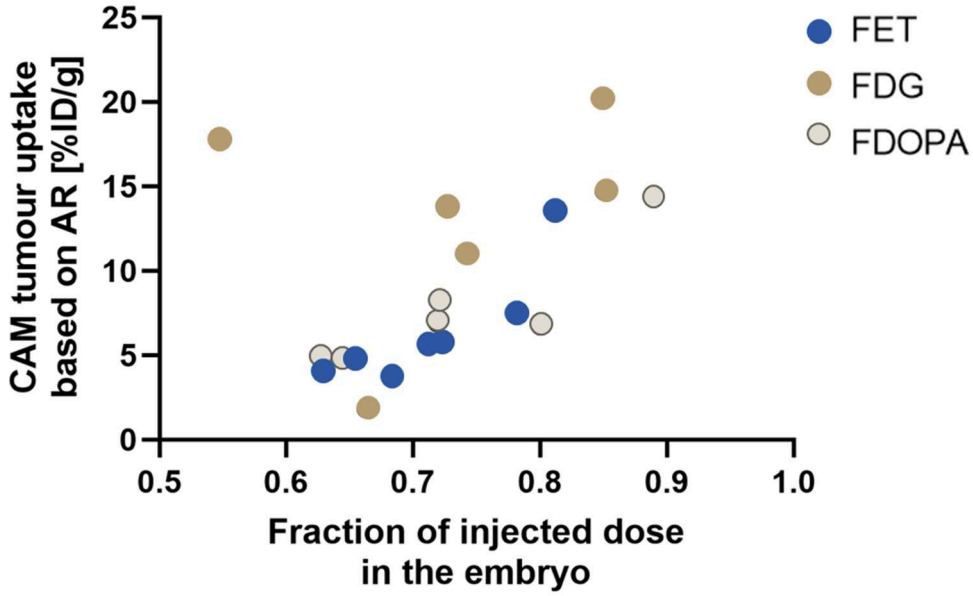

Figure 22: CAM tumour uptake in relation to the fraction of injected dose in the embryo (n = 19). A statistically significant correlation was found (Pearson correlation, r = 0.4567, p = 0.0247).

For the determination of a cut-off value of reliable data acquisition in the field of CAM tumour uptake studies, the biological meaningfulness of the parameter FID needed to be explained. For the regarded radiotracers FET, FDOPA and FDG, where an accumulation of radiotracer in the embryo took place one-hour post-injection, lower FID scores indicate an inferior injection performance. The tested radiotracers did not get reabsorbed in the considered time when injected paravenous into the CAM, and thus stayed at the injection area. Thus, CAM tumours in tight proximity of those paravenous tracer poolings could possibly take up radiotracer via facilitated diffusion effects, rather than the wanted intravenous application route. The higher the FID score, the more radiotracer activity was correctly applied into the CAM vessel, resulting in more reliable results for i.v. injection modelling. The CAM tumour uptake in relation to the FID showed an increasing CAM tumour uptake from 0.6 to 0.9 FID with an equal distribution of considered radiotracers for follow-up comparison of radiotracer performances. However, the FDG data point with the lowest FID score showed a comparably high uptake. No experimentation-wise criterium argued for an exclusion of this experiment. Thus, based on these test data, trendlines up to a quartic function were considered for a mathematical depiction of cut-off value (Figure 23). The local minima for all considered fits were similar at an FID score between 0.6 and 0.7. Thus, the most conservative break-point of 0.6 was chosen for a minimal exclusion of data points, in line with the animal welfare and considering the need of more data points with different operators, especially in the lower FID score range for more robust modelling.

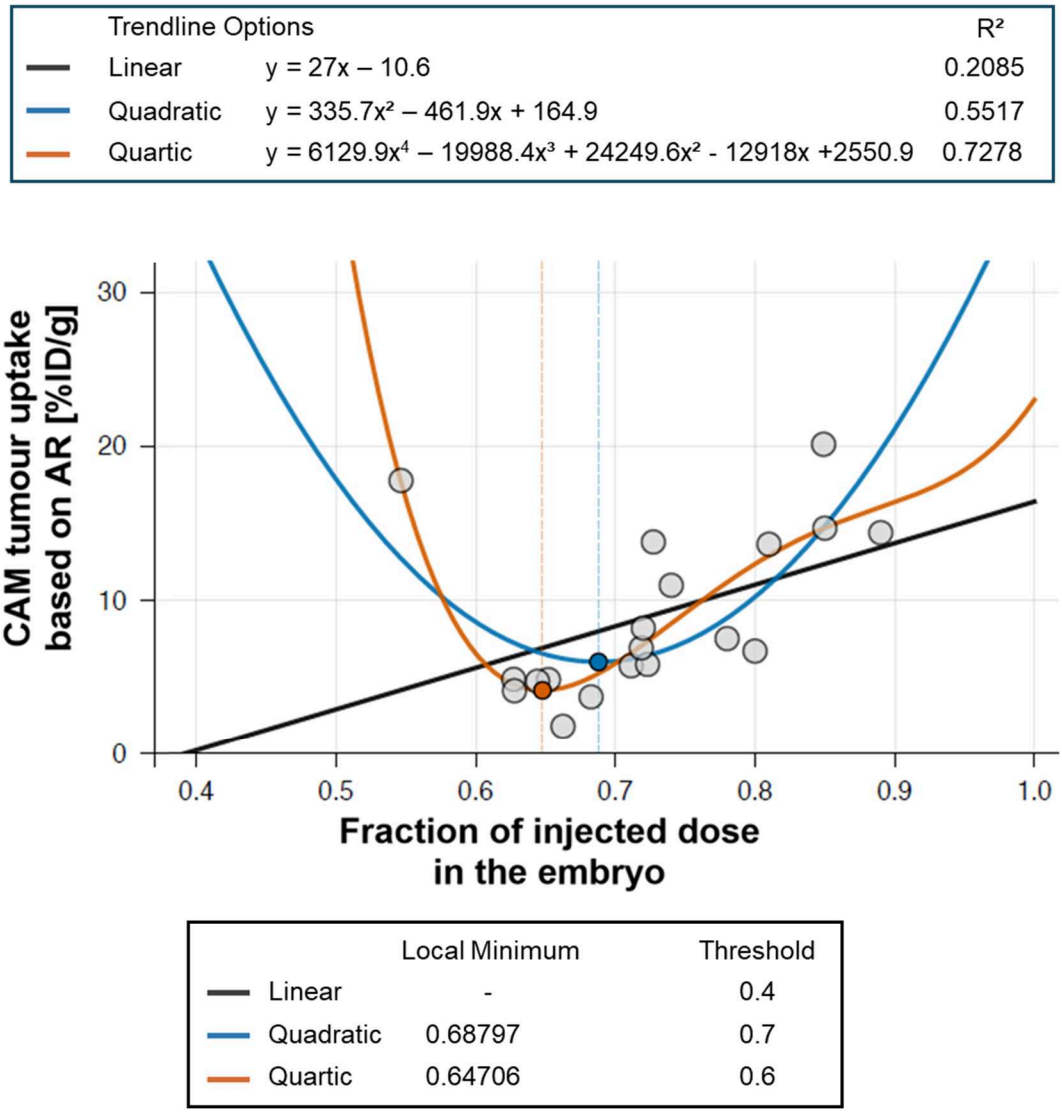

Figure 23: Determination of cut-off values for FID scores in CAM tumour uptake studies based on trendline options. Similar local minima in the range of 0.6 to 0.7 could be revealed.

Other inherent parameters to validate the methodological approach within the chick embryo CAM model were considered. First, influences of the fluctuations of the injected dose of radiotracers were considered. The injected dose was 9.49 ± 2.45 MBq for the tested cohort (n = 19). No significant correlation between the injected dose and the CAM tumour uptakes was found (Pearson Correlation, r = 0.1456, p = 0.2760). Also, the correlation of CAM tumour weights to CAM tumour uptake did not reveal any influence on the results (Pearson Correlation, r = -0.2538, p = 0.1472).

4.3.2.2 Refinements for µPET Measurements in CAM Radiotracer Experiments in Chick Embryos

For the validation of tumour uptakes based on CAM tumour VOI placements in a µPET image, the radiotracer uptakes of the naïve CAM were considered as background value. For the tested radiotracers, the CAM uptake was homogenous on the whole CAM surface based on PET images. Thus, a region outside of the injection point was marked as a VOI in the naïve PET image. The averaged CAM uptake values, as mean

FET and FDOPA uptake values of the three naïve chick embryos and the two naïve chick embryos for FDG, are summarised in Table 5.

Table 5: Static CAM uptakes in naïve chick embryos, injected with a mean of 8.7 ± 1.6 MBq of the radiotracers FET, FDOPA, and FDG, in mean [kBq/ccm] with Sd.

	FET n = 3	**FDOPA n = 3**	**FDG n = 2**
averaged CAM uptake in naïve chick embryos [kBq/ccm]	60 ± 73	59 ± 37	120 ± 44

As the averaged CAM uptake of FDG was twice as high as of FET and FDOPA, which were both similar in CAM uptake, the CAM uptake was evaluated in more detail. Dynamically, the tracer uptake of the CAM is summarised in Figure 24. The CAM uptake of FDG (n = 2) only showed a slight decline over time, with overall higher values than FDOPA and FET (both n = 3). Also, the standard deviation of FDG was high, which is related to the small sample size. FDOPA and FET showed qualitatively a similar mean CAM uptake, but the FET uptake increased over time in all three embryos whereas FDOPA showed a constant uptake value with a lower standard deviation. Based on this, high variations in CAM uptake were considered in the analysis of CAM tumour radiotracer uptakes of FET, FDOPA, and FDG. Thus, all of the following PET CAM tumour analyses were corrected by subtraction of the respective background CAM uptake in each subject.

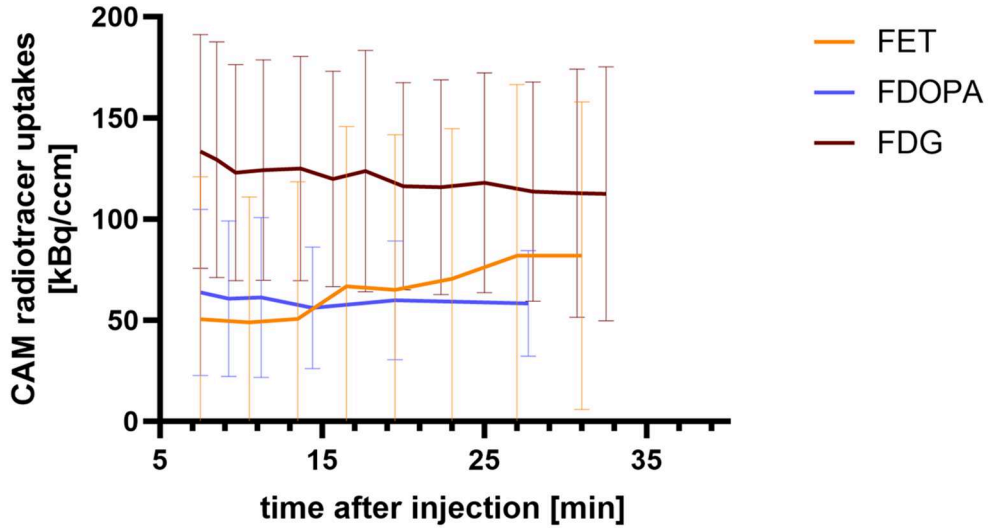

Figure 24: Time-activity curves of the naïve chick embryo CAM for radiotracer FET (n = 3), FDOPA (n = 3), and FDG (n = 2). Overall higher CAM uptake is visible for FDG with a slight decline over the regarded time. For FDOPA, the level in naïve CAM was constant, while FET showed an increase over the observation time. All data are shown in mean with standard deviation.

In some radiotracer injections, a small volume of radiotracer remained paravenous on the surface of the CAM due to the difficulty of vessel clamping in a fluid environment, as discussed in Chapter 4.3.2.1. For those cases, the distinction between CAM tumour uptake and paravenous residue on µPET data were investigated. For this, VOIs were placed on the CAM surface covering paravenous injections in naïve chick embryos and the respective dynamic kinetics for all three radiotracers were investigated. Depending on the activity concentration of the bolus pooling area, the radiotracer uptake during measurement start varied heavily, but the uptake kinetics showed a visible decline over the measurement time in all three tested radiotracers. An exemplary TAC for the bolus pooling areas in a naïve chick embryo, compared to a representative CAM tumour uptake dynamic, is shown in Figure 25. For PET analysis with CAM tumours without a suitable structural imaging modality, VOIs were placed at every CAM region of high uptake, and were rated based on their dynamic uptake kinetics between bolus pooling area and potential CAM tumour uptake. Additionally, the CAM tumour uptake was verified based on correlation between PET uptake versus uptake after extraction in a following *ex ovo* autoradiography. In all measurements involving CAM tumours, radiotracer injections were performed in veins distant to the CAM tumours to avoid a signal fusion of paravenous tracer and real CAM tumour uptake on PET data.

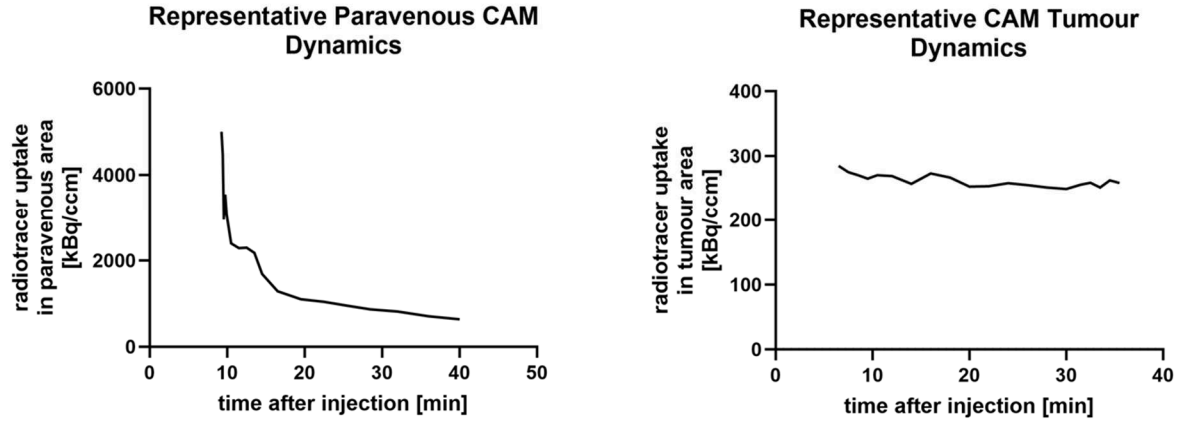

Figure 25: Time-activity-curve of a representative paravenous CAM VOI (left) in a naïve chick embryo compared to a representative CAM tumour radiotracer dyamic (right). The occurrence of paravenous radiotracer finding is limited to cases of insufficient vessel clamping after injection, or failed paravenous injections. Thus, only exemplary cases can be shown due to the limited sample size. In comparison, a representative CAM tumour uptake dynamic is shown on the right with nearly constant radiotracer uptake.

Another methodological aspect to-be-considered in µPET CAM tumour evaluation was the localisation of the CAM tumour in relation to the chick embryo (Figure 26). The FET injected, LAN-1 containing egg served as representative example of a chick embryo filling up the whole space of the egg, with the small CAM tumour growing on the CAM directly above the abdomen, where high radiotracer signals due to the proximity to heart and liver would be expected. Thus, a generally higher signal might be due to the difficulty of accurately placing the small VOI into the CAM tumour without having voxels of shared uptake from the embryo itself. Thus, for these tumour sizes, the quantification accuracy was expected to be heavily affected by partial volume effects. Compared to the FET sample, the FDG injected counterpart exemplified the opposite situation: an

underdeveloped embryo was found that was visually smaller than the FET chick embryo. Thus, calculations for the SUV, with the whole egg as reference weight, overestimate the SUV uptake of the CAM tumour, as the weight of the whole egg is declining over the incubation period. Compared to the FET chick embryo, the small-sized tumour VOI might also include surrounding voxels, where no signal could be observed, leading to a potential spill-out of actual tumour uptake.

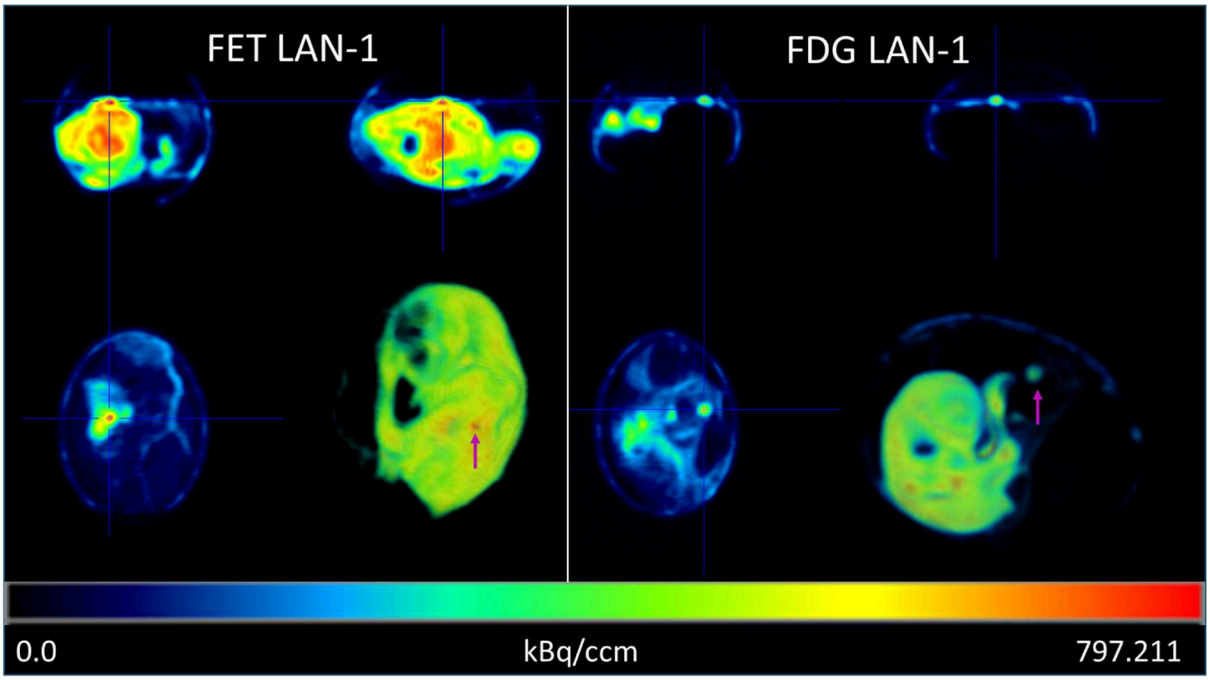

Figure 26: Pitfalls of the chick embryo CAM PET analysis based on chick embryo localisation, with examples of the LAN-1 CAM tumours for FET (left) and FDG (right). In the FET image, a chick embryo that is filling up the whole space of the egg is seen, with the small CAM tumour in tight proximity to the high-uptake area of the chick abdomen. Thus, the VOI of this small-sized tumour might include voxels of higher uptake, potentially overestimating the real tumour SUV. In contrast, the chick embryo utilised for the FDG study was visibly underdeveloped, leading to a less accurate depiction of SUV calculations based on the whole egg as reference weight. Besides, the FDG CAM tumour did not show any adjacent signals from the embryo in its localisation, thus, a potential spill-out of actual uptake signal might occur in these small-sized samples.

4.3.2.2 Correlation of PET and AR derived Uptake Values in CAM Tumours

Comparable to the correlation for FET brain SUV in Chapter 4.3.2, a pairing of neuroblastoma CAM tumour uptakes, derived by µPET and *ex ovo* autoradiography was analysed for congruency between the two methods. In the analysed subjects (n = 6, one for each tracer and cell line), a significant effective pairing, but also a significant bias could be shown (Figure 27 A) (paired two-tailed t-test: $p = 0.0001$; effectiveness of pairing: correlation coefficient: $r = 0.7700$, $p = 0.0366$). Thus, a Bland-Altman plot was considered for a more detailed evaluation of the systematic bias (Figure 27 B), revealing a bias of 4.18. Thus, on average, the AR derived SUV gave values that were consistently 4.18 units higher than the PET derived SUV. The 95% limits of agreement between AR and PET ranged from 2.26 to 6.11 units (dotted lines).

The difference between AR and PET did not meaningfully correlate with tumour weight in the tested data set (Pearson correlation, $r = -0.5384$, $p = 0.2704$, two-tailed). Also, the correlation did not show a variation based on the utilised cell line (two-way RM

ANOVA, p = 0.9597), but a significant difference in the utilised radiotracer was found (two-way RM ANOVA, p = 0.0458). The correlation sets of PET and AR SUV are visualised based on the subsequent radiotracer in Figure 28, revealing nearly parallel combination lines for FET and FDOPA, but FDG showing a more pronounced difference between PET and AR derived SUV. Thus, the comparison of radiotracer uptake solely based on PET might be insufficient for a clear depiction of uptake values. Hence, a more detailed analysis based on high resolution *ex ovo* autoradiography was necessary for a more reliable comparison of radiotracer performances.

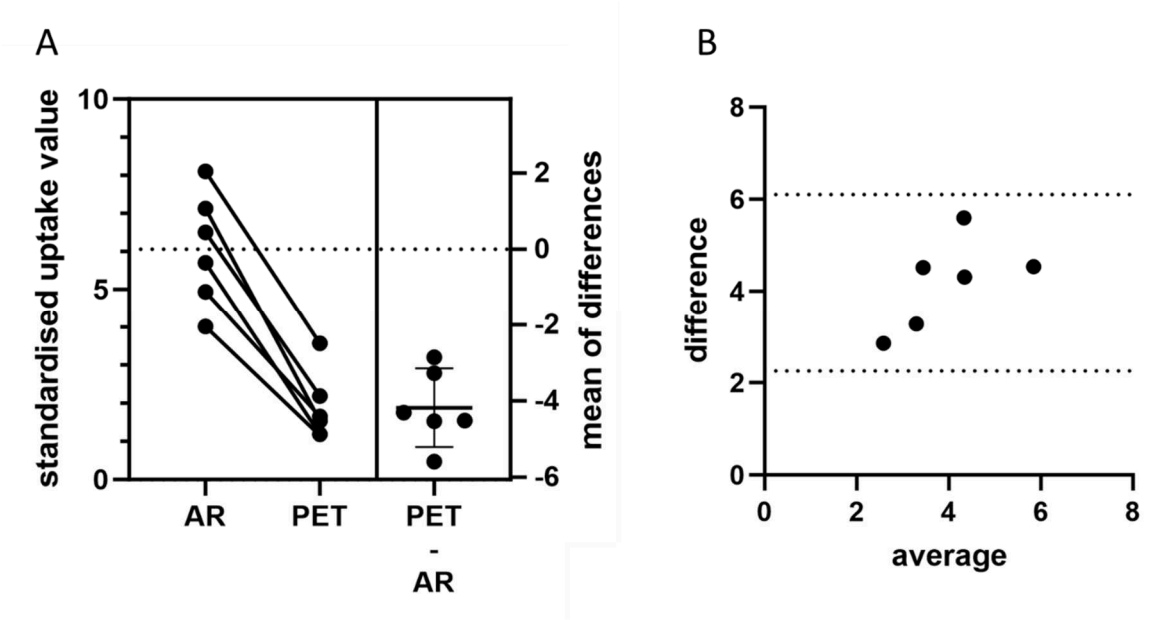

Figure 27: Correlation of radiotracer uptake in neuroblastoma CAM tumours measured by AR and PET. A: Correlation efficiency in the chick embryo neuroblastoma CAM model (n = 6), showing a significant bias (paired two-tailed t-test, p = 0.0001), with a significantly effective pairing (correlation coefficient: r = 0.7700, p = 0.0366). B: Bland-Altman plot illustrating agreement of the two methods, with a positive bias of 4.18. Dashed lines represent the 95% limits of agreement. The plots reveal an effective pairing with AR systematically yielding higher SUV than PET.

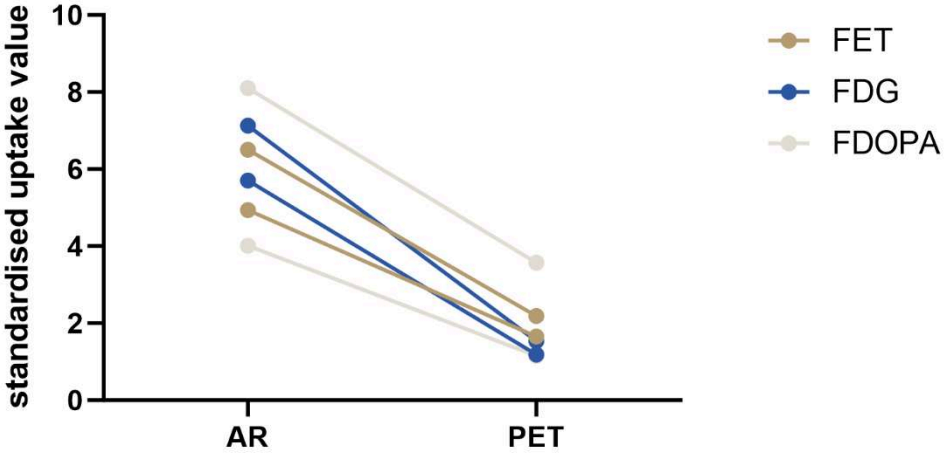

Figure 28: Correlation of SUV derived by AR and PET show a clear difference based on the utilised radiotracer. While FET and FDOPA show near parallel lines and thus near constant positive bias, the samples for FDG show higher difference between AR and PET derived SUV. Due to the partial-volume effects of small-sized tumours in PET measurements, the high-resolution AR provides the more precise modality. Thus, comparison of radiotracer performances based on PET might be insufficient for a clear depiction of SUV in the neuroblastoma CAM model.

4.3.2.4 Adopted Methodology for CAM Tumour Radiotracer Studies

Based on the findings of Chapter 4.3.2, the following changes were made for the evaluation of the neuroblastoma CAM tumour radiotracer study. First, an FID cut-off value of 0.6 was utilised for both µPET and AR. In all injection procedures, CAM veins distinct to the CAM tumour were utilised to minimise the risk of paravenous tracer poolings in close proximity to the CAM tumour to-be-analysed.

For µPET evaluation without structural imaging modality, the suspected CAM tumour VOI was controlled with the dynamic kinetics, as discussed in Chapter 4.3.2.2. In cases of arguable kinetics, the localisation of the embryo in comparison to the tumour VOI was considered. Also, a VOI was placed distinct from the CAM tumour and the injection side individually as background CAM uptake, which was later subtracted from the achieved tumour VOI uptake. For values to-be-compared to patient values, the uptake was given as SUV. For comparison with each other, the activity concentrations were given in kBq/ccm to avoid additional normalisation-related bias due to the missing standard control weight.

For AR evaluation, the tumour uptake was given in %ID/g and was normalised to the injected dose for more comparability. As no image of the whole egg was acquired with this methodology, the quantification of correctly intravenously injected radiotracer had to be carefully considered.

4.3.3 Radiotracer Uptakes of Neuroblastoma CAM Tumours based on µPET

In the following, the radiotracer uptakes of neuroblastoma CAM tumours were performed for the clinically established radiotracers FDG and FDOPA and compared to the standard PET tracer FET that has not been utilised for these tumours yet.

In the following, the radiotracer uptakes of the CAM tumours are analysed. For each radiotracer, one chick embryo with a LAN-1 CAM tumour and one with an SH-SY5Y CAM tumour were utilised for µPET evaluation. From those overall six samples, three small paravasal tracer poolings could be found on the CAM surface for FDG SH-SY5Y, FDOPA LAN-1 and FDOPA SH-SY5Y. However, as shown in Table 4, most of the utilised radiotracer was injected correctly based on the dosage of the chick embryo at the end of measurement with FID values above 0.6. Besides, the bolus poolings were located distant from the CAM tumour, not influencing the results of the respective VOIs. Thus, these measurements were not excluded from analysis. Due to the influence of CAM uptake differences from the three radiotracers (Table 5), as well as the different CAM uptake kinetics (Figure 24), a distinct CAM VOI was subtracted from the CAM tumour VOI for a depletion of background signal for each embryo.

The PET-derived SUV_{mean} and SUV_{max} values are visualised in Figure 29. Both tumour cell lines showed similar values for the radiotracers FET and FDG. For FET, the averaged SUV_{mean} was 1.92 and SUV_{max} 3.12; for FDG, the averaged SUV_{mean} was 1.36 and SUV_{max} 2.06. In contrast, the two different tumour lines exhibited proficient differences in uptake for FDOPA, with higher SUV observed for the SH-SY5Y CAM

tumour while the LAN-1 tumour showed values in the range of the other radiotracers ($SUV_{mean,FDOPA}$ = 2.36 and $SUV_{max,FDOPA}$ = 2.85). No statistically significant differences between the radiotracers could be found (two-way ANOVA, p = 0.4805).

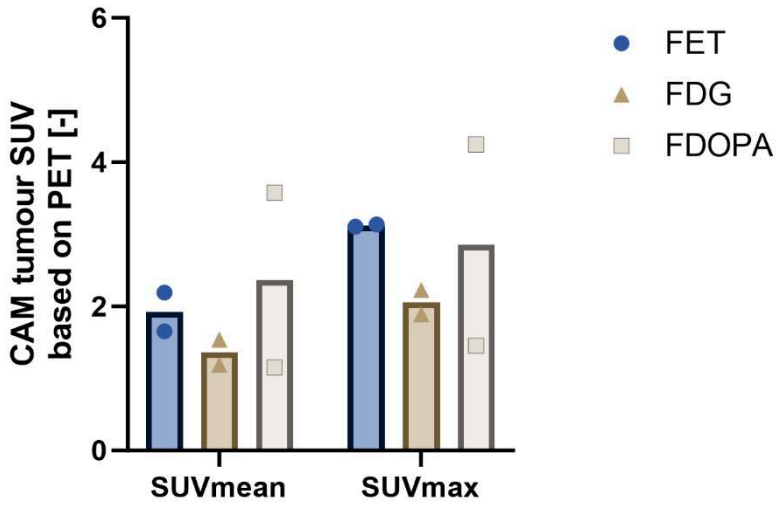

Figure 29: Radiotracer evaluation based on derived SUV_{mean} and SUV_{max} values, comparing FET, FDG, and FDOPA in CAM tumours of the neuroblastoma lines SH-SY5Y and LAN-1. No statistically significant differences were observed (two-way ANOVA, p = 0.4805).

For an evaluation of dynamic tracer uptakes of the CAM tumours, TACs for all six subjects are shown in Figure 30. For each sample, the dynamic naïve CAM VOI was subtracted dynamically for a depletion of background signal. In most cases, a constant tracer uptake of approximately 200-300 kBq/ccm could be observed. The FDOPA SH-SY5Y CAM tumour exhibited overall higher uptake levels with a slight increase and decrease over the measurement time of 30 minutes. The LAN-1 CAM tumour measured with FET, as well as the FDOPA SH-SY5Y CAM tumour showed a decline of tracer level over time.

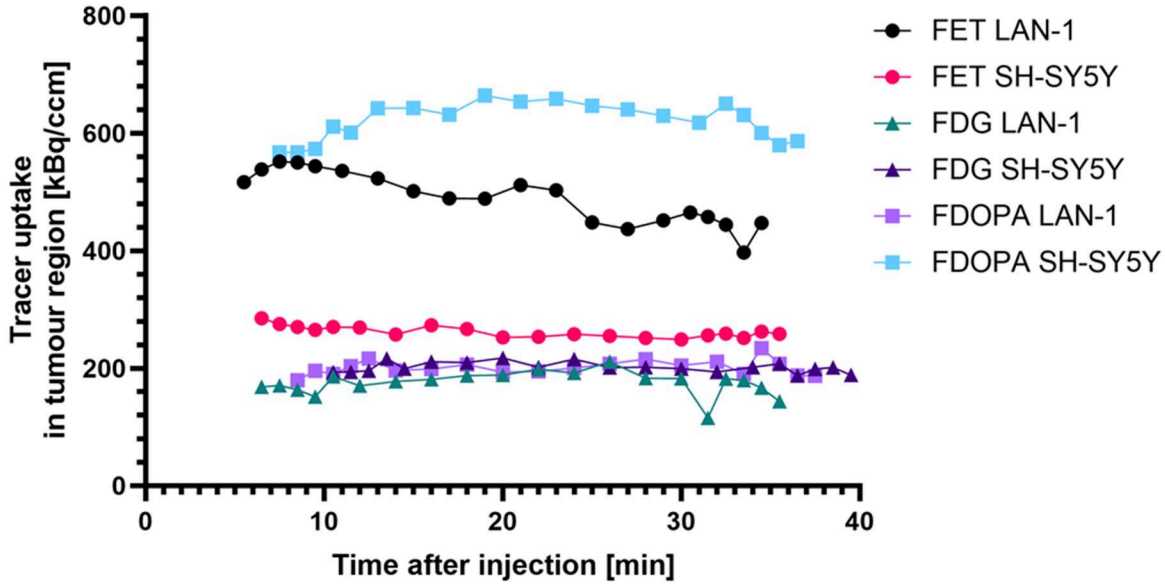

Figure 30: Time-activity curves of CAM tumours from the cell lines LAN-1 and SH-SY5Y for the radiotracers FET, FDG, and FDOPA. For each sample, the dynamic uptake of a region of naïve CAM was subtracted as background value.

For a further validation of the FET LAN-1 signal, as a paravenous VOI could not be excluded without a corresponding structural image and based on the declining TAC of this sample, the embryonic positioning was considered, as shown in Chapter 4.3.2.1.

4.3.4 Radiotracer Uptakes of Neuroblastoma CAM Tumours based on *ex ovo* AR

The analysis of radiotracer uptake based on *ex ovo* autoradiography was performed on 20 µm slices after co-registration with adjacent slices stained with a human nuclei antibody. An example of *ex ovo* autoradiography, the corresponding human nuclei staining and the resulting ROI is visualised in Figure 31. As explained in Chapter 4.3.1, the extracted CAM tumours showed infiltrative cluster growth on the CAM for both cell lines, thus, every tenth slice was stained, co-registered, and all slices for each CAM tumour were summarised and averaged. Based on the FID cut-off of 0.6, one sample of the FDG group with a LAN-1 CAM tumour was excluded from analysis (Table 6). The corresponding radiotracer uptakes, tumour and egg weights, as well as the recalculated SUV based on *ex ovo* AR are shown in Table 6 and Figure 32.

The mean activity concentration (AC) for CAM tumours normalised to the injected dose per gram (%ID/g) derived from the cell line LAN 1 was 8.40 ± 3.70 %ID/g for FET, 15.54 ± 4.58 %ID/g for FDG, and 6.15 ± 0.91 %ID/g for FDOPA. Thus, the mean activity concentration for FET was in the middle of the three tested radiotracers. FDOPA showed the lowest mean AC for LAN-1 tumours of the three radiotracers with the lowest standard deviation. For CAM tumours derived from the cell line SH SY5Y, FDG showed the highest tracer concentration with 10.08 ± 5.86 %ID/g with the highest standard deviation, followed by FDOPA with 9.10 ± 3.99 %ID/g. FET showed the lowest tracer concentration with 5.36 ± 1.57 %ID/g. Generally, no significant differences in the utilised radiotracer (two-way ANOVA, $p = 0.1338$) or in the tested cell lines (two-way ANOVA, $p = 0.4403$) were found. Šídák's multiple comparisons of radiotracer performances showed no significant differences for LAN-1 or SH-SY5Y CAM tumours, with the lowest p value above 0.5 while comparing FDG and FDOPA performance in LAN-1 tumours ($p_{\text{FDG LAN-1 vs. FDOPA LAN-1}} = 0.5472$).

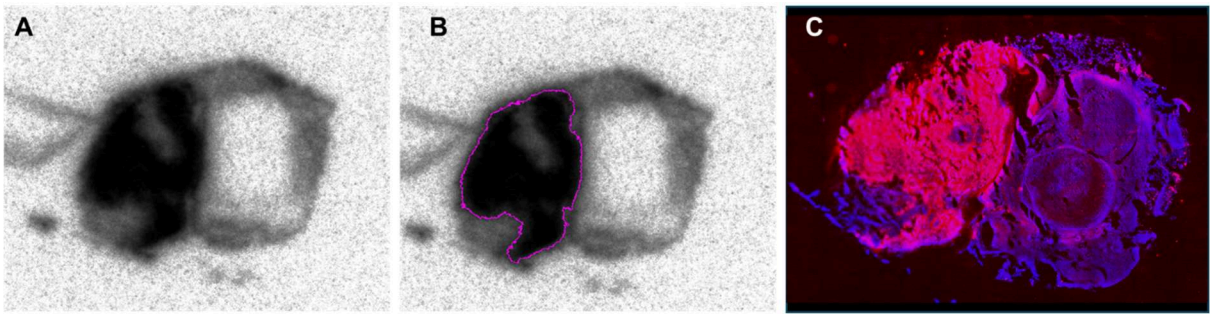

Figure 31: Example of ROI placing for the analysis of tracer uptakes in ex ovo autoradiographies, exemplary on an SH-SY5Y CAM tumour utilised in the FDG study. A: CAM tumour after ex ovo autoradiography; B: ROI placement based on C; C: Human nuclei immunofluorescence staining, revealing cells of human origin in red and cell nuclei in blue.

The mean activity concentration (AC) for CAM tumours normalised to the injected dose per gram (%ID/g) derived from the cell line LAN-1 was 8.40 ± 3.70 %ID/g for FET, 15.54 ± 4.58 %ID/g for FDG, and 6.15 ± 0.91 %ID/g for FDOPA. Thus, the mean activity concentration for FET was in the middle of the three tested radiotracers. FDOPA showed the lowest mean AC for LAN-1 tumours of the three radiotracers with the lowest standard deviation. For CAM tumours derived from the cell line SH-SY5Y, FDG showed the highest tracer concentration with 10.08 ± 5.86 %ID/g with the highest standard deviation, followed by FDOPA with 9.10 ± 3.99 %ID/g. FET showed the lowest tracer concentration with 5.36 ± 1.57 %ID/g. Generally, no significant differences in the utilised radiotracer (two-way ANOVA, p = 0.1338) or in the tested cell lines (two-way ANOVA, p = 0.4403) were found. Šídák's multiple comparisons of radiotracer performances showed no significant differences for LAN-1 or SH-SY5Y CAM tumours, with the lowest p value above 0.5 while comparing FDG and FDOPA performance in LAN-1 tumours ($p_{\text{FDG LAN-1 vs. FDOPA LAN-1}} = 0.5472$).

Table 6: Overview of radiotracer uptakes normalised to the injected dose, egg weights, as well as recalculated SUV based on ex ovo autoradiography for the CAM neuroblastoma study. Chick embryos with an additional PET measurement are highlighted in blue. In light red, the excluded chick embryo based on an FID value of 0.55 < 0.6 is shown. The order of subjects corresponds to Table 4.

Radiotracer	Cell line	Radiotracer uptake [%ID/g]	Weight egg [g]	SUV based on AR [-]
FET	LAN-1	5.74	47.7	6.50
		13.63	57.5	3.30
		5.83	48.5	2.83
	SH-SY5Y	3.72	48.2	4.93
		7.51	54.6	2.03
		4.84	57.6	2.79
FDG	LAN-1	10.96	52	5.15
		17.76	49.5	8.79
		20.12	50.3	10.12
	SH-SY5Y	14.67	48.6	6.20
		1.81	46.6	0.84
		13.78	48.1	6.62
FDOPA	LAN-1	6.69	59.9	3.65
		4.86	57.8	2.81
		6.89	56.1	3.87
	SH-SY5Y	14.37	56.4	7.04
		8.19	54.2	4.44
		4.74	54.9	2.60

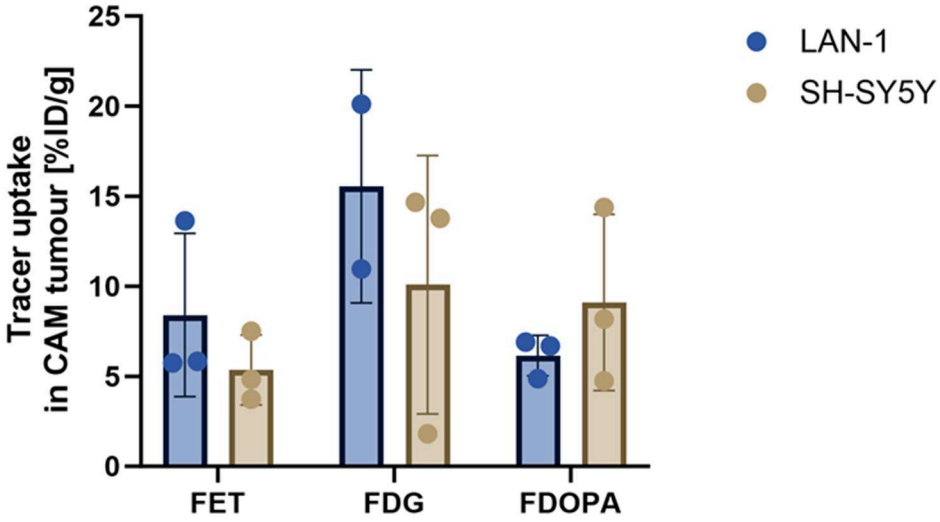

Figure 32: Radiotracer uptakes of neuroblastoma CAM tumours based on ex ovo autoradiography. Per group, three chick embryos with a LAN-1 or SH-SY5Y CAM tumour have been utilised. One FDG LAN-1 chick embryo had to be excluded due to insufficient FID. No significant differences in the utilised radiotracer (two-way ANOVA, p = 0.1338) or in the utilised cell line (two-way ANOVA, p = 0.4403) were found.

As no statistically significant differences with the utilised neuroblastoma cell line could be found, the two cell lines were combined for a further radiotracer comparison (Figure 33), validating the missing statistically significant differences (one-way ANOVA, p = 0.1636).

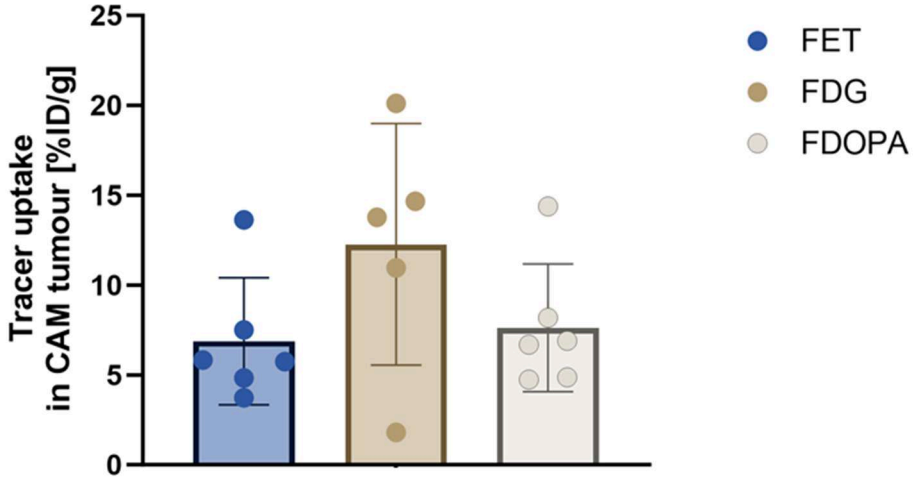

Figure 33: Radiotracer uptakes of both neuroblastoma cell lines LAN-1 and SH-SY5Y combined in the chick embryo CAM model (n = 12). A fraction of injected dose below 0.6 was used as cut-off value for the exclusion of the sample. No significant differences in the utilised radiotracer was found (one-way ANOVA, p = 0.1636).

5 Discussion

5.1 Considerations of Chick Embryo Tumour Research

All procedures and interventions were performed in strict alignment to regulatory policy for Germany and EU guidelines. Even though efforts for the protection of chick embryos have been made, especially in Germany, this model is still not considered as an animal in a regulartory sense. For the establishment of animal welfare aspects in chick embryo research, insights and expertise from rodent cancer research were adapted accordingly: In the field of brain tumour research, humane endpoints in rodents are often based on the combination of clinical and behavioural indicators as weight loss, reduced mobility, neurological impairments, failure of maintaining normal grooming, social interactions as well as frequent tumour growth monitoring via non-invasive imaging, such as MRI.

However, most behavioural considerations remain hard to detect and track in a chick embryo whilst *in ovo*, as shown with the behavioural tests performed to observe nociception by Süß and colleagues [139]: The authors state limitations based on coordinated movements that physiologically appear around EDD 17. Consequently, it is difficult to determine whether the observed motions are reflexes or coordinated movements. Also, the invasiveness of the experimental setup for the detection of motion, as the exposure of the embryo for visual access, might pose stress in itself. Together with the unphysiological fenestration of the eggshell that also influences the light exposure of the embryo, the avian behaviour might be altered due to stress [139]. Thus, behavioural alterations for humane endpoint determination were considered unreliable in this thesis.

Regarding the embryonal weight, only the whole egg could be measured longitudinally, where a weight loss is physiological and even crucial for chick development, as water evaporation is needed for the embryo to ultimately pip internally and start lung ventilation [150]. Thus, the egg weight fails as a marker of humane endpoint of tumour research, as well.

Thus, the tumour growth was monitored non-invasively with MR measurements using optimised egg coils. With this method, the tumour growth inside the brain was monitored and compared to in-house rodent tumour sizes that did not reach humane endpoints, offering more objective monitoring than behavioural tests. With the development of the specialised coil by Dr. Chang-Hoon Choi, the animal experimentation was firstly replaced by utilising simulation models, verifying the results on unfertilised supermarket eggs, and only afterwards finally validated with a low number of chick embryos. With the increased SNR at the end regions of the egg shape, the head of the chick embryos could be screened for excessive tumour growth for newly utilised cell lines with unknown growth kinetics in an embryonal environment. However, differences in avian and mammalian nociception might need further considerations in the future to ensure the validity of humane endpoint extrapolation

from rodents to chick embryos. Another drawback is the considerable effort required by this imaging procedure, limiting its throughput.

Implementing the findings by Kollmansperger and colleagues, who showed that nociception cannot be ruled out after physiological EEGs start to appear on EDD 13 [140], no invasive procedure was performed without deep anaesthesia with analgesic effect with embryos older than EDD 13. As all brain tumour inoculations were performed on EDD 5, nociception could be excluded. The CAM is not innervated, however, also these implantations take place before EDD 13, so that pain due to the invasive procedure can be ruled out, as well. Thus, no adaption of timings of interventions was required for refinement in accordance with the 3R principles. All finalisations took place under deep anaesthesia with analgesic effect by rapid decapitation.

Besides, an internal animal welfare team was established and consulted for chick embryo experiment approval to enforce a clear justification for the utilisation of this model before the start of studies, mimicking the German animal experiment application.

Also, analoguous to the replacement strategy in animal models, alternatives for the utilisation of chick embryos were considered. Whenever possible, *in vitro* tests were utilised in research instead of testing in the embryo.

Animal experiment reduction was ensured by suitable research planning, starting with few chick embryos and gradually increasing the number until the research question was answered sufficiently. Control groups of one *in ovo* experiment might be taken as *in vitro* control group for new study ideas by freezing organs, enabling the establishment and validation of staining protocols or other *in vitro* characterisation methods prior to testing substances in developing chick embryos. However, the aim to reduce animals is counteracted by the occurring developmental failure rates, as observed in Chapter 4.1.1, where even the naïve control chick embryos that were solely windowed showed high drop-out rates. Depending on the cohort, these developmental failure rates in control embryos varied strongly (data not shown, developmental failure rates varying from 30% to up to 80%). Several reasons for high developmental failure rates have to be considered. Firstly, the windowing itself poses the risk of procedure-related mortality, with mechanical stress due to the vibrations and movements, for example of the air bubble, as well as temperature fluctuations during the handling. In eggs, where the repositioning of the air bubble happened with too much force, the corresponding embryos were sometimes twisted into an s-shape with lethal outcome. The tested repositioning of s-shaped embryos did not demonstrate a statistically better outcome based on the survival after intervention (Figure 11), indicating the severity of small deviations from the normal procedure on the embryo in these early and critical developmental stages. The repositioning of the embryo even increased the lethality within the following days which might be due to the invasive nature and stress of the intervention. Still, one embryo survived the repositioning, which might indicate a slight overall viability increase that could increase with higher

sample sizes and a learning effect of the operator. Generally, temperature fluctuations during the windowing procedure itself did not result in increased mortality in chick embryos that were not windowed, but exposed to the same environment during windowing (data not shown). Thus, the temperature drop during the time of windowing was considered negligible. Another factor that was considered as potentially decreasing the viability is the static positioning of the egg, as physiologically, the egg is turned by the hen regularly. The turning of the egg is especially important to prohibit the attachment on the inner eggshell membrane. However, an attachment to this membrane is necessary for a smooth windowing process; and after the fenestration, the turning function of the incubator would lead to egg content spilling. Thus, the turning function was switched off for the whole incubation time. The non-windowed control group did not show considerable viability loss due to this missing turning (data not shown). The utilisation of closed control groups was only performed for the analysis of these incubation conditions, as the closed system highly prohibits egg manipulation, limiting its value while increasing the utilised chick embryo number. Due to the considerable differences in viability across cohorts, appropriate control groups need to be included in each cohort. Fenestrated control groups can be monitored more easily, while also offering the opportunity to practice non-painful procedures, such as administering low-volume physiological saline injections into the CAM.

High differences in viability between all cohorts might indicate preincubation storage issues, as the time between the hens laying the eggs and the start of experiment is unknown. Also, specific pathogen-free (SPF) eggs are utilised in these studies, potentially increasing the general susceptibility to contamination due to possible disruption of the cuticle: This outer thin layer of the eggshell consists of polysaccharides, proteins and lipids, and physiologically acts as the primary barrier against microbial penetration by covering the pore surfaces [151]. A damaged or missing cuticle, for example after chemical wash-off, increases the risk of potential pathogenic microorganisms reaching the developing embryo, as shown for Salmonella penetration after cuticle damage by Wang and Slavik in 1998 [152]. Generally, efforts for replacing conventional decontamination strategies have been made in the field of poultry hatcheries but also for food industry due to the impact on chick viability [153–155]. A bacteriological examination revealed the presence of various bacteria in dead-in-shell embryos, most predominantly with *Escherichia coli, Klebsiella spp.,* and *Staphylococcus spp*. in approximately 82% of total isolates of a study by Hananeh and colleagues [156], revealing several ubiquitously found bacteria as potential causes for embryonic mortalities. Even though the risk of high developmental failure rates might be increased in SPF eggs compared to conventional unwashed eggs, which leads to high numbers of experimental animals, all research was conducted in SPF eggs to ensure reproducibility. The egg distributor utilised in the studies of this thesis describes high standards and provides strict microbiological quality control of their SPF eggs; however, the integrity of the cuticle is not explicitly assessed. The possibility of disrupted, thinned or even lost cuticle might increase the developmental failure rates to the susceptibility of bacteria penetration through the washed eggshell. Even though

the eggshells were tested clean by the distributor, a potential exposure to ubiquitous bacteria during the incubation cannot be ruled out, as the egg incubator was utilised in a conventional laboratory area with shared ventilation of adjacent laboratories. Further research should focus on improving the chick embryo viability to gain a deeper understanding of the underlying causes of developmental failure variability in-between cohorts, thereby increasing the robustness and practical applicability of the model.

5.2 Evaluation of the Intracerebral Glioma Chick Embryo Tumour Model

Parts of this chapter have previously been published in Krause et al. 2025 [149].

5.2.1 Validation of the Intracerebral Tumour Inoculation Approach

Despite recent advances in the utilisation of chick embryos for preclinical research, a technically functioning implantation method for intracerebral tumour research has proven to be technically challenging with only few published studies [135, 134, 157, 142, 143, 136]. Cretu and colleagues published a technique for pressure-injecting glioma and gliosarcoma cells into the midbrain ventricle on EDD 6 with a pneumatic pico-pump [135], demonstrating the vascularisation and invasive patterns after two weeks, similar to those in rodent models. However, no mortality rates from this technique were disclosed [135]. Boulland and colleagues showed their approach of xenotransplantation in a video article, where chick embryos of HH stages 12 to 18, which is approximately EDD 3-4, were utilised for neural tube injections by pico-pump pressure-injections. The mortality rate of their procedure is also not disclosed; however, the authors state that “post-injection mortality of the embryos is the principle limiting factor” [134]. In a follow-up study, Boulland and colleagues utilised this technique for the evaluation of an intracellular labelling and *in vitro* and *in vivo* tracking system of human cells in chick embryos and mice [157]. Another method was utilised by Cage and colleagues for HH 11-12, which is approximately EDD 2. Their injection technique involved a P20 pipette and was located into the dorsal surface of metencephalon, as evaluation of disseminated medulloblastoma. Also here, no implantation-derived mortality rate was disclosed [142]. In a study by Pace and colleagues, a pneumatic pico-pump was used for glioblastoma injection in matrigel-suspension into the chick optic tectum on EDD 5. Neither the detailed methodology nor the mortality rate was disclosed, limiting its reproducibility [143]. More recently, another methodology was proposed using a pneumatic pico-pump for glioblastoma cell injection, utilising embryos on EDD 6 [136]. That approach yielded viable brain tumours in 25-75% of the experiments, thus providing another transparent option for brain tumour transplantation in chick embryos [136].

The intracerebral tumour inoculation technique that was described and utilised in this thesis, and that was published in Krause et al. [149], reflects a reproducible implantation method inside the developing mesencephalon with transparent disclosure of mortality rates due to the invasive procedure, yielding viable brain tumours in 48%

of the experiments. Thus, the described approach showed a comparable viability to that of Pastorino and colleagues [136]. As no additional equipment such as a pico-pump is needed, the utilised inoculation technique offers a less cost-intensive alternative. Moreover, Pastorino and colleagues utilised embryos in a shorter age span, finalising the experiments on EDD 16 [136], and thus limiting the evaluation of growth and behaviour of implanted tumours. The experiment described in this thesis was carried out for a longer duration (*i.e.*, up until EDD 20), allowing for imaging approaches in larger tumours due to the longer incubation time. Besides, with the use of a non-penetrating micro-syringe, this thesis potentially enhances work safety measures by minimising the risk of accidental self-injury while working with human-derived tumour cell lines.

For the tested brain tumour cell lines U-87 MG and U-87 IDH1^{R132H}, the utilised approach produced highly reproducible solid brain tumours inside the ventricles of the chick tectum infiltrating healthy brain tissue. The growth as well as the interaction of implanted cells with the surrounding developing brain tissue could be realised in a comparable manner to the established *in vivo* rodent implantation methods: In context of host immune reaction, the presence of intermediate filament protein GFAP expression in the vicinity of the brain tumours argues for reactive astrocytes as a response to the induced pathological condition, comparable to that observed in mammals [158–161]. For an intracerebral U-87 IDH1^{R132H} tumour that has split into both tecti of the chick embryo, higher proliferative indices in the regions of infiltrative growth were shown in the right tumour, whereas the centre of the right tumour revealed a region with visibly less Ki-67 positive cells (Figure 12 G). The visibly lower Ki-67 in the core region likely reflects a reduced proliferative capacity due to metabolic stress, hypoxia, and necrotic microenvironment, which might arise not only from limited supply of nutrients and oxygen into the tumour core, but also from perfusion-limited hypoxia and necrosis driving microscopic intravascular thrombosis by neoplastic pro-coagulants overexpression within the tumour [162]. Due to the missing validation of immunofluorescence markers for endothelial cells in avian and the limitation of *ex ovo* methods due to the utilisation of Evans Blue dye, stainings of the tumour neoangiogenesis could not be performed (data not shown). Also, a spatial heterogeneity in proliferation reflects a typical clinical growth pattern of glioma [163].

5.2.2 Feasibility of Intracerebral Tumour Imaging

As a first step, the BBB integrity of the intracerebral glioma has been evaluated. In this context, the formation of an intact BBB in naïve chick embryos has been well-known for an extensive period [164–168]. In this thesis, the BBB was assessed either by MRI after paramagnetic contrast agent administration, or *ex ovo* using Evans blue dye extravasation. As expected, BBB impairment within the area of intracerebral tumour could be detected in later developmental stages of the chick embryo, similar to results observed within established rat models with the same tumour cell line [74]. Interestingly, the *ex ovo* BBB evaluation using Evans blue dye extravasation revealed

a U-87 MG tumour, where no signs of BBB disruption could be observed in the tumour rim region, arguing for an intact blood-tumour barrier; an observation similar to that in non-enhancing gliomas in humans. Preclinically, intact BBBs despite brain tumour are rarely found in rodent brain tumour models, indicating the potential of the intracerebral chick embryo model as advantageous for modelling non-enhancing gliomas, providing important information concerning imaging properties, as for example the evaluation of new radiotracer evaluations modelling gliomas with intact BBB. Nevertheless, this finding of potential BBB variance in the intracerebral glioma chick embryo model highlights the risk of careless radiotracer evaluation: before testing radiotracers with unknown BBB permeability, the BBB integrity of the specific subject has to be evaluated *in ovo*. This implies that an MRI scan with contrast administration must be performed shortly before the scheduled PET measurement to assess the BBB status of the chick embryos. However, this also introduces the risk that the suitable chick embryo might stop developing before the PET scan, due to repeated interruptions of the incubation, for example through the loss of warmth, the administration of anaesthetics at such short time intervals, and repeated intravenous injections. Thus, in studies with BBB independent radiotracers, as the amino acid tracers FET or FDOPA, the BBB integrity status was evaluated *ex ovo* with the Evans blue assay, which represents a more accessible and experiment-friendly approach for routine BBB integrity assessment.

The feasibility of radiotracer evaluation in the intracerebral glioma chick embryo model was tested based on three radiotracers. Due to the extensive clinical and preclinical knowledge of amino acid tracer FET in glioma research, this radiotracer provides ideal conditions for the suitability evaluation of the intracerebral chick embryo model in brain tumour imaging [74, 169, 170, 103, 171–175]. Another amino-acid radiotracer of high relevance for the identification of metabolically active brain tumours is FDOPA [86, 87]. As third evaluated radiotracer, FAPI was chosen due to the known FAP expression in tissue remodelling during embryogenesis and in reactive stromal cells [97], to assess a potential limitation of an embryonic model which does not resemble a mature biological system.

For the comparison with data from rodent models and brain tumour patients, the intracerebral glioma chick embryo model was investigated by small animal PET and subsequent high-resolution *ex ovo* autoradiography. A suitable reference weight has to be investigated to yield similar SUV when comparing species, dependent on the utilised radiotracer as well as the developmental stage of the embryo. Due to the anatomy of the chick embryo, laying inside an albumen filled egg shell with yolk sac and allantois in the outer space of the embryo, a fitting reference weight has to be carefully chosen. The egg shell, albumen, and yolk do not take up the tested radiotracers, whereas excretion products can be delivered to the extra-embryonic allantois. However, the allantois is usually not weighted together with the embryo due to its extra-embryonic position and easy rupture during taking out the embryo. The decision for the correct reference weight thus heavily depends on the tracer kinetics and accumulation in the embryonic tissues: if a tracer is excreted fast and is delivered

into the allantois as extra-embryonic waste storage early after injection, a weight reference including this outer part of the embryo has to be considered. Also, this heavily depends on the age of the embryo on measurement day where significant differences in the size of the embryo and the surrounding egg content can be found. For this thesis' experiments on EDD 18-19, the embryo itself normally fills up the egg completely with only little albumen in the surrounding, while the weight of the remaining yolk sac as well as the egg shell were considered negligible. Comparing the SUV_{brain} of FET in the chick embryo to known SUV in human brains [170] and rat brains [176], SUVs using the weight of the whole egg as reference achieved the best agreement with rodent and human values. Thus, for the experiments with EDD 18-19 embryos and with the tracers FET, FDOPA, and FAPI, the whole egg weight was chosen as suitable reference for SUV calculations. Using the weight of the embryo as a reference resulted in SUVs that were 2.4 times lower.

Before evaluating the radiotracer performances in the intracerebral glioma chick embryo model, the time-activity curve of FET in naïve chick embryos was first assessed to ensure a reliable interpretation of the tracer's performance. A qualitative comparison showed similar results, with decreasing FET uptake after an early peak in most organs, while the brain entities showing SUV in the range of 1, comparable to rodents and humans. The FET whole-body distribution and clearance from the regarded organs of the chick embryo show high similarity to known elimination pathways of rodents and humans. Human dynamic whole-body scans revealed urinary excretion with high FET accumulations in bladder and kidneys [177], while in mice, urinary and pancreatic excretion have been shown [77]. Besides, a notable FET activity was found in human myocardium [177]. The time-activity curves of FET in chick embryos showed the highest FET accumulation in the heart, followed by high liver and kidney uptakes shortly after distribution, indicating a FET clearance through both hepatic and kidney / urinary excretion within the chick embryo on EDD 18-19. However, the possibility of additional pancreatic excretion cannot be excluded due to the close anatomical proximity of liver and pancreas in the chick embryo [112]. Thus, the FET uptake kinetics and excretion pathway have proven to be analogous to established species [178, 173, 170].

Due to the small tumour sizes in the brain and the limited spatial resolution of a small animal PET, scans of the chick embryo are affected by the partial volume effect, limiting a clear delineation of tumours within the rather small developing brain via PET as imaging modality. Hence, brain tumours could be better depicted in high-resolution *ex ovo* autoradiographic approaches. For this, the correlation of PET derived values for the chick embryo brain were compared to the corresponding animal's *ex ovo* autoradiography. Even though only four subjects were utilised in this study, significant correlation of pairs with only minimal deviation were found (Figure 17), resulting in a high degree of congruency between the two method and strengthening the impact of *ex ovo* autoradiographies in its translational relevance.

Thus, the intracerebral glioma chick embryo brain was evaluated based on parameters derived from *ex ovo* autoradiography, qualitatively showing high level of comparability

to FET uptake values in glioma patients with primary brain tumours [170] and xenograft rodent models of the same cell line implanted into the striatum [103] (Table 7), showing high congruency for modelling intracerebral glioma based on FET.

Table 7: Relevant FET parameters in glioma patients with primary brain tumours, orthotopic xenograft rats and orthotopic xenograft chick embryos of the same cell line. All values are given in mean with standard deviation. Abbreviations: SUV: standardised uptake value, TBR: tumour-to-brain ratio, AR: ex vivo autoradiography, n.d.: not determined. Table adapted from [149].

	SUV_{brain}	SUV_{tumour}	TBR_{mean}	TBR_{max}	Sample size	Method
Human [170]	1.06 ± 0.16	2.06	2.02 ± 0.54	2.67 ± 1.07	80	PET
Rat [103]	0.67 ± 0.14	1.42 ± 0.42	2.15 ± 0.37	n.d.	5	AR
Chick embryo [149]	0.80 ± 0.31	1.25 ± 0.35	1.69 ± 0.54	1.92 ± 0.5	5	AR

Experiments with FDOPA demonstrated brain tumours with divergent tracer uptake behaviours despite coming from the same cell line in the same embryo, which is a rather unusual finding (Figure 18). This variability indicates that brain tumour cells might display differing levels of differentiation, as well as showing the tumour's inherited heterogeneity, providing an opportunity to further investigate tumour uptake mechanisms. Clinically, low uptake of amino acid tracers FET or FDOPA is observed in up to 30% of brain tumour patients with Grade 2 oligodendrogliomas and astrocytomas [85], where isometabolic brain tumours tend to have more favourable prognosis [85, 84]. The chick embryo isometabolic tumour showed a lower proliferative index in the infiltration zone than the contralateral hypermetabolic tumour, showing a high resemblance to the clinical situation.

For FAPI, the uptake was also similar to that reported in patients [96]. At the investigated embryonic stage, the FAPI uptake within the brain was as low as in the mouse model [95]. The corresponding PET images showed high uptakes in jaw and spine (data not shown), which was expected due to FAP known for being involved in tissue remodelling in embryogenesis and reactive stromal cells [97]. Even though the whole-body FAPI uptake might thus not resemble a mature model, these differences are not essential for the analysis of brain tumour uptake, where no limitations due to the embryonic origin were found in the regarded developmental stages.

Lastly, the mean TBRs for the three radiotracers can be compared to TBR from glioma patients with primary brain tumours and orthotopic xenograft rats of the same cell line in Table 8, demonstrating strong agreement in achieved values and thus arguing for

the intracerebral glioma chick embryo model as an excellent preclinical model to be considered for tracer evaluation in neuro-oncology.

Table 8: Tumour-to-brain ratios of the radiotracers FET, FDOPA, and FAPI in relation to different species, in mean with standard deviation. Abbreviation: n.d.: not determined. Table taken from [149].

	Mean Tumour-to-Brain Ratio (TBR)		
	Chick Embryo	**Rat**	**Human**
FET	1.69 ± 0.54	2.15 ± 0.37 [103]	2.02 ± 0.54 [170]
FDOPA	1.92 ± 1.11	2.41 up to 3.36 [179]	1.76 ± 0.60 [180]
FAPI	19.13 ± 0.64	n.d.	19.95 ± 13.22 [96]

Considering the two distinct cell lines U-87 MG and U-87 IDH1^{R132H}, no differences in achieved tumour sizes or tracer uptakes could be observed. The expected slower growth of IDH mutated glioma compared to the more aggressive glioblastoma could not be shown in the small sample size. As the mutated IDH glioma is modelled based on a genetically engineered glioblastoma to carry an IDH mutation, the metabolite profile of the U-87 IDH1^{R132H} which is still that of a glioblastoma with other unknown but inherited mutations [27, 28] might limit analyses on differences between the glioma subtypes. For studies focused on glioma subtype deviations, glioma cells with inherent IDH1 mutation would be more suitable. As described before, the modelling of IDH mutated molecular subtypes proves to be more challenging due to the instability of propagation [24, 25]; however, some cell lines that still retain the heterozygous IDH1 mutation are existing, as the oligodendroglioma cell line TS603, that might be utilised in low passages and after rigorous stability testing to ensure validity. Potentially, the modelling of mutated IDH1 glioma can be performed more accurately with inherent mIDH glioma cells despite the known propagation challenges.

Additionally, the versatility of the chick embryo model offers a wide range of applications for multimodal imaging. Advanced MRI methods could assess a number of physiological and molecular parameters, such as the concentration of different metabolites by MR spectroscopy or sodium imaging [147]. However, most of these methods would favour bigger sized tumours, as achievable by CAM implantation, somewhat limiting its translational relevance due to the missing tumour microenvironment depending on the research question.

5.2.3. Limitations of the Intracerebral Glioma Chick Embryo Model

Some limitations that restrict the applicability of the intracerebral glioma chick embryo model need to be addressed. First, the developmental failure rate of 52% after tumour implantation poses a substantial methodological restrain, imposing an excessive operational burden. Also, general dropouts in the second and third week of incubation have been marked even in naïve control embryos, with high variability in-between

cohorts. The overall workflow of the radiotracer experimentation is thus additionally burdened due to the logistical and financial requirements for a chick embryo study, including pre-planning of tracer acquisitions, as well as the coordination of multiple imaging modalities on consecutive days of MRI and PET without previously known sample sizes on final experimentation day.

Further, the implantations of adult-type glioma into an embryonic brain might not resemble the tumour microenvironment of patients. Even though the feasibility in U-87 MG and U-87 IDH1^{R132H} has been demonstrated, extrapolation of these findings to the utilisation of other cell lines must be taken with caution. Especially when studies involve the inoculation of stem cells, the outcome of tumour growth might be different to known preclinical adult models. The embryonic or adult microenvironment might determine the outcome of stem cells due to developmental plasticity and reprogramming of tumours [181]. This has been shown for various tumour types, where a tumorigenic phenotype of teratocarcinoma was completely suppressed in a mouse embryonal environment, while the implantation into an adult mouse led to tumour growth [182]. A similar finding was observed with the Rous Sarcoma Virus, that was not tumorigenic when implanted in EDD 4 chick embryos, whereas implantation in the freshly-hatched chick led to sarcoma formation after a week [183]. However, these results also show adaptions of different tumour cell types based on the surrounding microenvironment, which might be useful for studies involving tumour cells' adaptations for immune evasion and evolved resistances.

Another limitation is the implantation site in the developing mesencephalon of the chick embryo, which varies from the usual striatum implantation in rodent orthotopic tumour research. However, the presence of GFAP expression in the vicinity of the tumour rim region showed high comparability to mammalian experimentation.

Besides, the limited time frame for experimental investigations pose challenges for evaluations of slow-growing tumours, or, in case of drug testing, might exceed the duration of needed administration. Thus, long-term treatment responses might be inadequately represented in the avian model.

A significant limitation arises from the inherent biological distinctions between avian and mammalian immunobiology, particularly creating challenges in studies where antibodies are used for immunohistochemical analysis or when radiotracers depend on host receptor binding. However, if the target binding is confined to the tumour itself, rather than the host, this does not constrain the evaluation of tracer developments or neuroimaging, as the xenograft human originated tumour still retains human physiological properties. Regarding host immunological processes, the extrapolation of findings from the intracerebral glioma chick embryo model to potential applications in mammalian systems might include pitfalls and conclusions must be drawn carefully. Thus, the translational relevance of immunological results obtained in chick embryos may be limited.

5.3 Evaluation of the Neuroblastoma CAM model

5.3.1 Validation of the Neuroblastoma CAM Tumour Inoculation Approach

Compared to LAN-1 CAM tumours, CAM tumours derived from SH-SY5Y cells showed higher mean tumour weights and regular occurring haemorrhagic responses arguing for strong tumour vascularity and angiogenic responses, with visible ruptures leading to extra-vasal blood deposits.

This stronger *in ovo* angiogenic potential for SH-SY5Y tumours grown on the CAM of chick embryos is contradicting existing literature: Ribatti observed that tumours with overexpressed MYCN, tend to induce a greater angiogenic response on the CAM compared to those in which MYCN is not amplified, as SH-SY5Y [65]. However, in their angiogenesis study, the CAM was examined daily until EDD 12, whereas the experiment in this thesis was carried on until EDD 19. Potentially, the angiogenetic effects observed within this experimental time span in a 50x magnified stereomicroscope would yield similar results. Also, the cell line LAN-1, which would belong to the group of amplified MYCN, was not tested in the experiments of Ribatti, possibly yielding other results. Moreover, the subculturing conditions of the SH-SY5Y cell line varied between this thesis and Ribatti's experiments: in this thesis, both morphologically distinct cells, that grew adherently and in suspension, were utilised together for a better depiction of the heterogeneous biology of neuroblastoma [69], whereas in Ribatti and colleagues' study, only the adherent growing cells were collected and used in their CAM experiments [65, 184]. Generally, this culturing variation has been shown to yield different angiogenic profiles, as deviations in the VEGF-A activity in the case of human osteosarcoma cells in monolayer cultivation compared to the culturing in 3D cell culture have been shown [185]. The authors conclude that VEGF-A activity in 3D spheroid culture follow a similar response pattern as found in pro-survival angiogenetic activity in tumours under stress [185]. However, a closer look into angiogenic effects of the cell lines on the chick embryo CAM was beyond the scope of this study and has been extensively studied in the past [129, 65, 116].

5.3.2 Methodological Feasibility of CAM Tumour Imaging

Before starting the evaluation of CAM neuroblastoma tracer uptakes, the general chick embryo methodology of radiotracer studies including PET and AR was systematically examined in this thesis. This is especially of interest due to the comparably higher difficulty of intravenous injections in chick embryo CAM vessels, where pinching or pressure to the injection site to prevent backflow is technically more challenging than in a rodent model. Also, the risk of partly paravasal injections is increased due to this more fluidic injection system.

Winter and colleagues already showed the differences of failed and successful injections of radiotracers in their studies [128]. In their example, the corresponding

chick embryos underwent PET imaging; thus, an example PET image was shown (Figure 34) where the radiotracer, solely accumulating above the embryo below the CAM surface, can be easily recognised. Also, they stated ‘minor’ paravasation in 5 out of 42 analysed chick embryos that were still included for evaluation after rigorous cleansing of the CAM tumours before gamma counter measurement [128]. However, rigorous criteria to reproducibly quantify what constitutes ‘minor’ and at which threshold the results become unreliable are not provided. Even small amounts of paravasal leakage could account for a substantial fraction of the radiotracer activity, depending on the concentration of the injected tracer. Besides, a paravasal bolus in direct contact to a CAM tumour might reveal deviations in radiotracer uptake of this region, *i.e.* through facilitated diffusion rather than modelling an intravenous administration route, limiting its translational value. Also more recent studies state the limitation of injection challenges in radiotracer evaluation studies [144], leading to heavy bleedings when removing the injection cannula. However, the authors did not state how this affected their evaluation of tracer uptakes. Besides, both studies utilised gamma counter measurements for counting the activity distribution in relevant organs and CAM tumours. As the tumour growth kinetics on the CAM strongly vary depending on the utilised cell type, this acquisition might show deviating amounts of integrated CAM tissue between tumour tissue, reducing the reproducibility of the achieved values.

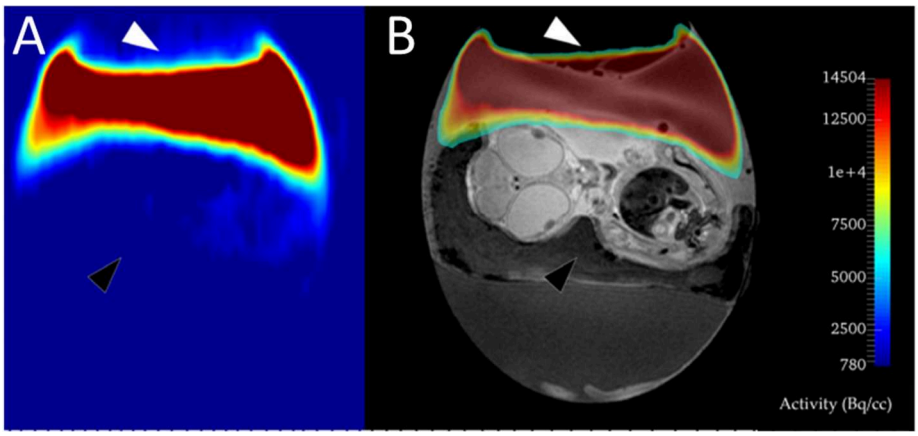

Figure 34: Example of a failed intravenous radiotracer injection in a chick embryo, shown in a PET image (A) and a PET/MR overlay (B). No radiotracer was found inside the embryo (black arrows), whereas the whole tracer activity was found on top of the CAM (white arrows). Image adapted from Winter et al. [128].

Thus, in this thesis, efforts were made to enhance the comparability and experimentation robustness by the evaluation of rigorous measures to ensure a clear and reliable assessment of CAM radiotracer studies.

For a more quantifiable depiction on a correct radiotracer injection in a CAM vessel, the new parameter FID was introduced and suggested in this thesis, based on the injected dose and the recalculated amount of activity based on a gamma counter measurement of the whole embryo after finalisation. Thus, the FID reflects the fraction of radiotracer that stays within the embryo. In this thesis, a significant correlation between CAM tumour radiotracer uptakes and the respective FID could be shown. Generally, in the range of FID fraction of 0.6 to 0.9, the more radiotracer was found in the embryo, the more radiotracer could be taken up by the CAM tumour in the tested

data set, with just one individual with an FID value below 0.6, that showed higher uptake. Thus, for the evaluation of trendlines, this one data point was considered unreliable. In lower FID values, higher tumour uptakes could be expected due to possible diffusion effects instead of the aimed intravenous administration route. For the purpose of setting a mathematical cut-off value, trendlines of different mathematical models were fitted to the dataset and compared. Due to the assumptions of an unreliable upwards trend below a certain threshold and the ideal values at an FID of 1, even numbers of polynomial functions seemed to model the system in the range of 0.4 and 1 the best. It still has to be considered that an overfitting might occur with higher order polynomials. However, the threshold did not vary strongly for all fits. As the data acquisition of the FID score might be different using different gamma counters, the achieved local minima of the trendlines were rounded to one decimal, yielding the set threshold of 0.6 for the tested dataset. However, higher sample sizes as well as values from other operators would be needed for an independent determination of a robust and reliable cut-off value. However, for this significant grouping, all radiotracer uptakes of FET, FDOPA, and FDG were taken together due to the similar outcomes, potentially masking non-significant trends in the low sample sizes. Also, the shown CAM tumours were small-sized and only stored negligible percentages of the injected dose and were thus excluded from the acquisition of the FID due to the extra-embryonic position. However, for bigger sized tumours, this procedure has to be reevaluated as the amount of radiotracer inside the tumour might not remain negligible. Potentially, together with the embryo, the respective CAM tumour has to be included in the acquisition of FID gamma counter measurement for more reliable results.

Intuitively, the recalculated dose inside the embryo would better reflect the amount of correctly injected radiotracer; however, the activity of failed radiotracer injection remains in the egg, especially in CAM region. Hence, the activity of failed injection could possibly reduce the validity of activity values on the CAM. Still, the achieved fraction of injected dose must be further evaluated, with further cut-off thresholds dependent on the distribution of specific radiotracers. Exemplary, for FDG, the naïve CAM study showed twice as high uptake values in this extra-embryonic membrane compared to the experiments of FET and FDOPA. Thus, the fraction will tend to be lower, as the CAM's physiological FDG tracer uptake will naturally decrease the resulting FID. For other radiotracers, faster wash-out and extra-embryonal storage in the allantois might occur, reducing the meaningfulness of FID as injection control. Thus, before new radiotracers can be evaluated in the chick embryo model, time-activity curves in naïve chick embryos of the respective radiotracers need to be utilised for a clear depiction of radiotracer distribution in the embryonal model. Potentially, each new radiotracer may require its own FID threshold. The fact that all three tested radiotracers showed the same embryonal uptakes and thus yielded a summarised threshold in this study might be coincidental.

5.3.3 Evaluation of Radiotracer Dosimetry and its Translational Validity

In the following, the TACs of the utilised radiotracers were compared to the known dosimetry in human.

For the comparison of FET, please refer to Chapter 5.2.2, where the TAC was discussed for the validity of radiotracer performance in the intracerebral tumour model.

For FDOPA, the TAC in the chick embryo model revealed the highest SUV in the kidneys, with increasing uptake after a short minimum at approximately five minutes post-injection. Generally, heart and liver show near same SUV with a plateau ten minutes after injection. The uptake within the brain was moderate and constant for the considered time. Compared to this, the physiological TAC of FDOPA in human demonstrate high uptake in liver, pancreas, and the excretory organs gallbladder, kidney, urinary bladder; with variations in the individual elimination timing [186]. The high excretory organ uptake in the chick embryo kidneys and liver argue for high similarity to the human physiological FDOPA uptake.

The TAC of FDG in relevant organs of the chick embryo revealed constant high SUV in kidneys, nearly identical values in heart and liver, and an accumulation of brain uptake. Also, high inter-subject variances occurred in the chick embryo model. Compared to human TAC of FDG in the regarded time of 30 minutes, increasing SUV for the brain are also observed. Qualitatively, the highest uptake in human is the heart with an increasing uptake curve, followed by kidney and liver with similar SUV in a decreasing uptake trend over the considered time [187]. Also, near constant SUV of 2 in the human stomach can be found [187]. These differences and inter-subject variances in FDG uptake are likely attributable to intrinsic biological heterogeneity, with strongly varying embryonal developmental stages, as shown in the underdeveloped embryo in Figure 26. Thus, a metabolically deviating embryonal state with differing glucose needs in the developing organs seems likely. The nearly identical values of heart and liver might be due to the close proximity and difficulty to deviate in the chick embryo with possibly signals of the stomach as well as other organs, complicating the systemically placing of VOIs of similar uptake. An interesting finding was the observed wash-out of FDG in the chick embryo heart, which is classically assumed unlikely due to the effective trapping of FDG-6-phosphate in heart tissues due to high influx via GLUT1 but no possibility of wash-out due to low concentration of glucose-6-phosphate for the needed dephosphorylation. While this finding holds true for adult brain and heart myocardium due to the high glycolytic activity and low concentration of glucose-6-phosphate, the shown chick embryo heart TAC indicates a deviating glucose metabolism in the avian embryonic heart. Coffey and colleagues already showed strong evidence that the chick embryo heart utilises glucose differently, dominantly over the phosphogluconate pathway which turns minor in adult chick hearts [188]. Another study performed by Kutchai and colleagues argues that the chick embryo glucose transport system of the heart might be more specific compared to rat hearts or humans, as inhibition of glucose uptake in ways suitable for rat hearts and humans could not be reproduced in the chick embryo [189], indicating a deviating heart glucose metabolism. These findings suggest that the chick embryo heart has a developmentally altered glucose metabolism, that is not following the classical FDG myocardium trapping.

For PET derived CAM tumour studies, the static and dynamic uptake of the evaluated radiotracers in the naïve CAM of same EDDs as the CAM tumour studies were assessed. This revealed both static deviations, with 2-fold higher uptake values for FDG compared to similar values in FET and FDOPA, as well as dynamic differences: while FDOPA and FDG exhibited relatively constant CAM uptake in the regarded time, the FET uptake increased in the regarded first half-hour post-injection. Additionally, the uptake of the naïve CAM showed high inter-subject variability. Thus, the simple statement of tracer uptakes of CAM tumours without CAM background subtraction proves to be insufficient for providing a fitting comparison in tumorous uptakes of the regarded radiotracers. Warnock and colleagues stated the challenge of clear background region identification due to the inconsistent positioning of the tumour to the position of the embryo [125]. This pitfall has also been found in this thesis, as shown in Figure 26. Still, the utilisation of chick embryos of EDD 18 to 19 normally show regions of CAM tissue without close contact to the embryo, that were considered as CAM background tissue individually for each chick embryo in the here presented study.

Besides, the correct VOI placement in PET-derived images proves challenging in smaller sized CAM tumours for the clear depiction of injection zone, paravenous residues, and real CAM tumour uptakes. Thus, naïve chick embryo PET imaging with the utilised radiotracers revealed the tracer kinetics of the injection zone as well as paravenous regions: The corresponding TAC curves of VOIs placed inside these regions showed fast wash-out for all three radiotracers. Together with unphysiologically high start SUV directly after the injection, the kinetics can be used to better characterise the observed VOI in PET imaging. Additional anatomical imaging would simplify the VOI region placement into the CAM tumour. CT imaging after PET acquisition has been shown to be feasible for delineating bigger-sized tumours on the CAM [125]; however, only the CAM surface and the eggshell can be visualised as reference structures, and smaller tumours might not be detected. Thus, the physical orientation of the chick embryo is not apparent in CT without previous CT contrast agents [125]. MR imaging on the day before PET would show the localisation of the CAM tumour in relation to the orientation of the embryo in sufficient manner for third-week embryonal stages, as the embryo does not change its orientation drastically once it fills up the eggshell. However, consecutive days of imaging poses potential chick embryo viability risks due to temperature deviations during the measurement as well as the additional need for narcotics.

As discussed in Chapter 5.2.2, the weight of the whole egg as reference weight for the calculations of SUV was chosen in this study, as well. However, a severe pitfall has been shown in Figure 26 with an underdeveloped embryo, yielding an overestimation of SUV, as high percentages of the egg weight might be albumen with no radiotracer uptake for the regarded radiotracers FET, FDG, and FDOPA. Additionally, the weight of the embryonal egg decreases physiologically during incubation due to water loss through evaporation, limiting the meaningfulness of the egg weight when varying embryonal stages are regarded. Especially in CAM studies, the developmental status of the embryo itself is currently insufficiently investigated due to the extra-embryonic

position of the CAM tumour as region of interest. Warnock and colleagues suggested in their outlook the possibility of an additional CT scan, to measure the egg volume or beak length, to better estimate the embryonal weight [125]. Also, the authors assume a direct relation between FDG blood plasma kinetics to injected dose and body weight [125]. When comparing SUV parameters based on the embryo instead of the whole egg weight, values 2.4 times lower have to be considered on EDD 18-19 for normally developing embryos. For the shown radiotracers FET, FDG, and FDOPA, the whole egg as reference yielded the highest similarity to values measured in patients and rodents. However, this might not reflect the reality and has to be reconsidered in the future. Thus, the SUV was only utilised for the direct comparison of tracer uptakes to other species. For all other evaluations, the tracer uptakes were better evaluated in activity per volume (kBq/ccm).

Another methodological evaluation was the correlation of PET derived and *ex ovo* AR derived SUV, as the small-sized CAM tumour evaluation based on PET led to partial-volume effects, with uptake over- and underestimations based on the orientation, size and location of the CAM tumour in relation to the embryo. For the tested neuroblastoma CAM tumours, a significant effective pairing has been validated; however, also a significant bias could be shown. The achieved radiotracer uptake values derived from PET and by phosphor imaging plates are not cross-validated. More detailed evaluation on the systematic bias revealed significantly higher SUV based on *ex ovo* AR compared to the PET counterpart in all tested subjects. The analysis of radiotracer dependency on the correlation showed significantly differences based on the utilised radiotracer, with more pronounced differences in AR and PET values for FDG, whereas similar deviations occurred for FET and FDOPA (Figure 28). Potentially, the higher background CAM values for FDG led to a signal wash out for the CAM tumour, aggravated by the background subtraction in the VOI uptake calculations.

5.3.4 Validation of Neuroblastoma CAM Tumour Approach based on FDG and FDOPA

This study aimed at evaluating radiotracer uptakes on high-risk neuroblastoma within the CAM model. Gold standard in clinical practice for detecting primary and metastatic lesions remains a scintigraphy with [^{123}I]MIBG [41]; still, whenever MIBG is not available or neuroblastoma tumours fail to accumulate MIBG, suitable alternatives have been found, with PET using FDG [44, 43, 190] or FDOPA [190, 91, 90, 92]. Thus, the evaluation of the CAM neuroblastoma approach for those established radiotracers shall be tested for its validity.

The achieved neuroblastoma tumour uptake values of FDG and FDOPA can be qualitatively compared to neuroblastoma patients as test of translational validity of the chick embryo neuroblastoma CAM study. For this, the tumour SUV values based on AR can be compared to the patient situation based on Liu and colleagues' findings [190] (Table 9). The chick embryo findings can only be qualitatively compared on a

percentage basis, acknowledging that the patient study comprised 42 neuroblastoma patients reported as median and interquartile range [190], while the chick embryo results are based on two human-derived cell lines. The chick embryo SUV values are based on recalculated SUV_{tumour} from *ex ovo* autoradiography, with the whole egg weight as reference. Overall, the radiotracer performances showed similar values with the same order of magnitude when both cell lines were combined (n = 6 per tracer). As shown with the systematic bias in the AR-PET correlation, PET derived SUVs would show lower values. Next, the tumour uptakes based on grouping of MYCN status can be qualitatively compared. The cell line LAN-1 is MYCN amplified, whereas the SH-SY5Y cell line does not show MYCN amplification. Again, all chick embryo derived SUV_{tumour} values were within the same order of magnitude compared to the patient derived counterpart, but moderately higher than usually found in human. Considering the MYCN status in patients, statistically significant differences between non-amplified and amplified SUV medians were reported for FDG ($p = 0.0067$) [190], with 1.8 times higher SUV_{tumour} for MYCN amplified neuroblastoma. For chick embryos carrying either non-amplified MYCN neuroblastoma (SH-SY5Y) or amplified MYCN neuroblastoma (LAN-1), a similar trend for FDG could be observed, with 1.7 times higher SUV for the amplified MYCN cell line. For FDOPA, the patients with non-amplified MYCN tumours showed a 1.1-fold higher SUV_{tumour} median than the amplified counterpart. This relative difference in the chick embryo was higher with 1.4-fold higher SUV_{tumour} in non-amplified MYCN tumours. Thus, even though all chick embryo derived values were moderately higher than the human uptake values, the relative differences revealed comparable results in both species, indicating the chick embryo neuroblastoma CAM model as a valuable model for tumour uptake assessment.

Table 9: Comparison of neuroblastoma tumour uptake for FDG and FDOPA of patients based on Liu et al. [190] to the chick embryo CAM results based on ex ovo autoradiography. All human values are given as median (interquartile range) and as mean for chick embryos.

Characteristics		**Species**	**SUV_{tumour}**	
			FDG	**FDOPA**
overall radiotracer uptakes		Human [190]	4.07 (2.76-6.36)	3.54 (2.79-5.03)
		Chick embryo	6.29	4.07
MYCN status	**non-amplified**	Human [190]	3.79 (2.64-5.11)	3.59 (2.95-5.30)
		Chick embryo	4.55	4.69
	amplified	Human [190]	6.85 (5.64-8.17)	3.24 (2.04-3.66)
		Chick embryo	7.64	3.44

5.3.5 Evaluation of FET as new Radiotracer for Neuroblastoma based on the CAM tumour model

As the CAM tumour approach showed high resemblance to the patient radiotracer uptake performance, the radiotracer FET that is established as brain tumour marker, was tested in this study for its validity in neuroblastoma. To the best of our knowledge, FET has never been tested as potential alternative. Several uptake pathways have been described for FET, from LAT1 and LAT2 to sodium dependent uptakes via system B^{0+} [78]. The uptake mechanism of FET remains to be further investigated in the future [81]. FDOPA is also mainly transported by the LAT1 transporter [86], while also serving as a substrate of catechol O-methyl transferase and aromatic amino acid decarboxylase, providing additional value as a diagnostic tool for functionally identifying tumours with elevated catecholamine metabolism [90, 92, 91, 41]. Thus, the comparison of FET uptake in high-risk neuroblastoma to the established radiotracers FDOPA and FDG might reveal another valuable alternative. In this study, the cell line LAN-1 was utilised as an example of a cell line lacking MIBG uptake, while harbouring ALK-mutation and MYCN amplification. As counterpart, SH-SY5Y was utilised as MYCN non-amplified cell line while harbouring the same ALK mutation.

Based on CAM tumour PET, overall low deviations in SUV_{mean} and SUV_{max} were observed for FET, FDG, and FDOPA (Figure 29). Also, FDG and FET showed low variability in the uptake, with almost no difference in the utilised cell lines. In contrast, a high deviation for FDOPA was observed, with higher tumour uptakes for the SH-SY5Y compared with the LAN-1 tumour. The expression of tyrosine hydroxylase and dopamine-β-hydroxylase in SH-SY5Y cells with neuroblast-like morphology show characteristics of catecholaminergic neurons [69], indicating functional activity of the catecholaminergic pathway while promoting FDOPA uptake and metabolism. The dynamic TACs of the individual CAM tumours reflect the overall higher uptake for FDOPA by SH-SY5Y cells, whereas most of the other subjects showed near constant uptake values around 200 kBq/ccm. However, as stated in Chapter 5.3.2, the surrounding uptake values in small-sized CAM tumours might hinder a reliable uptake assessment. The curves mainly show constant uptake without major retention, with small peaks for single time points, as exemplary seen in the FDG LAN-1 curve at 32 minutes post-injection (Figure 30). One possible reason is the inability to monitor the depth of anaesthesia in chick embryo imaging over time. While in animal experiments physiological parameters such as the body temperature and respiration rate are commonly monitored to prevent motion artefacts, this is only feasible to a limited extent in the embryo, as specialised equipment would be necessary. Movements at these embryonal developmental stages, where the embryo is filling up the egg, would have a direct impact, resulting in a short-time elevation and depression of the CAM level in specific regions of limb movements or head inclinations. However, the sample size with one tumour per group and radiotracer in PET limits the meaningfulness of the results. Hence, three embryos were utilised per group for the *ex ovo* autoradiographic evaluation, still yielding neither significant differences in the utilised radiotracer, nor in the utilised cell line, arguing for FET as a potential candidate for more detailed

examination in neuroblastoma uptake performance. For this, future studies would benefit from larger sample sizes and the inclusion of additional cell lines representing ALK non-mutated high-risk neuroblastoma. Also, for a more established model and final validation before proposing testing FET for high-risk neuroblastoma patients, a study with rodent xenograft neuroblastoma could be beneficial as further validation step of the achieved positive FET uptake.

5.3.6 Limitations of the Chick Embryo Neuroblastoma CAM Model

Some limitations of the chick embryo neuroblastoma CAM tumour model need to be addressed.

Firstly, as discussed in Chapter 5.3.2, the methodology of CAM tumour imaging based on radiotracer imaging modalities, as PET and AR, has to be carefully and critically examined for reliable results in CAM radiotracer studies. The introduction of the new proposed parameter FID shall enhance the comparability and robustness of these more complex imaging modalities; however, depending on the operator of the radiotracer injections, high dropout rates based on FID threshold might occur in cases of partly correct injections in the CAM tumour model. Thus, these studies might lack animal reduction aspects of the 3Rs for possibly enhancing reliability of achieved radiotracer tumour uptake assessments.

In addition, a main focus of neuroblastoma research lies in the investigation of the innate and adaptive immune system, particularly focusing on the tumour immune evasion mechanisms and the development of immune-based therapeutic strategies, as the utilisation of GD2 antibodies. However, the chick embryo neuroblastoma CAM model is limited in this context due to the absence of a fully developed immune system, restricting the investigation of immune-mediated mechanisms. Also, the immune system of the avian shows inherent differences to mammalian systems, such as a simplified major histocompatibility complex [191] or differences in the immunoglobulin classes [109], limiting the translational relevance of immune-based studies. Thus, in the field of neuroblastoma, studies have to be carefully evaluated to determine whether there is a meaningful benefit from the utilisation of the chick embryo CAM model.

The utilisation of heterogeneous human xenografts in the CAM model also introduces significant sources of variability that go beyond the intrinsic limitations of an embryonic host: The utilised neuroblastoma cell lines compromise heterogeneous subpopulations with stem-like or progenitor cells, which can dynamically alter their proliferation, differentiation, or angiogenic behaviour in response to their microenvironment. As the chick embryo develops, several physiological parameters, as the blood pH, the concentration of bicarbonate ions or the partial pressure of CO_2 and O_2 from the blood change continuously [192], which might influence the growth milieu and thus influence the tumour growth and cellular behaviour dynamically. Consequently, these changes driven both by stem-like cell plasticity and the avian embryonic physiology pose challenges in robustness and reproducibility and highlight the need for rigorous tumour cell characterisation and adequate sample sizes to account for inter-embryo variability.

6 Outlook and Conclusions

Further studies in the chick embryo model would highly profit from higher sample sizes to account for inter-embryo variability and ensure significant results.

In the field of orthotopic glioma xenografts, models that mimic mIDH glioma still need to be established. The utilisation of genetically modified glioblastoma cell lines might not resemble the tumour characteristics of this glioma subtype. Although unstable in long-term cell culture, mIDH glioma cell lines derived from astrocytoma or oligodendroglioma patients, as the cell lines BT142mut/- or TS603, could be implanted at young passages after rigorous stability testing for a better reflection of patient situation in those tumour types. Also, the implantation of patient biopsies into the brain of the chick embryo would yield a better reflection and should be considered in the future.

In neuroblastoma research, the radiotracer studies would benefit from the expansion to more neuroblastoma cell lines. Both utilised neuroblastoma cell lines are ALK mutated, a rather rare genetic component in high-risk neuroblastoma. ALK wildtype cell lines as SK-N-AS would improve the meaningfulness of radiotracer evaluations. Also, orthotopic implantations would better reflect the physiological tumour occurrence and might be considered. Further, the results from chick embryo radiotracer uptake studies shall be validated in mice to further strengthen the impact and examine the validity of chick embryo derived values.

Aim of this study was to establish, characterise and analyse neuro-oncological tumour models in the chick embryo for the feasibility and translational relevance in comparison to established models or patients.

Thus, now, the questions addressed in the aim of the study can be answered:

1. Can intracerebral gliomas in the chick embryo model be successfully modelled and visualised using autoradiography with different PET radiotracers?

Yes, the intracerebral tumour growth could be confirmed histologically, and the evaluated radiotracers showed robust tumour uptakes relative to the surrounding chick embryo brain tissue on the autoradiographs. This demonstrated the feasibility of intracerebral gliomas modelling in the chick embryo, while preserving the visualisation of PET radiotracers in autoradiographs identical to the methods established in rodents. Still, substantial methodological, logistical, and financial restrains are posed by high developmental failure rates of 52%.

2. How do radiotracer uptake and kinetics in the chick embryo model compare to those observed in rodent models and patients?

The radiotracer uptakes and kinetics in the chick embryo showed high comparability to rodent models as well as clinical observations. Especially, the occurrence of an isometabolic tumour, as observed in the FDOPA experiment through a TBR near 1,

argue for a reflection of the patient situation in non-enhancing mIDH gliomas of lower WHO grades.

3. Is the neuroblastoma CAM model suitable for reproducible radiotracer evaluations? Are there possible refinements to increase the robustness of CAM radiotracer studies?

Yes, it is possible to evaluate radiotracers in the neuroblastoma CAM model; however, more methodological aspects have to be considered compared to the rodent experiment setup. This includes a rigorous surveillance of the incorporation of radiotracer in the embryo for ensuring a functional intravenous application, as para-vasal radiotracer might come into close contact to the tumour leading to potentially differing administration routes, lowering the reproducibility and robustness of the experiments. For this purpose, a new parameter, the fraction of injected dose (FID) was suggested that shall offer a possibility to evaluate of the amount of correctly applied i.v. radiotracer for radiotracers known to accumulate in the embryo. A significant positive correlation of the FID and the corresponding radiotracer uptake in the CAM tumour could be found, leading to a cut-off value of experiments with FID below 0.6, and emphasising the need of additional considered parameters to ensure validity and reproducibility of neuroblastoma CAM radiotracer evaluations.

4. How do the radiotracer uptakes derived from CAM neuroblastoma perform compared to the achieved values in neuroblastoma patients?

With the whole egg as reference weight, the neuroblastoma grown on the CAM showed slightly higher SUV than the SUV in neuroblastoma patients, but still within the same order of magnitude. When grouping the results based on characteristics as the MYCN status, the relative differences occurring in neuroblastoma patients were very well reflected in the CAM neuroblastoma model for the clinically established radiotracers. Still, the sample size would have to be increased for reliable quantitative translational comparison.

5. How does the radiotracer FET compare in respect to its neuroblastoma uptake to the clinically established radiotracers FDG and FDOPA in the chick embryo model?

No statistically significant differences in the uptake of FET compared to the clinically established radiotracers FDG or FDOPA could be found. However, an increase in sample sizes, the expansion to more neuroblastoma cell lines, as well as the validation of achieved results in more established preclinical models are needed to support and strengthen the findings before conclusions can be drawn. In case the results can be confirmed, experiments in xenograft neuroblastoma rodent models could be performed before proposing for clinical testing. This would also further validate the CAM neuroblastoma chick embryo approach.

6. In which aspects might the chick embryo model be considered an alternative to rodent models and what are its limitations?

Based on the results of the intracerebral glioma chick embryo model and the neuroblastoma CAM model, several tested parameters showed high resemblance to those from rodent models or patients. However, the experiments need to be expanded on other cell lines and tracers; and the reproducibility needs to be tested in other laboratories for validation. With today's knowledge, the shown chick embryo models might be good intermediate models between *in vitro* tests and rodent *in vivo* studies, bridging more realistic rapid screening before rodent experiments. An important limitation is the developmental failure rates that pose substantial methodological and logistical restrains while limiting the ethical animal reduction aspect. Also, the limited time frame for experimental investigations pose challenges for slow-growing tumours or might exceed the duration of needed administration for drug testing. Still, the chick embryo provides a suitable model for initial assessment of new radiotracers. A significant limitation arises from the inherent difference of avian and mammalian immunobiology, as well as the differences between embryonal and adult models.

Declaration on the Use of Manuscripts in the Doctoral Thesis

In the present doctoral thesis, manuscripts to which the doctoral researcher is an author and to which a substantial contribution have been made are included in accordance with Doctoral Degree Regulations of Math.-Nat. Faculty, Official Announcement No.24/2018 of HHU, §6 (3). The manuscripts were incorporated in an adapted form.

Manuscript 1:

Authors:	Chang-Hoon Choi, Maximilian Bruch, Suk-Min Hong, **Sandra Krause**, Carina Stegmayr, Stefan Schwan, Wieland Alexander Worthoff, Jörg Felder, N. Jon Shah
Title:	"A modified quadrature birdcage coil incorporated with a curved feature for in ovo MR imaging"
Journal:	IEEE Open Journal of Engineering in Medicine and Biology
Year:	2024
DOI:	doi: 10.1109/OJEMB.2024.3420231

Specific Contributions of the Doctoral Researcher

- Planning and execution of chick embryo experiments
- Contribution to Fig. 6 (identification of relevant anatomical regions)
- Manuscript revision

Identification of adapted content based on this manuscript:

Parts of Chapter 4.1 were adapted from this publication.

Confirmation by Supervisor:

I hereby confirm that, to the best of my knowledge, the information provided above regarding the doctoral researcher's contribution to the manuscript is accurate and credible.

Jülich 8.1.26
Place, Date

Signature

Manuscript 2:

Authors: **Sandra Krause**, Alexandru Florea, Chang-Hoon Choi, Wieland Alexander Worthoff, Alexander Heinzel, Saskia Fischer, Nicole Burda, Bernd Neumaier, N. Jon Shah, Philipp Lohmann, Felix M. Mottaghy, Karl-Josef Langen, Carina Stegmayr

Title: "Autoradiography of Intracerebral Tumours in the Chick Embryo Model: A Feasibility Study Using Different PET Tracers"

Journal: Molecular Imaging and Biology

Year: 2025

DOI: https://doi.org/10.1007/s11307-025-01983-9

Specific Contributions of the Doctoral Researcher

- Planning and execution of FDOPA experiment
- Image analysis and interpretation of FDOPA and FET experiments
- Figure preparations: Fig. 5, 6; Supplementary Fig. 2, 3, 4
- Contributions to Fig. 2, 3, 4 (about 10-20% each)
- Generation of Tab. 1, 2; Supplementary Tab. 1
- Writing of initial manuscript
- Discussion and contextualisation of the findings
- Coordination and implementation of revisions suggested by the co-authors
- Handling and coordination of manuscript submission and resubmission process, including response drafts to the peer-reviewers and implementation of revisions

Identification of adapted Content based on this manuscript:

Parts of Chapter 4.2 and 5.2 were adapted from this publication.

Confirmation by Supervisor:

I hereby confirm that, to the best of my knowledge, the information provided above regarding the doctoral researcher's contribution to the manuscript is accurate and credible.

Jülich 8.1.26
Place, Date

Signature

References

1. Weller M, van den Bent M, Preusser M et al. (2021) EANO guidelines on the diagnosis and treatment of diffuse gliomas of adulthood. Nat Rev Clin Oncol 18:170–186. https://doi.org/10.1038/s41571-020-00447-z
2. Dai C, Holland EC (2001) Glioma models. Minireview. Biochimica et Biophysica Acta:M19-M27
3. Louis DN, Perry A, Wesseling P et al. (2021) The 2021 WHO Classification of Tumors of the Central Nervous System: a summary. Neuro Oncol 23:1231–1251. https://doi.org/10.1093/neuonc/noab106
4. Yan J, Parsons DW, Jin G et al. (2009) IDH1 and IDH2 Mutations in Gliomas. The New England Journal of Medicine 360:765–773
5. Neumaier F, Zlatopolskiy BD, Neumaier B (2023) Mutated Isocitrate Dehydrogenase (mIDH) as Target for PET Imaging in Gliomas. Molecules 28. https://doi.org/10.3390/molecules28072890
6. Alshiekh Nasany R, La Fuente MI de (2023) Therapies for IDH-Mutant Gliomas. Curr Neurol Neurosci Rep 23:225–233. https://doi.org/10.1007/s11910-023-01265-3
7. Ostrom QT, Cioffi G, Gittleman H et al. (2019) CBTRUS Statistical Report: Primary Brain and Other Central Nervous System Tumors Diagnosed in the United States in 2012-2016. Neuro Oncol 21:v1-v100. https://doi.org/10.1093/neuonc/noz150
8. Lohmann P, Schäfer L, Krause S et al. (2025) Advancements in noninvasive visualization of the immune environment in glioblastoma: A systematic review. Neurooncol Adv 7:vdaf176. https://doi.org/10.1093/noajnl/vdaf176
9. Wen PY, Weller M, Lee EQ et al. (2020) Glioblastoma in adults: a Society for Neuro-Oncology (SNO) and European Society of Neuro-Oncology (EANO) consensus review on current management and future directions. Neuro Oncol 22:1073–1113. https://doi.org/10.1093/neuonc/noaa106
10. Banks WA (2016) From blood-brain barrier to blood-brain interface: new opportunities for CNS drug delivery. Nat Rev Drug Discov 15:275–292. https://doi.org/10.1038/nrd.2015.21
11. Aldape K, Brindle KM, Chesler L et al. (2019) Challenges to curing primary brain tumours. Nat Rev Clin Oncol 16:509–520. https://doi.org/10.1038/s41571-019-0177-5
12. Abbott NJ (2005) Dynamics of CNS barriers: evolution, differentiation, and modulation. Cell Mol Neurobiol 25:5–23. https://doi.org/10.1007/s10571-004-1374-y
13. Abbott NJ, Patabendige AAK, Dolman DEM et al. (2010) Structure and function of the blood-brain barrier. Neurobiol Dis 37:13–25. https://doi.org/10.1016/j.nbd.2009.07.030
14. Li X, Li L, Zhou K et al. (2022) Glioma Shapes Blood-Brain Barrier Integrity and Remodels the Tumor Microenvironment: Links with Clinical Features and Prognosis. J Clin Med 11. https://doi.org/10.3390/jcm11195863

15. Arvanitis CD, Ferraro GB, Jain RK (2020) The blood-brain barrier and blood-tumour barrier in brain tumours and metastases. Nat Rev Cancer 20:26–41. https://doi.org/10.1038/s41568-019-0205-x
16. Langen K-J, Galldiks N (2016) PET Imaging of Brain Tumors: in Medical Radiology. Diagnostic Imaging. Springer Berlin Heidelberg, Heidelberg
17. Bergström M, Collins VP, Ehrin E et al. (1983) Discrepancies in Brain Tumor Extent as Shown by Computed Tomography and Positron Emission Tomography Using [68Ga]EDTA, [11C]Glucose, and [11C]Methionine. Journal of Computer Assisted Tomography:1062–1066
18. Galldiks N, Lohmann P, Friedrich M et al. (2024) PET imaging of gliomas: Status quo and quo vadis? Neuro Oncol 26:S185-S198. https://doi.org/10.1093/neuonc/noae078
19. Pontén J, Macintyre EH (1968) Long term culture of normal and neoplastic human glia. Acta Pathol. Microbiol. Scand. 74:465–486
20. Allen M, Bjerke M, Edlund H et al. (2016) Origin of the U87MG glioma cell line: Good news and bad news. Sci Transl Med 8:354re3. https://doi.org/10.1126/scitranslmed.aaf6853
21. Clark MJ, Homer N, O'Connor BD et al. (2010) U87MG decoded: the genomic sequence of a cytogenetically aberrant human cancer cell line. PLoS Genet 6:e1000832. https://doi.org/10.1371/journal.pgen.1000832
22. Fogh J, Fogh JM, Orfeo T (1977) One Hundread and Twenty-Seven Cultured Human Tumor Cell Lines Producing Tumors in Nude Mice. Journal of the National Cancer Institute:221–226
23. Brehar FM, Ciurea AV, Chivu M et al. (2008) The development of xenograft glioblastoma implants in nude mice brain. Journal of Medicine and Life 1
24. Piaskowski S, Bienkowski M, Stoczynska-Fidelus E et al. (2011) Glioma cells showing IDH1 mutation cannot be propagated in standard cell culture conditions. Br J Cancer 104:968–970. https://doi.org/10.1038/bjc.2011.27
25. Luchman HA, Chesnelong C, Cairncross JG et al. (2013) Spontaneous loss of heterozygosity leading to homozygous R132H in a patient-derived IDH1 mutant cell line. Neuro Oncol 15:979–980. https://doi.org/10.1093/neuonc/not064
26. Kim W, Liau LM (2012) IDH mutations in human glioma. Neurosurg Clin N Am 23:471–480. https://doi.org/10.1016/j.nec.2012.04.009
27. Izquierdo-Garcia J, Viswanath P, Eriksson P et al. (2015) Metabolic reprogramming in mutant IDH1 glioma cells. PLOS ONE 10. https://doi.org/10.1371/journal.pone.0118781
28. Molloy AR, Najac C, Viswanath P et al. (2020) MR-detectable metabolic biomarkers of response to mutant IDH inhibition in low-grade glioma. Theranostics 10:8757–8770. https://doi.org/10.7150/thno.47317
29. Wen Z, Zhang L, Zhuang H (2020) Roles of PET/Computed Tomography in the Evaluation of Neuroblastoma. PET Clin 15:321–331. https://doi.org/10.1016/j.cpet.2020.03.003
30. Kaatsch P, Grabow D, Spix C (2016) German Childhood Cancer Registry: Annual Report 2016 (1980-2015)

31. Park JR, Bagatell R, London WB et al. (2013) Children's Oncology Group's 2013 blueprint for research: neuroblastoma. Pediatr Blood Cancer 60:985–993. https://doi.org/10.1002/pbc.24433
32. Qiu B, Matthay KK (2022) Advancing therapy for neuroblastoma. Nat Rev Clin Oncol 19:515–533. https://doi.org/10.1038/s41571-022-00643-z
33. Chaudhury A (1971) Regression of Neuroblastoma during Pregnancy. The Lancet 298:1041–1042
34. DuBois S, Kalika Y, Lukens JN et al. (1999) Metastatic Sites in Stage IV and IVS Neuroblastoma Correlate With Age, Tumor Biology, and Survival. Journal of Pediatric Hematology/Oncology 21:181–189
35. Monclair T, Brodeur GM, Ambros PF et al. (2009) The International Neuroblastoma Risk Group (INRG) staging system: an INRG Task Force report. J Clin Oncol 27:298–303. https://doi.org/10.1200/JCO.2008.16.6876
36. Cohn SL, Pearson ADJ, London WB et al. (2009) The International Neuroblastoma Risk Group (INRG) classification system: an INRG Task Force report. J Clin Oncol 27:289–297. https://doi.org/10.1200/JCO.2008.16.6785
37. Sokol E, Desai AV (2019) The Evolution of Risk Classification for Neuroblastoma. Children (Basel) 6. https://doi.org/10.3390/children6020027
38. Huang M, Weiss WA (2013) Neuroblastoma and MYCN. Cold Spring Harb Perspect Med 3:a014415. https://doi.org/10.1101/cshperspect.a014415
39. Brodeur GM, Seeger RC, Schwab M et al. (1984) Amplification of N-myc in Untreated Human Neuroblastomas Correlates with Advanced Disease Stage. Science 224
40. Seeger RC, Brodeur GM, Sather H et al. (1985) Association of Multiple Copies of the N-myc Oncogene with Rapid Progression in Neuroblastomas. The New England Journal of Medicine 313
41. Bar-Sever Z, Biassoni L, Shulkin B et al. (2018) Guidelines on nuclear medicine imaging in neuroblastoma. Eur J Nucl Med Mol Imaging 45:2009–2024. https://doi.org/10.1007/s00259-018-4070-8
42. Vallabhajosula S, Nikolopoulou A (2011) Radioiodinated metaiodobenzylguanidine (MIBG): radiochemistry, biology, and pharmacology. Semin Nucl Med 41:324–333. https://doi.org/10.1053/j.semnuclmed.2011.05.003
43. Sharp SE, Shulkin BL, Gelfand MJ et al. (2009) 123I-MIBG scintigraphy and 18F-FDG PET in neuroblastoma. J Nucl Med 50:1237–1243. https://doi.org/10.2967/jnumed.108.060467
44. Hu R, Zhang Y, Liu S et al. (2023) Prognostic prediction by 18F-FDG-PET/CT parameters in patients with neuroblastoma: a systematic review and meta-analysis. Front Oncol 13:1208531. https://doi.org/10.3389/fonc.2023.1208531
45. Paret C, Ustjanzew A, Ersali S et al. (2022) GD2 Expression in Medulloblastoma and Neuroblastoma for Personalized Immunotherapy: A Matter of Subtype. Cancers (Basel) 14. https://doi.org/10.3390/cancers14246051
46. Fredman P, Hedberg K, Brezicka T (2003) Gangliosides as Therapeutic Targets for Cancer Biodrugs:155–167

47. Anderson J, Majzner RG, Sondel PM (2022) Immunotherapy of Neuroblastoma: Facts and Hopes. Clin Cancer Res 28:3196–3206. https://doi.org/10.1158/1078-0432.CCR-21-1356
48. Schmitt J, Schwenck J, Maurer A et al. (2022) Translational immunoPET imaging using a radiolabeled GD2-specific antibody in neuroblastoma. Theranostics 12:5615–5630. https://doi.org/10.7150/thno.56736
49. Seeger RC, Rayner SA, Banerjee A et al. (1977) Morphology, Growth, Chromosomal Pattern, and Fibrinolytic Activity of Two New Human Neuroblastoma Cell Lines. Cancer Research 37:1364–1371
50. Stock C, Bozsaky E, Watzinger F et al. (2008) Genes proximal and distal to MYCN are highly expressed in human neuroblastoma as visualized by comparative expressed sequence hybridization. Am J Pathol 172:203–214. https://doi.org/10.2353/ajpath.2008.061263
51. Chen Y, Takita J, Choi YL et al. (2008) Oncogenic mutations of ALK kinase in neuroblastoma. Nature 455:971–974. https://doi.org/10.1038/nature07399
52. Mosse YP, Greshock J, Margolin A et al. (2005) High-resolution detection and mapping of genomic DNA alterations in neuroblastoma. Genes Chromosomes Cancer 43:390–403. https://doi.org/10.1002/gcc.20198
53. George RE, Sanda T, Hanna M et al. (2008) Activating mutations in ALK provide a therapeutic target in neuroblastoma. Nature 455:975–978. https://doi.org/10.1038/nature07397
54. Kang J, Kamal A, Burrows FJ et al. (2006) Inhibition of Neuroblastoma Xenograft Growth by HSP90 Inhibitor. Anticancer Res. 26:1903–1908
55. Schäfer P, Muhs S, Turnbull L et al. (2023) Ex Vivo Model of Neuroblastoma Plasticity. Cancers (Basel) 15. https://doi.org/10.3390/cancers15041274
56. Guerreau D, Thedrez P, Fritsch P et al. (1990) In vitro therapeutic targeting of neuroblastomas using 125I-labelled meta-iodobenzylguanidine. Int J Cancer 45:1164–1168. https://doi.org/10.1002/ijc.2910450629
57. Manil L, Perdereau B, Barbaroux C et al. (1994) Strong uptake of 111In-pentetreotide by an MIBG-negative, xenografted neuroblastoma. Int J Cancer 57:245–246. https://doi.org/10.1002/ijc.2910570219
58. Biedler JL, Helson L, Spengler BA (1973) Morphology and Growth, Tumorigenicity, and Cytogenetics of Human Neuroblastoma Cells in Continuous Culture. Cancer Research 33:2643–2652
59. Bi X, Zhang J-Z (2003) Experimental study of thymidine kinase gene therapy of neuroblastoma in vitro and in vivo. Pediatr Surg Int 19:400–405. https://doi.org/10.1007/s00383-003-1019-0
60. Ghandi M, Huang FW, Jané-Valbuena J et al. (2019) Next-generation characterization of the Cancer Cell Line Encyclopedia. Nature 569:503–508. https://doi.org/10.1038/s41586-019-1186-3
61. Langlois S, St-Pierre M-E, Holland SH et al. (2023) Inhibition of PANX1 Channels Reduces the Malignant Properties of Human High-Risk Neuroblastoma. J Cancer 14:689–706. https://doi.org/10.7150/jca.79552

62. Pajtler KW, Mahlow E, Odersky A et al. (2014) Neuroblastoma in dialog with its stroma: NTRK1 is a regulator of cellular cross-talk with Schwann cells. Oncotarget 5
63. Pai P, Reddy Y, Das I et al. (2025) Targeting neuroblastoma with hydroxamic acid based HDAC1 and HDAC2 inhibitors: Insights from in vitro and in vivo studies. Invest New Drugs 43:780–791. https://doi.org/10.1007/s10637-025-01559-y
64. Heukamp LC, Thor T, Schramm A et al. (2012) Targeted expression of mutated ALK induces neuroblastoma in transgenic mice. Sci Transl Med 4:141ra91. https://doi.org/10.1126/scitranslmed.3003967
65. Ribatti D, Raffaghello L, Pastorino F et al. (2002) In vivo angiogenic activity of neuroblastoma correlates with MYCN oncogene overexpression. Int J Cancer 102:351–354. https://doi.org/10.1002/ijc.10742
66. Ross RA, Spengler BA, Biedler JL (1983) Coordinate morphologcial and biochemical interconversion of human neuroblastoma cells:741–747
67. Cuende J, Moreno S, Bolanos J.P. et al. (2008) Retinoic acid downregulates Rae1 leading to APC Cdh1 activation and neuroblastoma SH-SY5Y differentiation. Oncogene 27:3339–3344
68. Lopes FM, Schröder R, Da Frota MLC et al. (2010) Comparison between proliferative and neuron-like SH-SY5Y cells as an in vitro model for Parkinson disease studies. Brain Res 1337:85–94. https://doi.org/10.1016/j.brainres.2010.03.102
69. Kovalevich J, Langford D (2013) Considerations for the use of SH-SY5Y neuroblastoma cells in neurobiology. Methods Mol Biol 1078:9–21. https://doi.org/10.1007/978-1-62703-640-5_2
70. Prasad R (2025) Understanding Medical Devices. Springer Nature Switzerland, Cham
71. Vik TA, Pfluger T, Kadota R et al. (2009) (123)I-mIBG scintigraphy in patients with known or suspected neuroblastoma: Results from a prospective multicenter trial. Pediatr Blood Cancer 52:784–790. https://doi.org/10.1002/pbc.21932
72. Galldiks N, Kaufmann TJ, Vollmuth P et al. (2024) Challenges, limitations, and pitfalls of PET and advanced MRI in patients with brain tumors: A report of the PET/RANO group. Neuro Oncol 26:1181–1194. https://doi.org/10.1093/neuonc/noae049
73. Galldiks N, Langen K-J (2015) Applications of PET imaging of neurological tumors with radiolabeled amino acids. Q J Nucl Med Mol Imaging 59:70–82
74. Stegmayr C, Oliveira D, Niemietz N et al. (2017) Influence of Bevacizumab on Blood-Brain Barrier Permeability and O-(2-18F-Fluoroethyl)-l-Tyrosine Uptake in Rat Gliomas. J Nucl Med 58:700–705. https://doi.org/10.2967/jnumed.116.187047
75. Langen K-J, Stoffels G, Filss C et al. (2017) Imaging of amino acid transport in brain tumours: Positron emission tomography with O-(2-18Ffluoroethyl)-L-tyrosine (FET). Methods 130:124–134. https://doi.org/10.1016/j.ymeth.2017.05.019
76. Singnurkar A, Poon R, Detsky J (2023) 18F-FET-PET imaging in high-grade gliomas and brain metastases: a systematic review and meta-analysis. J Neurooncol 161:1–12. https://doi.org/10.1007/s11060-022-04201-6

77. Heiss P, Mayer S, Herz M et al. (1999) Investigation of Transport Mechanism and Uptake Kinetics of O-(2-[18F]Fluoroethyl)-L-Tyrosine In Vitro and In Vivo. J Nucl Med 40:1367–1373
78. Langen K-J, Hamacher K, Weckesser M et al. (2006) O-(2-18Ffluoroethyl)-L-tyrosine: uptake mechanisms and clinical applications. Nucl Med Biol 33:287–294. https://doi.org/10.1016/j.nucmedbio.2006.01.002
79. Nawashiro H, Otani N, Uozumi Y et al. (2005) High expression of L-type amino acid transporter 1 in infiltrating glioma cells. Brain Tumor Pathol 22:89–91. https://doi.org/10.1007/s10014-005-0188-z
80. Vettermann FJ, Diekmann C, Weidner L et al. (2021) L-type amino acid transporter (LAT) 1 expression in 18F-FET-negative gliomas. EJNMMI Res 11:124. https://doi.org/10.1186/s13550-021-00865-9
81. Krieger K, Pyka T, Mingels C et al. (2025) Kinetics of the amino acid uptake tracer O-(2-18Ffluoroethyl)-L-tyrosine (FET) in human brain. EJNMMI Res 15:90. https://doi.org/10.1186/s13550-025-01279-7
82. Dunet V, Pomoni A, Hottinger A et al. (2016) Performance of 18F-FET versus 18F-FDG-PET for the diagnosis and grading of brain tumors: systematic review and meta-analysis. Neuro Oncol 18:426–434. https://doi.org/10.1093/neuonc/nov148
83. Hutterer M, Nowosielski M, Putzer D et al. (2011) O-(2-18F-fluoroethyl)-L-tyrosine PET predicts failure of antiangiogenic treatment in patients with recurrent high-grade glioma. J Nucl Med 52:856–864. https://doi.org/10.2967/jnumed.110.086645
84. Galldiks N, Verger A, Zaragori T et al. (2019) Comment on "Hypometabolic gliomas on FET-PET-is there an inverted U-curve for survival?". Neuro Oncol 21:1612–1613. https://doi.org/10.1093/neuonc/noz173
85. Galldiks N, Unterrainer M, Judov N et al. (2019) Photopenic defects on O-(2-18F-fluoroethyl)-L-tyrosine PET: clinical relevance in glioma patients. Neuro Oncol 21:1331–1338. https://doi.org/10.1093/neuonc/noz083
86. Roach JR, Plaha P, McGowan DR et al. (2022) The role of 18Ffluorodopa positron emission tomography in grading of gliomas. J Neurooncol 160:577–589. https://doi.org/10.1007/s11060-022-04177-3
87. Walker MD, Dinelle K, Kornelsen R et al. (2013) In-vivo measurement of LDOPA uptake, dopamine reserve and turnover in the rat brain using 18FFDOPA PET. J Cereb Blood Flow Metab 33:59–66. https://doi.org/10.1038/jcbfm.2012.120
88. Schiepers C, Chen W, Cloughesy T et al. (2007) 18F-FDOPA kinetics in brain tumors. J Nucl Med 48:1651–1661. https://doi.org/10.2967/jnumed.106.039321
89. Zaragori T, Castello A, Guedj E et al. (2021) Photopenic Defects in Gliomas With Amino-Acid PET and Relative Prognostic Value: A Multicentric 11C-Methionine and 18F-FDOPA PET Experience. Clin Nucl Med 46:e36-e37. https://doi.org/10.1097/RLU.0000000000003240
90. Piccardo A, Lopci E, Conte M et al. (2012) Comparison of 18F-dopa PET/CT and 123I-MIBG scintigraphy in stage 3 and 4 neuroblastoma: a pilot study. Eur J Nucl Med Mol Imaging 39:57–71. https://doi.org/10.1007/s00259-011-1938-2

91. Lopci E, Piccardo A, Nanni C et al. (2012) 18F-DOPA PET/BT in Neuroblastoma: Comparison of Conventional Imaging with CT/MR. Clin Nucl Med 37:73–78
92. Piccardo A, Puntoni M, Lopci E et al. (2014) Prognostic value of ^{18}F-DOPA PET/CT at the time of recurrence in patients affected by neuroblastoma. Eur J Nucl Med Mol Imaging 41:1046–1056. https://doi.org/10.1007/s00259-014-2691-0
93. Rosenkrans ZT, Massey CF, Bernau K et al. (2022) 68 GaGa-FAPI-46 PET for non-invasive detection of pulmonary fibrosis disease activity. Eur J Nucl Med Mol Imaging 49:3705–3716. https://doi.org/10.1007/s00259-022-05814-9
94. Chandekar KR, Prashanth A, Vinjamuri S et al. (2023) FAPI PET/CT Imaging-An Updated Review. Diagnostics (Basel) 13. https://doi.org/10.3390/diagnostics13122018
95. Röhrich M, Loktev A, Wefers AK et al. (2019) IDH-wildtype glioblastomas and grade III/IV IDH-mutant gliomas show elevated tracer uptake in fibroblast activation protein-specific PET/CT. Eur J Nucl Med Mol Imaging 46:2569–2580. https://doi.org/10.1007/s00259-019-04444-y
96. Yao Y, Tan X, Yin W et al. (2022) Performance of 18 F-FAPI PET/CT in assessing glioblastoma before radiotherapy: a pilot study. BMC Med Imaging 22:226. https://doi.org/10.1186/s12880-022-00952-w
97. Jacob M, Chang L, Puré E (2012) Fibroblast activation protein in remodeling tissues. Curr Mol Med 12:1220–1243. https://doi.org/10.2174/156652412803833607
98. Day C-P, Merlino G, van Dyke T (2015) Preclinical mouse cancer models: a maze of opportunities and challenges. Cell 163:39–53. https://doi.org/10.1016/j.cell.2015.08.068
99. Pardridge WM (2005) The blood-brain barrier: Bottleneck in brain drug development. The Journal of the American Society for Experimental NeuroTherapeutics 2:3–14
100. Kenney J, Schmiedl U, Maravilla K et al. (1992) Measurement of blood-brain barrier permeability in a tumor model using magnetic resonance imaging with gadolinium-DTPA. Magn Reson Med 27:68–75. https://doi.org/10.1002/mrm.1910270108
101. Hed J, Dahlgren C, Rundquist I (1983) A simple fluorescence technique to stain the plasma membrane of human neutrophils. Histochemistry:105–110
102. Jaffer H, Adjei IM, Labhasetwar V (2013) Optical imaging to map blood-brain barrier leakage. Sci Rep 3:3117. https://doi.org/10.1038/srep03117
103. Stegmayr C, Bandelow U, Oliveira D et al. (2017) Influence of blood-brain barrier permeability on O-(2-18F-fluoroethyl)-L-tyrosine uptake in rat gliomas. Eur J Nucl Med Mol Imaging 44:408–416. https://doi.org/10.1007/s00259-016-3508-0
104. Russell WMS (1999) The principles of humane experimental technique, Special ed. Universities Federation for Animal Welfare
105. (2010) Directive 2010/63/EU of the European Parliament and of the Council of 22 September 2010 on the protection of animals used for scientific purposes
106. Kang M, Long T, Chang C et al. (2022) A Review of the Ethical Use of Animals in Functional Experimental Research in China Based on the "Four R" Principles of

Reduction, Replacement, Refinement, and Responsibility. Med Sci Monit 28:e938807. https://doi.org/10.12659/MSM.938807
107. Jankovic BD, Isakovic K, Lukic ML et al. (1975) Immunological Capacity of the Chicken Embryo. Immunology 29
108. Weber WT, Mausner R (1977) Avian Immunology: Migration Patterns of Avian Embryonic Bone Marrow Cells and their Differentiation to Functional T and B Cells. Plenum Press, New York
109. Garcia P, Wang Y, Viallet J et al. (2021) The Chicken Embryo Model: A Novel and Relevant Model for Immune-Based Studies. Front Immunol 12:791081. https://doi.org/10.3389/fimmu.2021.791081
110. Nowak-Sliwinska P, Segura T, Iruela-Arispe ML (2014) The chicken chorioallantoic membrane model in biology, medicine and bioengineering. Angiogenesis 17:779–804. https://doi.org/10.1007/s10456-014-9440-7
111. Hamburger V, Hamilton HL (1992) A series of normal stages in the development of the chick embryo. 1951. Dev Dyn 195:231–272. https://doi.org/10.1002/aja.1001950404
112. Bellairs R, Osmond M (2014) The atlas of chick development, Third edition. Elsevier/AP Academic Press is an imprint of Elsevier, Amsterdam
113. Chen L, Wang S, Feng Y et al. (2021) Utilisation of Chick Embryo Chorioallantoic Membrane as a Model Platform for Imaging-Navigated Biomedical Research. Cells 10. https://doi.org/10.3390/cells10020463
114. Miebach L, Berner J, Bekeschus S (2022) In ovo model in cancer research and tumor immunology. Front Immunol 13:1006064. https://doi.org/10.3389/fimmu.2022.1006064
115. Wang Y, Xue W, Pustovalova M et al. (2025) Chick Embryo Chorioallantoic Membrane (CAM) Model for Cancer Studies and Drug Evaluation. Front Biosci (Landmark Ed) 30:37456. https://doi.org/10.31083/FBL37456
116. Ribatti D, Vacca A, Roncali L et al. (1996) The chick embryo chorioallantoic membrane as a model for in vivo research on angiogenesis. Int. J. Dev. Biol. 40:1189–1197
117. Ribatti D, Nico B, Vacca A et al. (2001) Chorioallantoic membrane capillary bed: a useful target for studying angiogenesis and anti-angiogenesis in vivo. Anat Rec 264:317–324. https://doi.org/10.1002/ar.10021
118. Strojnik T, Kavalar R, Barone TA et al. (2010) Experimental Model and Immunohistochemical Comparison of U87 Human Glioblastoma Cell Xenografts on the Chicken Chorioallantoic Membrane and in Rat Brains. Anticancer Research 30:4851-1860
119. Harper K, Yatsyna A, Charbonneau M et al. (2021) The Chicken Chorioallantoic Membrane Tumor Assay as a Relevant In Vivo Model to Study the Impact of Hypoxia on Tumor Progression and Metastasis. Cancers (Basel) 13. https://doi.org/10.3390/cancers13051093
120. Shoin K, Yamashita J, Enkaku F et al. (1991) Chick Embryo Assay as Chemosensitivity Test for Malignant Glioma. Jpn. J. Cancer Res. 82:1165–1170

121. Vu BT, Shahin SA, Croissant J et al. (2018) Chick chorioallantoic membrane assay as an in vivo model to study the effect of nanoparticle-based anticancer drugs in ovarian cancer. Sci Rep 8:8524. https://doi.org/10.1038/s41598-018-25573-8
122. Rupp T, Legrand C, Hunault M et al. (2022) A Face-To-Face Comparison of Tumor Chicken Chorioallantoic Membrane (TCAM) In Ovo with Murine Models for Early Evaluation of Cancer Therapy and Early Drug Toxicity. Cancers (Basel) 14. https://doi.org/10.3390/cancers14143548
123. Charbonneau M, Harper K, Brochu-Gaudreau K et al. (2023) The development of a rapid patient-derived xenograft model to predict chemotherapeutic drug sensitivity/resistance in malignant glial tumors. Neuro Oncol 25:1605–1616. https://doi.org/10.1093/neuonc/noad047
124. Würbach L, Heidrich A, Opfermann T et al. (2012) Insights into bone metabolism of avian embryos in ovo via 3D and 4D 18F-fluoride positron emission tomography. Mol Imaging Biol 14:688–698. https://doi.org/10.1007/s11307-012-0550-6
125. Warnock G, Turtoi A, Blomme A et al. (2013) In vivo PET/CT in a human glioblastoma chicken chorioallantoic membrane model: a new tool for oncology and radiotracer development. J Nucl Med 54:1782–1788. https://doi.org/10.2967/jnumed.112.117150
126. Zuo Z, Syrovets T, Wu Y et al. (2017) The CAM cancer xenograft as a model for initial evaluation of MR labelled compounds. Sci Rep 7:46690. https://doi.org/10.1038/srep46690
127. Chen L, Wang Z, Fu X et al. (2023) Dynamic 3D morphology of chick embryos and allantois depicted nondestructively by 3.0T clinical magnetic resonance imaging. Poult Sci 102:102902. https://doi.org/10.1016/j.psj.2023.102902
128. Winter G, Koch ABF, Löffler J et al. (2020) Multi-Modal PET and MR Imaging in the Hen's Egg Test-Chorioallantoic Membrane (HET-CAM) Model for Initial in Vivo Testing of Target-Specific Radioligands. Cancers (Basel) 12. https://doi.org/10.3390/cancers12051248
129. Ribatti D, Alessandri G, Vacca A et al. (1998) Human neuroblastoma cells produce extracellular matrix-degrading enzymes, induce endothelial cell proliferation and are angiogenicin vivo. Int J Cancer 77:449–454. https://doi.org/10.1002/(SICI)1097-0215(19980729)77:3<449:AID-IJC22>3.0.CO;2-1
130. Ribatti D, Tamma R (2018) The chick embryo chorioallantoic membrane as an in vivo experimental model to study human neuroblastoma. J Cell Physiol 234:152–157. https://doi.org/10.1002/jcp.26773
131. Pastorino F, Loi M, Sapra P et al. (2010) Tumor regression and curability of preclinical neuroblastoma models by PEGylated SN38 (EZN-2208), a novel topoisomerase I inhibitor. Clin Cancer Res 16:4809–4821. https://doi.org/10.1158/1078-0432.CCR-10-1354
132. Mangieri D, Nico B, Coluccia AML et al. (2009) An alternative in vivo system for testing angiogenic potential of human neuroblastoma cells. Cancer Lett 277:199–204. https://doi.org/10.1016/j.canlet.2008.12.014

133. Patiño-Morales CC, Jaime-Cruz R, Ramírez-Fuentes TC et al. (2023) Technical Implications of the Chicken Embryo Chorioallantoic Membrane Assay to Elucidate Neuroblastoma Biology. Int J Mol Sci 24. https://doi.org/10.3390/ijms241914744
134. Boulland J-L, Halasi G, Kasumacic N et al. (2010) Xenotransplantation of human stem cells into the chicken embryo. J Vis Exp. https://doi.org/10.3791/2071
135. Cretu A, Fotos JS, Little BW et al. (2005) Human and rat glioma growth, invasion, and vascularization in a novel chick embryo brain tumor model. Clin Exp Metastasis 22:225–236. https://doi.org/10.1007/s10585-005-7889-x
136. Pastorino NG, Tomatsu S, Lin A et al. (2023) Using the Chick Embryo Brain as a Model for In Vivo and Ex Vivo Analyses of Human Glioblastoma Cell Behavior. J Vis Exp. https://doi.org/10.3791/65199
137. (2013) Ordinance on the Protection of Animals Used for Experimental Purposes (TierSchVersV)
138. Weiss L, Saller AM, Werner J et al. (2023) Nociception in Chicken Embryos, Part I: Analysis of Cardiovascular Responses to a Mechanical Noxious Stimulus. Animals (Basel) 13. https://doi.org/10.3390/ani13172710
139. Süß SC, Werner J, Saller AM et al. (2023) Nociception in Chicken Embryos, Part III: Analysis of Movements before and after Application of a Noxious Stimulus. Animals (Basel) 13. https://doi.org/10.3390/ani13182859
140. Kollmansperger S, Anders M, Werner J et al. (2023) Nociception in Chicken Embryos, Part II: Embryonal Development of Electroencephalic Neuronal Activity In Ovo as a Prerequisite for Nociception. Animals (Basel) 13. https://doi.org/10.3390/ani13182839
141. (1972) German Animal Welfare Act (TierSchG)
142. Cage TA, Louie JD, Liu SR et al. (2012) Distinct patterns of human medulloblastoma dissemination in the developing chick embryo nervous system. Clin Exp Metastasis 29:371–380. https://doi.org/10.1007/s10585-012-9456-6
143. Pace KR, Dutt R, Galileo DS (2019) Exosomal L1CAM Stimulates Glioblastoma Cell Motility, Proliferation, and Invasiveness. Int J Mol Sci 20. https://doi.org/10.3390/ijms20163982
144. Smith LM, Greenwood HE, Tyrrell WE et al. (2023) The chicken chorioallantoic membrane as a low-cost, high-throughput model for cancer imaging. Npj Imaging 1:1. https://doi.org/10.1038/s44303-023-00001-3
145. Benčurová K, Tran L, Friske J et al. (2024) An in vivo tumour organoid model based on the chick embryonic chorioallantoic membrane mimics key characteristics of the patient tissue: a proof-of-concept study. EJNMMI Res 14:86. https://doi.org/10.1186/s13550-024-01151-0
146. Choi C-H, Bruch M, Hong S-M et al. (2024) A Modified Quadrature Birdcage Coil Incorporated With a Curved Feature for In Ovo MR Imaging. IEEE Open J Eng Med Biol 5:534–541. https://doi.org/10.1109/OJEMB.2024.3420231
147. Choi C-H, Hong S-M, Felder J et al. (2024) Design, construction, and use of a tapered-spiral, quadrature 1H/23Na double-tuned coil for in ovo MRI at 7 T. Med Phys 51:8761–8767. https://doi.org/10.1002/mp.17448

148. Bao Q, Newport D, Chen M et al. (2009) Performance evaluation of the inveon dedicated PET preclinical tomograph based on the NEMA NU-4 standards. J Nucl Med 50:401–408. https://doi.org/10.2967/jnumed.108.056374
149. Krause S, Florea A, Choi C-H et al. (2025) Autoradiography of Intracerebral Tumours in the Chick Embryo Model: A Feasibility Study Using Different PET Tracers. Mol Imaging Biol 27:151–162. https://doi.org/10.1007/s11307-025-01983-9
150. Tona K, Voemesse K, N'nanlé O et al. (2022) Chicken Incubation Conditions: Role in Embryo Development, Physiology and Adaptation to the Post-Hatch Environment. Front Physiol 13:895854. https://doi.org/10.3389/fphys.2022.895854
151. Harris CE, Josselson LB, Bourassa DV et al. (2022) Examination of the impact of eggshell cuticle and membranes on Salmonella Enteritidis or Typhimurium recovery from inoculated and stored eggs. Journal of Applied Poultry Research 31:100297. https://doi.org/10.1016/j.japr.2022.100297
152. Wang H, Slavik MF (1998) Bacterial penetration into eggs washed with various chemicals and stored at different temperatures and times. J Food Prot 61:276–279. https://doi.org/10.4315/0362-028x-61.3.276
153. Kusstatscher P, Cernava T, Liebminger S et al. (2017) Replacing conventional decontamination of hatching eggs with a natural defense strategy based on antimicrobial, volatile pyrazines. Sci Rep 7:13253. https://doi.org/10.1038/s41598-017-13579-7
154. Orajaka LJE, Mohan K (1984) Aerobic Bacterial Flora From Dead-In-Shell Chicken Embryos From Nigeria. Avian Diseases 29
155. Cox NA, Berrang ME, Cason JA (2000) Salmonella penetration of egg shells and proliferation in broiler hatching eggs--a review. Poult Sci 79:1571–1574. https://doi.org/10.1093/ps/79.11.1571
156. Hananeh WM, Al-Natour MQ, Alaboudi AR et al. (2021) Congenital abnormalities in dead-in-shell chicks associated with mixed bacterial infections. Heliyon 7:e06272. https://doi.org/10.1016/j.heliyon.2021.e06272
157. Boulland J-L, Leung DSY, Thuen M et al. (2012) Evaluation of intracellular labeling with micron-sized particles of iron oxide (MPIOs) as a general tool for in vitro and in vivo tracking of human stem and progenitor cells. Cell Transplant 21:1743–1759. https://doi.org/10.3727/096368911X627598
158. Lee J, Borboa AK, Baird A et al. (2011) Non-invasive quantification of brain tumor-induced astrogliosis. BMC Neuroscience 12
159. Piroth MD, Prasath J, Willuweit A et al. (2013) Uptake of O-(2-18Ffluoroethyl)-L-tyrosine in reactive astrocytosis in the vicinity of cerebral gliomas. Nucl Med Biol 40:795–800. https://doi.org/10.1016/j.nucmedbio.2013.05.001
160. Sofroniew MV, Vinters HV (2010) Astrocytes: biology and pathology. Acta Neuropathol 119:7–35. https://doi.org/10.1007/s00401-009-0619-8
161. Chekhonin VP, Baklaushev VP, Yusubalieva GM et al. (2007) Modeling and immunohistochemical analysis of C6 glioma In Vivo. Cell Technologies in Biology and Medicine 2:501–509

162. Markwell SM, Ross JL, Olson CL et al. (2022) Necrotic reshaping of the glioma microenvironment drives disease progression. Acta Neuropathol 143:291–310. https://doi.org/10.1007/s00401-021-02401-4
163. Moffet JJD, Fatunla OE, Freytag L et al. (2023) Spatial architecture of high-grade glioma reveals tumor heterogeneity within distinct domains. Neurooncol Adv 5:vdad142. https://doi.org/10.1093/noajnl/vdad142
164. Wakai S, Hirokawa N (1978) Development of the blood-brain barrier to horseradish peroxidase in the chick embryo. Cell and Tissue Research 195:195–203
165. Janzer RC, Raff MC (1987) Astrocytes induce blood-brain barrier properties in endothelial cells. Letters to Nature 325:253–257
166. Möller W, Kummer W (2003) The blood-brain barrier of the chick glycogen body (corpus gelatinosum) and its functional implications. Cell and Tissue Research 313:71–80. https://doi.org/10.1007/s00441-003-0742-0
167. Parvas M, Parada C, Bueno D (2008) A blood-CSF barrier function controls embryonic CSF protein composition and homeostasis during early CNS development. Dev Biol 321:51–63. https://doi.org/10.1016/j.ydbio.2008.05.552
168. Parvas M, Bueno D (2010) The embryonic blood-CSF barrier has molecular elements to control E-CSF osmolarity during early CNS development. J Neurosci Res 88:1205–1212. https://doi.org/10.1002/jnr.22293
169. Stegmayr C, Willuweit A, Lohmann P et al. (2019) O-(2-18F-Fluoroethyl)-L-Tyrosine (FET) in Neurooncology: A Review of Experimental Results. Curr Radiopharm 12:201–210. https://doi.org/10.2174/1874471012666190111111046
170. Stegmayr C, Stoffels G, Kops ER et al. (2019) Influence of Dexamethasone on O-(2-18F-Fluoroethyl)-L-Tyrosine Uptake in the Human Brain and Quantification of Tumor Uptake. Mol Imaging Biol 21:168–174. https://doi.org/10.1007/s11307-018-1221-z
171. Tang G, Wang M, Tang X et al. (2003) Pharmacokinetics and radiation dosimetry estimation of O-(2-18Ffluoroethyl)-L-tyrosine as oncologic PET tracer. Appl Radiat Isot 58:219–225. https://doi.org/10.1016/s0969-8043(02)00311-1
172. Richard MA, Fouquet JP, Lebel R et al. (2017) Determination of an Optimal Pharmacokinetic Model of 18F-FET for Quantitative Applications in Rat Brain Tumors. J Nucl Med 58:1278–1284. https://doi.org/10.2967/jnumed.116.180612
173. Wang H-E, Wu S-Y, Chang C-W et al. (2005) Evaluation of F-18-labeled amino acid derivatives and 18FFDG as PET probes in a brain tumor-bearing animal model. Nucl Med Biol 32:367–375. https://doi.org/10.1016/j.nucmedbio.2005.01.005
174. Maurer GD, Brucker DP, Stoffels G et al. (2020) 18F-FET PET Imaging in Differentiating Glioma Progression from Treatment-Related Changes: A Single-Center Experience. J Nucl Med 61:505–511. https://doi.org/10.2967/jnumed.119.234757
175. Lohmann P, Herzog H, Rota Kops E et al. (2015) Dual-time-point O-(2-(18)Ffluoroethyl)-L-tyrosine PET for grading of cerebral gliomas. Eur Radiol 25:3017–3024. https://doi.org/10.1007/s00330-015-3691-6

176. Stegmayr C (2016) Effect of pharmaceutical interventions on reproducibility of O-(2-[18F]fluoroethyl)-L-tyrosine (FET) uptake kinetics in rat glioma models. Doctoral dissertation, RWTH Aachen University
177. Pauleit D, Floeth F, Herzog H et al. (2003) Whole-body distribution and dosimetry of O-(2-18Ffluoroethyl)-L-tyrosine. Eur J Nucl Med Mol Imaging 30:519–524. https://doi.org/10.1007/s00259-003-1118-0
178. Wester HJ, Herz M, Weber W et al. (1999) Synthesis and Radiopharmacology of O-(2-[18F]fluoroethyl)-L-Tyrosine for Tumor Imaging. The Journal of Nuclear Medicine 40:205–212
179. Clément A, Zaragori T, Filosa R et al. (2022) Multi-tracer and multiparametric PET imaging to detect the IDH mutation in glioma: a preclinical translational in vitro, in vivo, and ex vivo study. Cancer Imaging 22:16. https://doi.org/10.1186/s40644-022-00454-6
180. Cicone F, Filss CP, Minniti G et al. (2015) Volumetric assessment of recurrent or progressive gliomas: comparison between F-DOPA PET and perfusion-weighted MRI. Eur J Nucl Med Mol Imaging 42:905–915. https://doi.org/10.1007/s00259-015-3018-5
181. Li J, Stanger BZ (2020) How Tumor Cell Dedifferentiation Drives Immune Evasion and Resistance to Immunotherapy. Cancer Research 80:4037–4041. https://doi.org/10.1158/0008-5472.CAN-20-1420
182. Mintz B, Illmensee K (1975) Normal genetically mosaic mice produced from malignant teratocarcinoma cells. Proc Natl Acad Sci U S A 72:3585–3589. https://doi.org/10.1073/pnas.72.9.3585
183. Dolberg DS, Bissell MJ (1984) Inability of Rous sarcoma virus to cause sarcomas in the avian embryo. Letters to Nature 309:552–556
184. Ponzoni M, Bocca P, Chiesa V et al. (1995) Differential Effects of N-(4-Hydroxyphenyl)retinamide and Retinoic Acid on Neuroblastoma Cells: Apoptosis versus Differentiation. Cancer Research 55:853–861
185. Sarkar S, Peng C-C, Tung Y-C (2020) Comparison of VEGF-A secretion from tumor cells under cellular stresses in conventional monolayer culture and microfluidic three-dimensional spheroid models. PLOS ONE 15:e0240833. https://doi.org/10.1371/journal.pone.0240833
186. Chondrogiannis S, Marzola MC, Al-Nahhas A et al. (2013) Normal biodistribution pattern and physiologic variants of 18F-DOPA PET imaging. Nucl Med Commun 34:1141–1149. https://doi.org/10.1097/MNM.0000000000000008
187. Dias AH, Hansen AK, Munk OL et al. (2022) Normal values for 18F-FDG uptake in organs and tissues measured by dynamic whole body multiparametric FDG PET in 126 patients. EJNMMI Res 12:15. https://doi.org/10.1186/s13550-022-00884-0
188. Coffey RG, Cheldelin VH, Newburgh RW (1964) Glucose Utilization by Chick Embryo Heart Homogenates. The Journal of General Physiology 48:105–112
189. Kutchai H, King SL, Martin M et al. (1977) Glucose Uptake by Chicken Embryo Hearts at Various Stages of Development. Dev Biol 55:92–102
190. Liu Y-L, Lu M-Y, Chang H-H et al. (2016) Diagnostic FDG and FDOPA positron emission tomography scans distinguish the genomic type and treatment outcome

of neuroblastoma. Oncotarget 7:18774–18786. https://doi.org/10.18632/oncotarget.7933
191. Kaufman J (2022) Innate immune genes of the chicken MHC and related regions. Immunogenetics 74:167–177. https://doi.org/10.1007/s00251-021-01229-2
192. Everaert N, Smit L de, Debonne M et al. (2008) Changes in acid-base balance and related physiological responses as a result of external hypercapnia during the second half of incubation in the chicken embryo. Poult Sci 87:362–367. https://doi.org/10.3382/ps.2007-00345